

cy 2



# AN ANALYSIS OF TRANSONIC VISCOUS/INVISCID INTERACTIONS ON AXISYMMETRIC BODIES WITH SOLID STINGS OR REAL PLUMES

Steven F. Yaros  
ARO, Inc, a Sverdrup Corporation Company

PROPELLION WIND TUNNEL FACILITY  
ARNOLD ENGINEERING DEVELOPMENT CENTER  
AIR FORCE SYSTEMS COMMAND  
ARNOLD AIR FORCE STATION, TENNESSEE 37389

February 1978

Final Report for Period October 1, 1976 — September 30, 1977

Approved for public release; distribution unlimited.

Property of U. S. Air Force  
AEDC LIBRARY  
F43600-77-C-0003

Prepared for

ARNOLD ENGINEERING DEVELOPMENT CENTER/DOTR  
ARNOLD AIR FORCE STATION, TENNESSEE 37389

## NOTICES

When U. S. Government drawings, specifications, or other data are used for any purpose other than a definitely related Government procurement operation, the Government thereby incurs no responsibility nor any obligation whatsoever, and the fact that the Government may have formulated, furnished, or in any way supplied the said drawings, specifications, or other data, is not to be regarded by implication or otherwise, or in any manner licensing the holder or any other person or corporation, or conveying any rights or permission to manufacture, use, or sell any patented invention that may in any way be related thereto.

Qualified users may obtain copies of this report from the Defense Documentation Center.

References to named commercial products in this report are not to be considered in any sense as an indorsement of the product by the United States Air Force or the Government.

This report has been reviewed by the Information Office (OI) and is releasable to the National Technical Information Service (NTIS). At NTIS, it will be available to the general public, including foreign nations.

## APPROVAL STATEMENT

This report has been reviewed and approved.

*Elton R. Thompson*  
ELTON R. THOMPSON  
Project Manager, Research Division  
Directorate of Test Engineering

Approved for publication:

FOR THE COMMANDER

*Marion L. Laster*

MARION L. LASTER  
Director of Test Engineering  
Deputy for Operations

**UNCLASSIFIED**

REPORT DOCUMENTATION PAGE		READ INSTRUCTIONS BEFORE COMPLETING FORM
1 REPORT NUMBER AEDC-TR-77-106	12 GOVT ACCESSION NO. 	3 RECIPIENT'S CATALOG NUMBER
4 TITLE (and Subtitle) AN ANALYSIS OF TRANSONIC VISCOUS/INVISCID INTERACTIONS ON AXISYMMETRIC BODIES WITH SOLID STINGS OR REAL PLUMES		5 TYPE OF REPORT & PERIOD COVERED Final Report - October 1, 1976 - September 30, 1977
7 AUTHOR(s) Steven F. Yaros, ARO, Inc.	6 PERFORMING ORG REPORT NUMBER	
9 PERFORMING ORGANIZATION NAME AND ADDRESS Arnold Engineering Development Center/DOT Air Force Systems Command Arnold Air Force Station, Tennessee 37389	10 PROGRAM ELEMENT, PROJECT, TASK AREA & WORK UNIT NUMBERS Program Element 65807F	
11 CONTROLLING OFFICE NAME AND ADDRESS Arnold Engineering Development Center/DOS Arnold Air Force Station, Tennessee 37389	12 REPORT DATE February 1978	
14 MONITORING AGENCY NAME & ADDRESS (if different from Controlling Office)	13 NUMBER OF PAGES 164	
	15 SECURITY CLASS (of this report) UNCLASSIFIED	
	15a DECLASSIFICATION DOWNGRADING SCHEDULE N/A	
16 DISTRIBUTION STATEMENT (of this Report)  Approved for public release; distribution unlimited.		
17 DISTRIBUTION STATEMENT (of the abstract entered in Block 20, if different from Report)		
18 SUPPLEMENTARY NOTES  Available in DDC		
19 KEY WORDS (Continue on reverse side if necessary and identify by block number) transonic flow      boundary layer viscous flow      axisymmetric inviscid flow      bodies interactions      plumes		
20 ABSTRACT (Continue on reverse side if necessary and identify by block number)  A numerical and theoretical investigation of pressure distribution predictions over arbitrary bodies of revolution in transonic flow has been carried out. Special features of the study include a comprehensive survey of previous and contemporary efforts in this direction and a detailed description of a combined viscous/inviscid digital computer program which was developed to iterate between the inviscid transonic and the		

# UNCLASSIFIED

## 20. ABSTRACT (Continued)

viscous portions of the analysis. For attached boundary layers the calculation procedure has been fully automated for both subcritical and supercritical cases, and predicted pressure distributions agree well with data. The entrainment effect of a real plume was modeled using the mixing theory first developed by Chapman and Korst. This method shows promise when its results are compared with data, but further work must be done to more correctly model the turbulent mixing of the two jets.

## PREFACE

The work reported herein was conducted by the Arnold Engineering Development Center (AEDC), Air Force Systems Command (AFSC), under Program Element 65807F. The results of the investigation were obtained by ARO, Inc., AEDC Division (a Sverdrup Corporation Company), operating contractor for the AEDC, AFSC, Arnold Air Force Station, Tennessee, under ARO Project Number P33A-G4A. The manuscript was submitted for publication on October 18, 1977.

The author would like to thank all of the people who, at some time or another, gave him assistance during his work toward the completion of this dissertation. Space allows mention of only a handful, unfortunately. In particular, sincere gratitude is extended to my advisor, Dr. Jain-Ming Wu, who has always provided me with solid technical advice and continual encouragement. Two of my co-workers, Dr. David L. Whitfield and Mr. Robert C. Bauer of the Propulsion Wind Tunnel Facility, ARO, Inc., are especially to be thanked for their aid, particularly during the past two years. Formulation of the Combined Program would have been impossible without the aid of Mr. Karl Kneile, and the same may be said about the Plume Entrainment Program and Mr. John Fox's efforts.

Both of these gentlemen are employed by ARO, Inc. in the Central Data Processing Division. Finally, I would like to thank warmly the woman who typed this manuscript, Mrs. Lena Blocker, and the women who prepared the plots and sketches, Mrs. Frances May, Mrs. Lorene Mottern, and Mrs. Peggy Teague. They never ceased to amaze me with their speed and accuracy. The material reported herein was submitted to the University of Tennessee as partial fulfillment of the requirements of the degree of Doctor of Philosophy.

## CONTENTS

<u>Chapter</u>	<u>Page</u>
I. INTRODUCTION . . . . .	1
II. THE VISCOUS/INVISCID ITERATIVE TECHNIQUE AND THE COMBINED PROGRAM . . . . .	11
Introductory Remarks . . . . .	11
Viscous/Inviscid Iterative Approach . . . . .	11
Inviscid Digital Computer Program . . . . .	15
Viscous Digital Computer Program . . . . .	26
Plume Calculation . . . . .	31
Combined Viscous/Inviscid Iterative Program . . . . .	35
III. MIXING ANALYSIS AND THE PLUME ENTRAINMENT MODEL . . . . .	53
Introductory Remarks . . . . .	53
Mixing Analysis . . . . .	54
Digital Computer Program . . . . .	66
Stagnation Temperature Distribution Near the Nozzle/Afterbody . . . . .	67
The Mixing Parameter, $\sigma$ . . . . .	77
IV. ANALYTICAL RESULTS IN COMPARISON TO EXPERIMENT . . . . .	82
Introductory Remarks . . . . .	82
Solid Sting Cases . . . . .	83
Real Plume Cases . . . . .	111
V. CONCLUSIONS AND RECOMMENDATIONS . . . . .	125
BIBLIOGRAPHY . . . . .	131

## ILLUSTRATIONS

<u>Figure</u>	<u>Page</u>
1. Schematic of the Various Flow Regions Involved in the Modeling of the Afterbody Problem . . . . .	3
2. Schematic of the Modified Flow Regions Involved in the Modeling of the Afterbody Problem . . . . .	14
3. Two Coordinate Systems Used by RAXBOD . . . . .	18
4. Comparison of the Viscous Methods . . . . .	27
5. Plume Shape as a Function of Nozzle Pressure Ratio . . . . .	34
6. General Iteration Flow Plan . . . . .	36
7. Boundary Layer Coordinate System Used in the Viscous Portion of the CVI Program . . . . .	42
8. Schematic Diagram of Boundary Layer Displacement Thickness Relaxation Technique . . . . .	45
9. Effect of Relaxation Factor on Convergence, NASA Langley $\ell/d_m = 1.768$ Afterbody, $M_\infty = 0.8$ , $Re/\ell = 3.8 \times 10^6 \text{ ft}^{-1}$ . . . . .	47
10. Characteristic Pressure, Effective Body Shapes, and Displacement Thickness Distribution of a Converging Viscous/Inviscid Iteration . . . . .	48
11. Boundary Layer Relaxation Displacement Thickness Development Relative to Calculated Displacement Thickness . . . . .	50

<u>Figure</u>	<u>Page</u>
12. Comparison of the Oscillating Solution of an R = 1.0 Case and the Converged Solution of an R = 0.3 Case . . . . .	51
13. Schematic Diagram of the Jet Mixing Region . . . . .	56
14. Component Velocity Function for a Flow Not Yet Fully Developed . . . . .	62
15. Qualitative Examples of the Stagnation Temperature and Velocity Distribution for Boundary Layer and Fully-Developed Flow . . . . .	70
16. Stagnation Temperature Distribution for $T_{ob} =$ $T_{oa}$ . . . . .	75
17. Variation of Mixing Parameter, $\sigma$ , with Downstream Distance . . . . .	81
18. Equivalent Body Shape and Circumferential Pres- sure Tap Locations . . . . .	84
19. Longitudinal Pressure Coefficient Distribution for the Equivalent Body . . . . .	86
20. Sketch of the NASA Langley $l/d_m = 1.768$ Circular Arc Boattail Model Showing Internal Sting Arrangement for Support of Simulators . . . . .	91
21. Shape of the NASA Langley $l/d_m = 1.768$ Circular Arc Boattail and Cylindrical Plume Simulator . . . . .	92
22. Longitudinal Pressure Coefficient Distribution for the NASA Langley $l/d_m = 1.768$ Circular Arc Boattail in the Langley 16-ft Transonic Wind Tunnel . . . . .	94

<u>Figure</u>	<u>Page</u>
23. Longitudinal Pressure Coefficient Distribution for the NASA Langley $l/d_m = 1.768$ Circular Arc Boattail Using a Two-Dimensional Boundary Layer in the CVI Program . . . . .	103
24. Longitudinal Pressure Coefficient Distribution for the NASA Langley $l/d_m = 1.768$ Circular Arc Boattail in the Langley 1/3-Meter Cryogenic Tunnel . . . . .	105
25. Sketch of Air-Powered Cone-Cylinder Model with a Typical Circular-Arc Convergent Nozzle Installed . . . . .	112
26. Boundary Layer Displacement Calculation for the Plenum and Nozzle of the NASA Langley $l/d_m = 1.768$ Air-Powered Model . . . . .	114
27. Longitudinal Pressure Coefficient Distribution for the NASA Langley $l/d_m = 1.768$ Circular Arc Boattail with a Real Plume . . . . .	116
28. Boundary Layer Correction due to Entrainment for the NASA Langley $l/d_m = 1.768$ Circular Arc Boattail for $M_\infty = 0.8$ , $NPR = 4$ , $\sigma = \sigma_I$ . . .	119
29. Comparison of Boattail and Plume Simulator Shapes Between the NASA Langley $l/d_m = 1.768$ Circular Arc Boattail and the AGARD 15-deg Boattail . . . . .	121

<u>Figure</u>	<u>Page</u>
30. Longitudinal Pressure Coefficient Distribution for the AGARD 15-deg Boattail . . . . .	122
C-1. Comparison of Boattail and Plume Simulator Shapes Between the NASA Langley 1.768 Circular Arc Boattail and the CBA Boattail . . . . .	151
C-2. Longitudinal Pressure Coefficient Distribution for the CBA Boattail, $M_{\infty} = 0.56$ . . . . .	152
C-3. Longitudinal Pressure Coefficient Distribution for the CBA Boattail, $M_{\infty} = 0.70$ . . . . .	153
C-4. Maximum Pressure Coefficient Change at Each Iteration Showing Presence of Two Solutions, $M_{\infty} = 0.80$ . . . . .	155
C-5. Longitudinal Pressure Coefficient Distribution for the CBA Boattail Showing Presence of Two Solutions, $M_{\infty} = 0.80$ . . . . .	156
C-6. Longitudinal Pressure Coefficient Distribution for the CBA Boattail Showing Erroneous Solution, $M_{\infty} = 0.90$ . . . . .	157
C-7. Longitudinal Pressure Coefficient Distribution for the CBA Boattail Using Central Differences Only, $M_{\infty} = 0.80$ . . . . .	159

## TABLES

	<u>Page</u>
I. Summary of Previous Viscous/Inviscid Iterative Efforts . . . . .	9
II. Convergence History with and without Mesh Halving . . . . .	24
III. Typical Computation Times Using Mesh Halving . . . . .	25
IV. Input to the South-Jameson Transonic Program (RAXBOD) . . . . .	38
V. Input for the Viscous Portion of the CVI Program . . . . .	40
VI. Input for the Plume Displacement Thickness Subprogram (DELPL), as Provided by the Calling Subroutine . . . . .	68

## APPENDIXES

A. DEVELOPMENT OF AN APPROXIMATE CLOSED FORM SOLUTION FOR THE TRANSIENT INITIAL BOUNDARY LAYER INTEGRALS . . . . .	139
B. LISTING OF THE PLUME ENTRAINMENT PROGRAM, DELPL . . . . .	143
C. ANALYSIS OF THE CBA BOATTAIL - AN ANOMALOUS CASE . . . . .	150
NOMENCLATURE . . . . .	160

## CHAPTER I

## INTRODUCTION

The transonic flow about an axisymmetric jet engine nacelle can create pressure forces which may contribute significantly to the total drag of the aircraft. In wind tunnel testing of such configurations, it is desirable to have analytical methods to predict the pressure distribution over the nacelle. With reliable prediction methods, areas of specific interest in the Mach number/Reynolds number test envelope may be investigated. Such methods are also of value for the placement and sizing of wind tunnel instrumentation and an evaluation of wall interference effects.

Particular interest has centered around the aft portions of the nacelle under the general topic of nozzle-afterbody (NAB) flow problems. The combination of internal and external flows, with their viscous properties, and the possibility of a shock wave on the afterbody creates a flow that is complex and highly interactive. The jet plume itself, considered in its relationship with the external flow, has the dual characteristics of a solid body, causing turning of the external flow, and of a shear layer, which accelerates the external flow due to the higher jet velocity, in general. Any prediction must include, in some way, all of the above-mentioned characteristics if it is to be accurate.

In order to render this complex flow manageable to analysis, an approximate model, as shown in Figure 1, is assumed. Most methods that have addressed themselves to the solution of the NAB problem use a similar type of flow model (1)<sup>1</sup>, differing primarily in the way that the mixing region is handled. Using this model, the usual approach is to use a viscous/inviscid iterative technique, in which the body shape is modified by the boundary-layer displacement thickness calculated along the length of the body. An inviscid calculation of the external flow is then carried out on the new body shape, and the viscous/inviscid iteration is continued until convergence. The plume shape may be modified in some way due to the effects of flow entrainment and changes in the pressures of the local inviscid flow. If the nacelle is mounted on a solid sting, then no entrainment analysis is required and the viscous/inviscid method is directly applicable to the nacelle/sting combination.

Numerous recent efforts have used a viscous-inviscid iterative method to predict pressure distributions with various degrees of success. Grossman and Melnik (2) were among the first to publish results of a combined viscous-inviscid iterative computer program, but they treated the jet plume as a solid body. Further efforts at Grumman (3) took the entrainment effect of the plume into account through the

---

<sup>1</sup>Numbers in parentheses refer to similarly numbered references in the Bibliography.

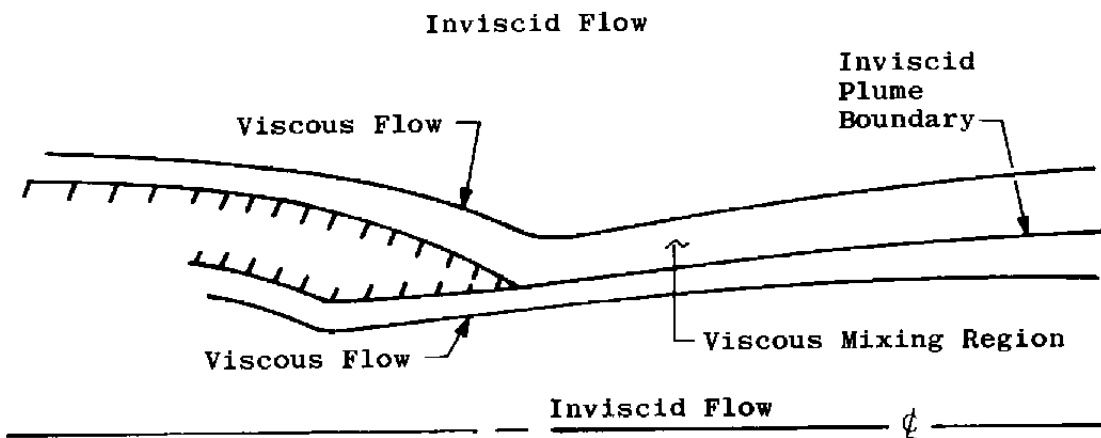


Figure 1. Schematic of the various flow regions involved in the modeling of the afterbody problem.

use of a correction to the plume shape based on Green's integral method (4). This method is still the basis of the plume entrainment model, according to the most recent publication (5), but current efforts have shifted to the case of afterbodies with flow separation occurring on the afterbody, with reattachment located on the solid supporting sting or plume. Presz's method (6) for predicting and calculating the separated region is used. It is significant to note that even in cases where the flow is substantially attached, Grossman and Melnik felt that the Green's integral method "... [did] not take into account the complete mixing of the high velocity jet with the external stream. Nonetheless, this procedure [did], at least qualitatively, produce a necking-down of the wake displacement surface and [indicated] some jet-entrainment effects." (3)

Keith, et al. (7) addressed the more complicated problem of the transonic flow about a two-dimensional or axisymmetric high-bypass-ratio fan duct nacelle with appropriate inlet and exhaust flows. Their solution technique was a Streamtube Curvature Analysis, in which the streamline coordinates were updated based on new coordinates required by the continuity equation and the effect of the resulting change in streamline curvature as computed from the integrated momentum equation. This inviscid solution technique was combined with a boundary-layer analysis, which, however, was used only over the solid body to provide a new effective body for the inviscid analysis. This work also included calculations

for incipient separation, but no detailed analysis of the flow field from separation to recompression was carried out. In addition, any changes in jet plume shape itself were neglected.

A "wake-body" configuration for flow over an after-body with a blunt base and no plume was used by Rom and Bober (8) in their iterative solution technique. At the end of the boattail a conical body was assumed over which the flow was calculated in the regular viscous/inviscid iterative manner until the boundary layer solution began to diverge. The minimum radius was then extended as a solid-body cylinder downstream. For uniqueness of solution, however, an experimental pressure at the separation point was required, as the shape of the "wake-body" was varied until this pressure was matched. The "wake-body" concept will be used in this paper for one configuration similar to those configurations studied by Rom and Bober. In a broader sense, however, it can be said that the wake-body approach is basic to the modeling of plume or wake flow, whether the flow is separated or attached, when the viscous/inviscid iterative method of solution is utilized.

It is striking to see the advances made in recent years, both from the recognition of the similarity of approach, vis-a-vis the iterative technique, to the application of the particular differences in the detailed problems considered by each effort. Chow, Bober, and Anderson (9) pointed out the inadequacy of small disturbance theory for use in the

inviscid portion of the iteration. Their predictions of attached flows over a boattail with a cylindrical sting were improved when the full transonic potential equations were used. They were also among the first to acknowledge the necessity of "relaxing" the boundary layer correction as a means of attaining convergence of the iterative technique. Bower (10) applied the iterative technique to the problem of axisymmetric or two-dimensional diffusers. His method is interesting in that he applied Strong Interaction Theory once his solution indicated separation, that is to say, when his viscous solution began to diverge, he would begin calculating the flow step-by-step downstream using a one-dimensional description of the inviscid region solved simultaneously with the integral equations for the turbulent compressible viscous layer. Calarese (11) approached the jet plume displacement phenomenon by means of varying the location of a cone frustum on the NAB support sting according to a correlation given by McDonald and Hughes (12). Any separated regions were calculated using a Korst base flow analysis. Calarese's method, however, was limited to subsonic free-stream flows.

In the work of Moulden, Wu, and Spring (13) and the more comprehensive work of Wu, Moulden, and Uchiyama (14), excellent descriptions of the interaction of the flow components about a missile-type configuration are given. The approach to the solution of the entire flow field about a missile with and without fins is the viscous/inviscid iteration, but the inviscid portion of the analysis is somewhat

limited in that the transonic small perturbation equation has been used throughout. The attached boundary layer flow is handled in a straightforward manner employing the method of Nash (15), while the inviscid plume shape is calculated with a step-by-step method of characteristics solution taking into account the static pressure variation due to the interaction. Concerning itself with missile configurations, however, the complete method assumes a strong interaction between the jet plume and the external flow, and the analysis assumes a sizeable separated area from the afterbody to a point of reattachment, or "confluence," on the plume. This region is treated with a Korst component analysis.

Chronologically, the past year has witnessed the culmination of what may be regarded as the first stage of the viscous/inviscid iterative solution of transonic nozzle afterbody flows, including the effects of shock boundary layer interaction, plume and external flow interaction, and afterbody flow separation and reattachment. This was demonstrated at the Propulsion Interactions Workshop held at Langley Research Center in May 1976 (16), where no less than five papers were presented dealing with the viscous/inviscid iterative method, and a number of other papers were delivered treating the analyses of individual components of the flows. The most recent papers also indicate a continued and widespread interest and confidence in iterative techniques. Reubush and Putnam (17) and the continuing efforts related to this work, Putnam and Abeyounis (18) and Wilmoth (19), have

applied the iterative method to flows with separation, according to the Presz method, but have not included any plume entrainment model in their analysis. Cosner and Bower (20) have also concentrated on the separated case, using an "empirical bridging" technique to carry the flow analysis past the point of reattachment to a point where boundary layer calculations may once again be used. Plume entrainment is modeled by treating the inviscid plume boundary as a non-adiabatic moving wall. The present author's most recent utilization of the viscous/inviscid iteration (21) included a crude model for plume entrainment based on mass conservation considerations. Finally, a most interesting approach, and one that may be representative of future efforts, was provided by Holst (22), who used the iteration technique combined with solution of the Navier-Stokes equations in the afterbody/plume region. A summary of the above information is presented in Table I.

The purpose of this thesis will be to provide a viscous/inviscid iterative technique valid for the solution of transonic, attached flows over typical jet engine nacelles, including a reliable and efficient method of accounting for the effect of jet plume entrainment on the afterbody pressure distribution. Accordingly, Chapter II will describe the development of the combined viscous and inviscid digital computer program and Chapter III will derive the equations, based on a Chapman-Korst mixing analysis, necessary for the implementation of the plume entrainment model. Results of the

TABLE I  
SUMMARY OF PREVIOUS VISCOUS/INVISCID ITERATIVE EFFORTS

Name and Reference	Plume Entrainment	Separated Flows	Comments
Grossman & Melnik (2)	No	No	Treated plumes as solid body
Grossman & Melnik (3)	Yes	No	Green's Integral Method for mixing
Yaeger (5)	Yes	Yes	Presz's Method for separated flows
Keith, et al. (7)	No	No	Streamtube curvature analyses of bypass jet engine
Rom and Bober (8)	No	Yes	Wake body for separated region
Chow, Bober, and Anderson (9)	No	No	"Relaxed" boundary layer
Bower (10)	No	Yes	Strong interaction theory for separated regions
Cosner & Bower (20)	No	Yes	
Calarese (11)	No	Yes	One-stream Chapman-Korst analysis for separated region
Wu, Moulden, and Uchiyama (14)	Yes	Yes	Separated flow assumed
Reubush & Putnam (17)	Yes	No	Presz's Method for separated flows
Putnam & Abeyounis (18)	Yes	No	
Yaros (21)	Yes	No	Plume entrainment effect based on mass conservation
Holst (22)	No	Yes	Navier-Stokes equation used in after-body and plume region

combined program, compared with data from typical practical geometric configurations, will be presented in Chapter IV, with Chapter V presenting conclusions and recommendations based on these efforts.

## CHAPTER II

THE VISCOUS/INVISCID ITERATIVE TECHNIQUE  
AND THE COMBINED PROGRAMIntroductory Remarks

This section will describe the physical model of the transonic viscous flow over a typical nozzle/afterbody combination, emphasizing the case where the flow is largely attached. Further simplifications of the model to enhance the mathematical resolution of the complex flow field will then be presented, followed by an explanation of the viscous/inviscid iterative technique as applied in this thesis. A summary of the component inviscid, viscous, and plume digital computer programs will indicate the advantages and limitations of this method, and the iterative technique as carried out operationally with the combined program will be described.

Viscous/Inviscid Iterative Approach

As indicated previously, the physical model applied to transonic flows over an afterbody and plume combination usually takes the form shown in Figure 1, page 3. The flow over the afterbody and, for that matter, the flow over the body preceding the afterbody are broken down into their inviscid and viscous components, a result of the application of classical boundary layer principles. This simplification of the flow over the body is justifiable if no local flow

separations, due to strong shock-boundary layer interactions and/or excessive changes in body shape, are present. The flow within the nozzle is approximated in an identical manner, with similar restrictions on local flow separation. The resulting flow at the end of the nozzle/afterbody is still within the realm of the boundary layer concept, that is, there exists two boundary layers external to which are their respective, essentially inviscid, external and internal flows.

With no viscous effects, for example if the internal and external flows were fully inviscid and uniform at the end of the nozzle/afterbody, the subsequent flow development would follow the line of the inviscid jet plume, denoted in Figure 1, page 3, as the inviscid jet plume boundary. This boundary is a function of the ratio of the pressure of the jet and the pressure of the external stream as well as the thermodynamic properties of both streams. Under this inviscid assumption, the jet plume boundary would act as a solid obstruction to the external flow, causing it to turn more rapidly in the neighborhood of the nozzle/afterbody endpoint, thus increasing the pressure of the afterbody. This phenomenon is characterized as the "displacement effect" of the plume shape.

In the actual, physical case there exists a strong viscous interaction between the internal and external streams after the nozzle/afterbody endpoint. There is substantial turbulent mixing between the two streams with mass and momentum transfer across the inviscid jet boundary. This

phenomenon, known as the "entrainment effect" of the jet plume, will change the effective shape of the plume as seen by the external inviscid flow.

It is for these reasons that the flow model shown in Figure 2 is assumed for purposes of applying the viscous/inviscid iterative technique. The technique is restricted to afterbodies with sharp trailing edges, i.e. no substantial base areas are permitted. Basically, this model reflects the assumption that the plume boundary will be treated as a solid boundary in the first iterative computation. As a qualitative example, consider the afterbody and original plume boundary as shown in Figure 2. Application of the pressure distribution over this body/plume combination to the viscous boundary layer solution would result in a classic viscous/inviscid solution as shown by the solid lines denoting the displacement thickness of the external flow. If the viscous mixing between the plume and external flow were included, however, the original plume shape would be modified as shown by the dashed line, as would be the resulting effective body as determined by the boundary layer displacement thickness and modified plume shape.

One is then led naturally to the concept of the viscous/inviscid iterative technique. With the new effective body and effective plume shape the inviscid calculation is repeated. If the pressure distribution over the body and plume agrees with the previous pressure distribution, the

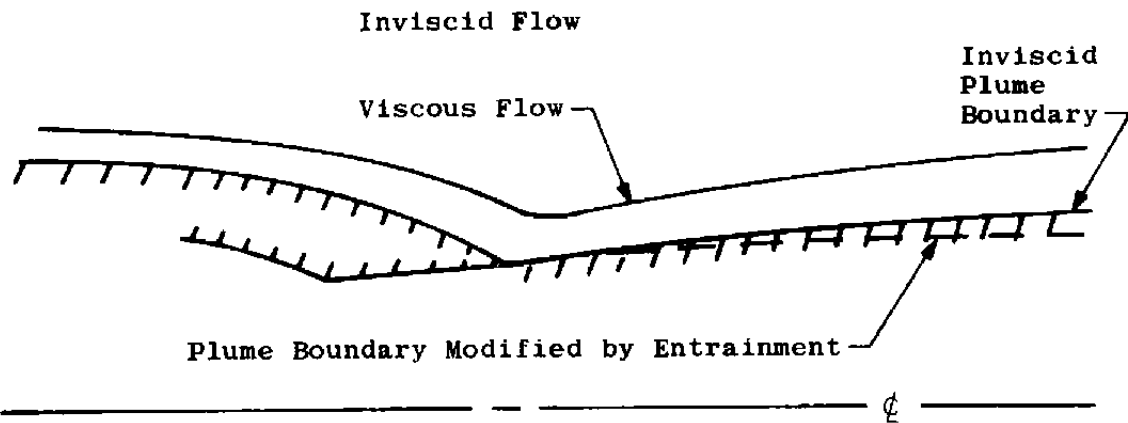


Figure 2. Schematic of the modified flow regions involved in the modeling of the afterbody problem.

solution is considered converged. If not, the viscous/inviscid iteration is continued.

One advantage to this approach is that the viscous/inviscid iterative operation may be developed for flows over what are effectively solid bodies, and the adjustment to the effective plume shape, which will be developed in Section III, may be included when necessary. Thus, flows over afterbodies with solid support stings may be treated directly by this method by simply not applying the plume entrainment adjustments.

#### Inviscid Digital Computer Program

The use of a reliable and accurate inviscid digital computer program in the viscous/inviscid iterative method is of prime importance, in that it is only through this segment of the iteration that any upstream influences of perturbations of the flow can be accounted for, as the viscous segment is essentially parabolic in the longitudinal direction. Certain requirements peculiar to the nature of the transonic afterbody flow problem demand an inviscid digital computer program with the following characteristics:

1. The program must be fully transonic.
2. The program must be axisymmetric.
3. Small perturbation approximations are valid for restricted body shapes and may not be satisfactory for the afterbody geometries considered.

4. Arbitrary effective body shapes must be acceptable to the program.

5. Computation time must not be excessive.

In early applications of the iterative method (23), three digital computer programs were used and compared, two of which proved to be unsatisfactory. Of these two, the first, the Douglas-Neumann Potential Flow Program, displayed favorable accuracy and reliability, but it was limited to wholly subsonic flow. The second program was the Pratt and Whitney Transonic Program, which was based on the small perturbation form of the transonic flow equations. In addition to this restriction, it displayed other shortcomings related to extreme sensitivity to the effective body shape derivatives and a chronic inability to provide reliable solutions for supersonic portions of the flow. By far the most acceptable inviscid computer program examined was the third, the South-Jameson Relaxation Solution for Inviscid Axisymmetric Flow, RAXBOD (24). RAXBOD is a finite-difference relaxation solution of the full transonic potential equation with exact boundary conditions. The program is applicable only to axisymmetric bodies in steady flow. These characteristics of RAXBOD satisfy the first three requirements stated previously.

In addition, RAXBOD contains some other special features which enhance its use for flow calculations about afterbody and sting or plume combinations, as well as for flow about the entire axisymmetric body. Originally conceived

as a calculation method for blunt axisymmetric bodies, RAXBOD uses two different coordinate systems along the length of the body, as shown in Figure 3. Based on the experience of Lipnitskii and Lifshits (25), South and Jameson chose to use a conformal body normal coordinate system in the body nose region. This coordinate system supplies the fine and well balanced grid distribution necessary in this region of highly changeable flow. Surprisingly, this coordinate system also works well for pointed-nose bodies by assuming the body angle to be 90 degrees at the nose and supplying the other normal coordinate axes at their true body-normal angles. According to South and Jameson, "This procedure leaves an embarrassing gap in the coordinates in the region ahead of the nose, but the calculation proceeded without difficulty." (24) The present author has also experienced little difficulty with calculations in the region of a pointed nose, typical of an equivalent body of revolution rather than a nacelle, providing that the shape is convex, in spite of the fact that the difference in orientation of the first two normal axes is often 75 degrees or more.

At some distance down the body, usually, but not always, the point where the body obtains a horizontal slope, the sheared cylindrical system of coordinates is introduced. In this system, the coordinate axes extending out into the flow remain perpendicular to the axis of symmetry of the body, while the tangential coordinate axes remain their respective distances from the body at each grid intersection,

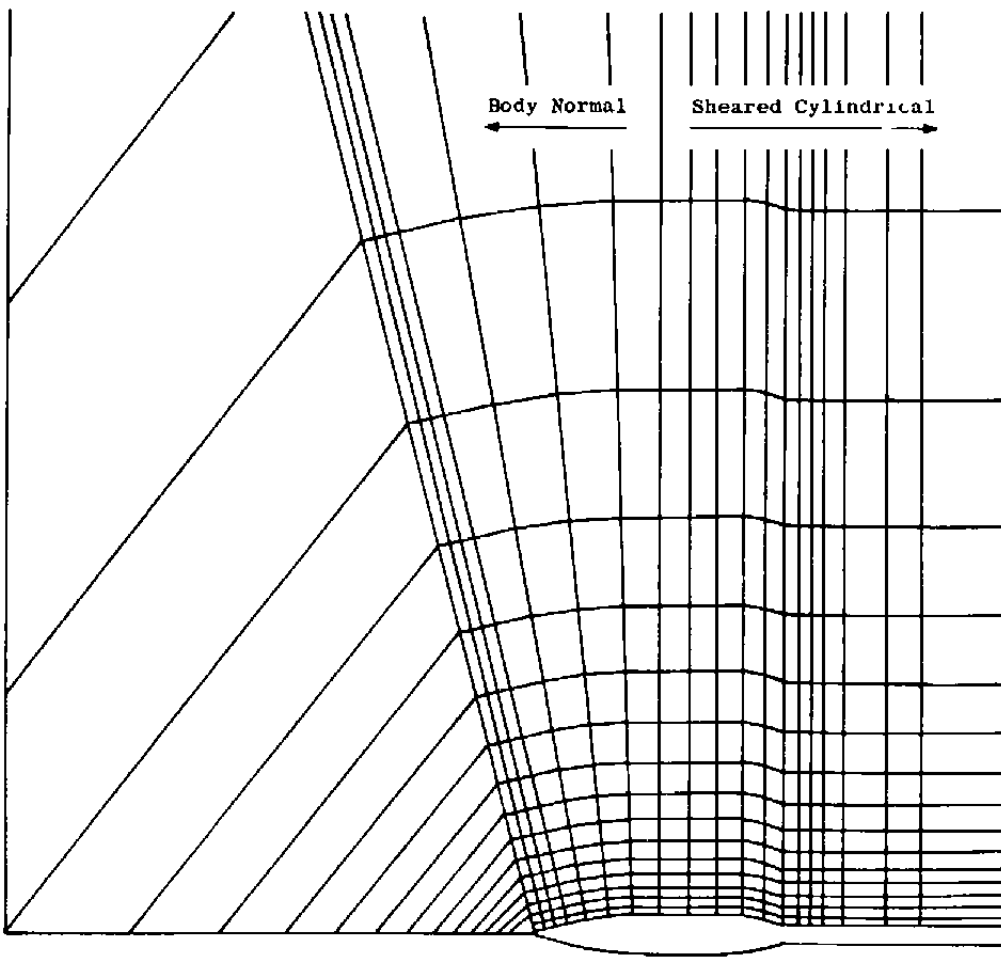


Figure 3. Two coordinate systems used by RAXBOD.

thus attaining a "sheared" configuration matching the body shape. This coordinate system was expressly used to avoid the problems a body-normal system would experience in areas of body concavity, where two or more body-normal coordinates would tend to intersect at large distances from the body, creating computational difficulties. Thus, with the exception of some points in the nose region where the body-normal system is used, RAXBOD is capable of flow calculation over many varied body shapes and is thus satisfactory from the standpoint of the fourth requirement.

Another feature of RAXBOD which lends itself to afterbody configurations with highly sloping shapes is the "Rotated Difference Scheme," which is applied at supersonic points when both velocity components, normal and tangential to the local coordinates, are subsonic. Although South and Jameson point out that the Rotated Difference Scheme is not an exact transformation to an intrinsic coordinate system, it does provide a redefinition of the computational "molecule" to include new points when the flow is not well aligned with the computational coordinates.

The RAXBOD Program thus solves the equation

$$\left(1 - \frac{U^2}{a^2}\right) \frac{1}{H} \frac{\partial}{\partial \xi} \left( \frac{1}{H} \frac{\partial \phi}{\partial \xi} \right) - 2 \frac{UV}{a^2 H} \frac{\partial^2 \phi}{\partial \xi \partial \eta} + \left(1 - \frac{V^2}{a^2}\right) \frac{\partial^2 \phi}{\partial \eta^2} + \left[ \frac{K}{H} \left(1 - \frac{U^2}{a^2}\right) + \frac{\cos \theta}{r} \right] \frac{\partial \phi}{\partial \eta} + \left[ 2 \frac{KUV}{Ha^2} + \frac{\sin \theta}{r} \right] \frac{1}{H} \frac{\partial \phi}{\partial \xi} = 0 \quad (1)$$

in the orthogonal curvilinear coordinate system, where

$$U = \cos \theta + \frac{1}{H} \frac{\partial \phi}{\partial \xi} \quad (2a)$$

and

$$V = -\sin \theta + \frac{\partial \phi}{\partial \eta} . \quad (2b)$$

In the sheared cylindrical system, the equation solved is

$$\begin{aligned} & \left(1 - \frac{U^2}{a^2}\right) \frac{\partial^2 \phi}{\partial \xi^2} - 2 \left[ r'_{bod} \left(1 - \frac{U^2}{a^2}\right) + \frac{UV}{a^2} \right] \frac{\partial^2 \phi}{\partial \xi \partial \eta} \\ & + \left[ \left(1 - \frac{V^2}{a^2}\right) + (r'_{bod})^2 \left(1 - \frac{U^2}{a^2}\right) + 2 \frac{UV}{a^2} r'_{bod} \right] \frac{\partial^2 \phi}{\partial \eta^2} \\ & + \left[ -r''_{bod} \left(1 - \frac{U^2}{a^2}\right) + \frac{1}{r} \right] \frac{\partial \phi}{\partial \eta} = 0, \end{aligned} \quad (3)$$

with

$$U = 1 + \frac{\partial \phi}{\partial \xi} - r'_{bod} \frac{\partial \phi}{\partial \eta} \quad (4a)$$

and

$$V = \frac{\partial \phi}{\partial \eta} . \quad (4b)$$

The boundary conditions are applied at infinity in the forms

$$\phi \rightarrow 0 \text{ as } \eta \rightarrow \infty$$

in both coordinate systems, and, additionally,

$$\theta \rightarrow 0 \text{ as } \xi \rightarrow \infty$$

when the sheared cylindrical coordinates are used. The boundary conditions at the body are

$$v = 0 \rightarrow \frac{\partial \phi}{\partial \eta} = \sin \theta$$

for the orthogonal curvilinear coordinates, and

$$v - Ur'_{bod} = 0 \rightarrow \frac{\partial \phi}{\partial \eta} = \frac{r'_{bod}}{1 + (r'_{bod})^2} \left( 1 + \frac{\partial \phi}{\partial \xi} \right)$$

for the sheared cylindrical system. The computational procedure of South and Jameson also allows for coordinate stretching in the body normal direction near the body, and an independent stretching in the tangential direction in regions where large gradients of the perturbation potential are expected to occur, e.g. the nose and afterbody regions.

The Rotated Difference Scheme is applied in areas of supersonic flow, i.e.

$$a^2 < u^2 + v^2.$$

The basis behind the scheme is to use upwind differences for the second derivatives contributing to  $\phi_{SS}$  and central differences for the contributions to  $\phi_{NN}$ , where these derivatives are in the directions tangential to and normal to the velocity vector, respectively. The derivatives for the orthogonal curvilinear system become

$$\phi_{SS} = \frac{1}{q^2} \left[ \frac{u^2}{H} \frac{\partial}{\partial \xi} \left( \frac{1}{H} \frac{\partial \phi}{\partial \xi} \right) + 2 \frac{uv}{H} \frac{\partial^2 \phi}{\partial \xi \partial \eta} + v^2 \frac{\partial^2 \phi}{\partial \eta^2} \right]$$

and

$$\phi_{NN} = \frac{1}{q^2} \left[ \frac{v^2}{H} \frac{\partial}{\partial \xi} \left( \frac{1}{H} \frac{\partial \phi}{\partial \xi} \right) - 2 \frac{uv}{H} \frac{\partial \phi}{\partial \eta} + u^2 \frac{\partial^2 \phi}{\partial \eta^2} \right]$$

The corresponding equations for the sheared cylindrical system are

$$\begin{aligned} \phi_{SS} = \frac{1}{q^2} & \left[ u^2 \frac{\partial^2 \phi}{\partial \xi^2} + 2u(v - r'_{bod} u) \frac{\partial^2 \phi}{\partial \xi \partial \eta} \right. \\ & \left. + (v - r'_{bod} u)^2 \frac{\partial^2 \phi}{\partial \eta^2} \right] \end{aligned}$$

and

$$\begin{aligned} \phi_{NN} = \frac{1}{q^2} & \left[ v^2 \frac{\partial^2 \phi}{\partial \xi^2} - 2v(u + r'_{bod} v) \frac{\partial^2 \phi}{\partial \xi \partial \eta} \right. \\ & \left. + (u + r'_{bod} v) \frac{\partial^2 \phi}{\partial \eta^2} \right] \end{aligned}$$

The upwind differences for the  $\phi_{SS}$  derivatives are taken in the quadrant in which the velocity vector is located.

Computation time, requirement 5, is also a factor in any relaxation method. South and Jameson used the steady transonic equations with spatial relaxation as opposed to the time-asymptotic method, based on findings by Yoshihara (26) that the latter method was more costly in computer time and storage. To further reduce computation time, RAXBOD begins calculations with a coarse computational grid, for example 25 x 25 points, and upon convergence in this grid system, halves the mesh size and again calculates to convergence.

This "mesh halving" may be repeated, bringing the final mesh to a 97 x 97 point configuration, at a considerable saving, according to South and Jameson, of computation time if the 97 x 97 grid were used throughout (Table II). The present author's experience, based on the two mesh halvings described above, is shown in Table III. While RAXBOD may not be considered an extremely fast program, the computation times involved are reasonable when the complexity and sensitivity of the calculation, as well as the size of the computational grid, are considered.

The RAXBOD program was originally designed to calculate flow over a solid body, the shape of which was well defined, and as such required the body shape to be input as an analytic function or combinations of such functions, such as circular arcs, cylinders, or cones. The first and second derivatives at each longitudinal grid location were then integrated along the length of the body to provide the body shape for computation. As the non-analytic nature of the effective body shape during the course of a viscous/inviscid iteration did not lend itself to such specification, the program was modified to accept body coordinates as input. The required derivatives calculated from neighboring points were provided to the program for subsequent integration using a curve fitting technique based on the work of Akima (27). It is worth noting that the most recent version of RAXBOD (28) has been modified to accept body coordinates directly.

TABLE II

CONVERGENCE HISTORY WITH AND WITHOUT MESH  
HALVING (ADAPTED FROM REF. 24)

Computational Grid	Cycles	$\Delta\phi_{\max}^a$	Time <sup>b</sup>
<b>With Mesh Halving</b>			
25 x 25	36	$4.9 \times 10^{-5}$	6.6
49 x 49	21	$4.7 \times 10^{-5}$	15.3
97 x 97	53	$9.8 \times 10^{-6}$	154.0
<b>No Mesh Halving</b>			
97 x 97	280	$1.0 \times 10^{-5}$	812.0

<sup>a</sup> $\Delta\phi_{\max} = \max \left| \phi_{i,j}^n - \phi_{i,j}^{n-1} \right|$ , n = number of cycles and

$i,j$  is the transonic disturbance potential at grid point  
( $i,j$ ).

<sup>b</sup>CDC 6600 CPU time, seconds.

TABLE III  
TYPICAL COMPUTATION TIMES USING MESH HALVING

Mach Number	(25x25)	Cycles (49x49)	(97x97)	$\Delta\phi_{\max}^a$	Time <sup>b</sup>
0.6	5	16	30	$1.0 \times 10^{-2}$	48.8
0.8	5	19	30		44.2
0.9	6	26	31		47.1
0.95	16	38	48		68.7
1.05	18	26	101		157.2
1.1	20	25	121		184.7
1.2	23	30	119		202.0
1.4	42	68	237	↓	435.8

<sup>a</sup> $\Delta\phi_{\max}$  defined as in Table II.

<sup>b</sup>IBM 370 mod 165 time, seconds.

Viscous Digital Computer Program

The viscous portion of the viscous/inviscid iterative method is no less important than the inviscid portion. Although there exist literally dozens of "boundary layer programs" capable of calculation of the viscous segment of the flow, the requirements of the iteration demand certain characteristics of the program which may be summed up below:

1. the program must be axisymmetric,
2. the program must be able to calculate through strong adverse pressure gradients which are generated by the inviscid program in the early iterations, and
3. computation time must not be excessive.

The five viscous digital computer programs examined were essentially different, as a representative cross-section of solution methods was desired. For purposes of comparison, a hypothetical afterbody/plume shape was assumed (Figure 4), and each program was run under the conditions of zero longitudinal pressure gradient. The body shape was represented in each program by discrete points, and thus the sharp turns in Figure 4 were not really present. The five viscous methods examined were those of Kuhn and Nielsen (29), Tucker (30), Bartz (31), Mayne (32), and Whitfield (33). Of these, the method of Kuhn and Nielsen and the one of Tucker were limited to two-dimensional flows, but the former was studied because of its potential capabilities of boundary-layer calculation in separated flows, and the latter because of its reliability,

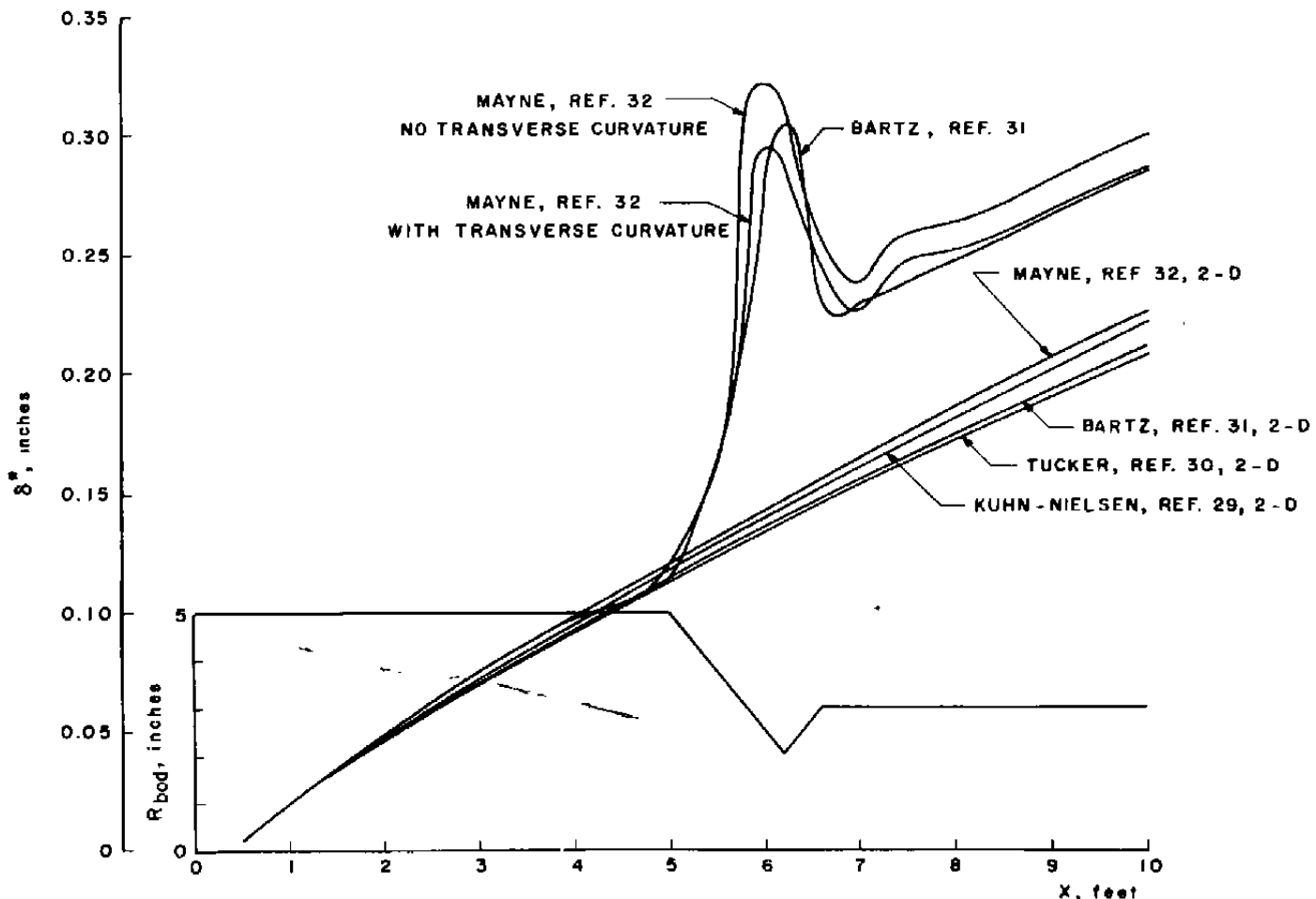


Figure 4. Comparison of the viscous methods.

so as to provide a data base for comparison with the other methods. The hypothetical body shape consisted of a cylinder with a conical afterbody and a conical plume expansion, with the downstream plume shape being assumed a cylinder.

The first three viscous programs (Refs. 29-31) are integral methods, differing in the formulation of the ordinary differential equations and the assumptions inherent in the modeling of the turbulent viscous parameters. The Kuhn-Nielsen Turbulent Separated Boundary Layer Program, however, provides an extension of the usual solution into the realm of separated flows through rearrangement of the independent and dependent variables, thus eliminating the problems encountered with singularities in the boundary layer equations near separation. The program was not used in this "separated mode," however, for the test case. The methods of Mayne and Whitfield (32,33) both are based on the work of Patankar and Spalding (34), but they differ primarily in their treatment of the turbulent viscosity, the former using an eddy viscosity model while the latter using a turbulent kinetic energy approach. Recent work of Chou (35) has indicated that the effects of transverse curvature may be substantial for body fineness ratios of the magnitude associated with the present configurations considered, so the Mayne program calculations were performed not only with the two-dimensional equations, but also with the axisymmetric equations with and without transverse curvature.

As can be seen in Figure 4, page 27, all of the methods agree well in the prediction of the displacement thickness distribution when the two-dimensional equations are used (the results of the Whitfield calculation are not presented as they agreed very well with the other Patankar and Spalding calculation). With the axisymmetric formulation, the results of Bartz and Mayne agree fairly well. In the Mayne calculation, the effect of transverse curvature lessens the axisymmetric displacement thickness rise near the afterbody/plume junction, but compared to the difference between the axisymmetric and two-dimensional predictions, the difference was not thought to be especially significant.

As a result of this test case it was decided that the Kuhn-Nielsen and Tucker program, though both were accurate, could not be considered because of their two-dimensional limitations. Further investigations with the remaining programs involving substantial adverse pressure gradients near the afterbody/plume junction, which were realistic physically, indicated that the integral method, the Bartz program, was more capable of overcoming these gradients than either of the Patankar and Spalding finite-difference methods. Since extremely steep pressure gradients can occur in the initial iterations of the viscous/inviscid method, it was decided that this characteristic of the Bartz program demanded its use in the combined viscous/inviscid formulation. No direct comparisons of the displacement thickness were made, however, between the Bartz and the Mayne programs under adverse pressure gradients for the purpose of judging the accuracy of the programs.

The Bartz solution is based on the numerical integration of the momentum and energy equations in the forms

$$\frac{d\theta}{dz} = \frac{C_f}{2} \left[ 1 + \left( \frac{dr}{dz} \right)^2 \right]^{1/2} - \theta \left[ \frac{2-M^2 + (\delta^*/\theta)}{M \left( 1 + \frac{\gamma-1}{2} \right) M^2} \frac{dM}{dz} + \frac{1}{r} \frac{dr}{dz} \right]$$

and

$$\begin{aligned} \frac{d\phi}{dz} = C_h & \left( \frac{T_{aw} - T_w}{T_o - T_w} \right) \left[ 1 + \left( \frac{dr}{dz} \right)^2 \right]^{1/2} - \phi \left[ \frac{1 - M^2}{M \left( 1 + \frac{\gamma-1}{2} \right) M^2} \frac{dM}{dz} \right. \\ & \left. + \frac{1}{r} \frac{dr}{dz} - \frac{1}{T_o - T_w} \frac{dT_w}{dz} \right], \end{aligned}$$

respectively. The relationship for the skin friction coefficient,  $C_f$ , is based on a correlation developed by Coles, and is derived in Appendix A, Bartz (31) :

$$C_f = \frac{0.0256}{(R_\theta)^{1/4}} \left( \frac{T_{aw}}{T} \right)^{-0.6}$$

The Stanton number,  $C_h$ , is represented by the relationship based on the Prandtl number correction to the Reynolds analogy due to von Kármán, which is also derived in Appendix A of Reference (31), of the form

$$C_h = \frac{\frac{C_f(R_\phi)}{2} (\phi/\theta)^{0.1}}{1 - 5 \left[ \frac{C_f(R_\phi)}{2} \right]^{1/2} \left[ 1 - Pr + \ln \frac{6}{5Pr+1} \right]}$$

Once these two relationships are assumed, the integration of the momentum and energy equations may proceed once the Mach number distribution at the edge of the boundary layer and the initial shape parameter,  $\delta^*/\theta$ , are specified. The former distribution is provided by the inviscid calculation, and the latter by assuming a velocity and stagnation temperature distribution through the boundary layer. Bartz uses a 1/7th-power law distribution for both the velocity and stagnation temperature variation (actually,  $T_o - T_w$ ).

Typical run time for the Bartz program along the entire length of a body under a varying pressure distribution is about twenty-five CPU seconds on the IBM 370 mod 165.

#### Plume Calculation

In order to analyze the flow over a boattail with a real exhaust plume, it is necessary to be able to determine the "shape" of the plume, recognizing that the shape must be a simplification of the quite complex flow actually encountered (36). When viscous effects are considered, the actual shape of the plume is open to question, and one may choose to define the shape using a "dividing-streamline" measure or a certain percentage of the difference between the plume and external velocities, to cite two examples. If viscous effects are ignored, however, the merging of the plume and external flows, both considered to be inviscid, determine a

well-defined boundary between the two flows. This boundary is referred to as the "inviscid plume boundary" or "inviscid reference line."

The importance of the inviscid plume boundary is that (1) it serves as the basic solid body shape of the plume, which is the basis for the aforementioned solid-body or displacement effect of the plume, and (2) it is the reference line to which corrections to the plume shape due to entrainment effects are applied.

The plume shape is calculated using a Method of Characteristics (MOC) digital computer program produced by the Lockheed Missiles and Space Company (37). This program is one of a group of programs used by Lockheed to analyze various aspects of the nozzle exhaust plume flow problems as well as external transonic flows and forces and moments on objects immersed in such flows. The Lockheed MOC program used in these studies is valid for ideal or real gases in supersonic compressible flow, and two-dimensional or axisymmetric geometry may be used. It has a number of starting options for the flows, and either solid walls or free boundaries may be specified downstream of the starting point, with capability

of switching from a solid boundary to a free boundary at the user's option. This characteristic makes the program ideal for those cases where it is desirable to begin the plume calculation within the nozzle, for example at the sonic line in the throat of a converging-diverging nozzle, and to continue it past the lip at the exit of the nozzle. In cases where the nozzle is sonic, that is, the throat of the nozzle is at the exit plane, the calculation may be started at this point and the flow is calculated immediately into the free-boundary region.

When used to furnish the plume shape for the viscous/inviscid iteration, the program is supplied the nozzle pressure ratio of the exhaust and external flows, i.e. the nozzle total pressure divided by the free-stream static pressure, the exhaust total temperature, pertinent gas constants, the Mach number distribution of the starting line, and the proper boundary conditions. The calculation runs less than ten seconds CPU time on the IBM 370 mod 165. Some examples of actual typical plume shapes are shown in Figure 5. The solid lines represent the plume as calculated by the Lockheed program, but the plumes were extended as shown by the dashed lines. The difference in  $C_p$  distribution on the boattail caused by this simplification of plume shape was minor.

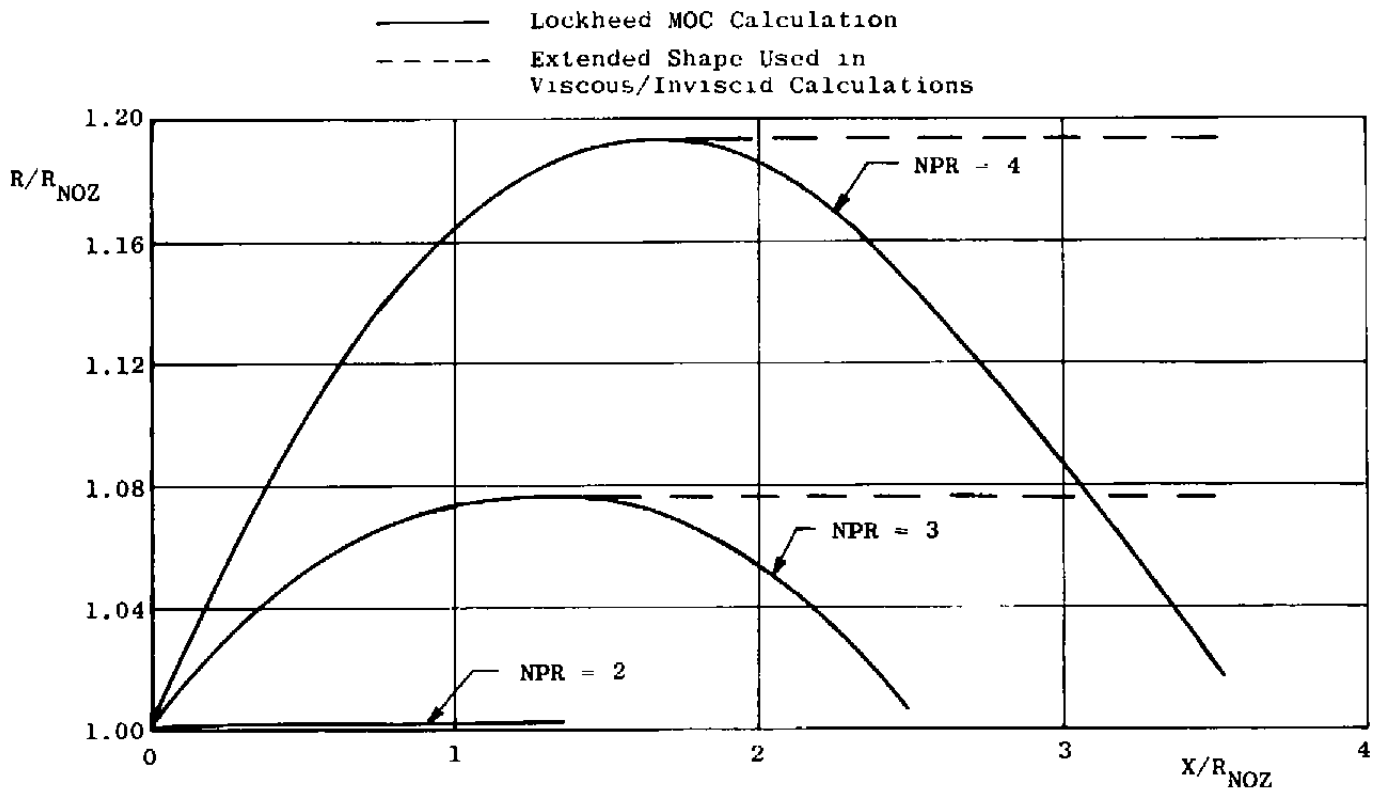


Figure 5. Plume shape as a function of nozzle pressure ratio.

Combined Viscous/Inviscid Iterative Program

The general method for the iterative solution of the type previously described is shown in the flow chart in Figure 6. As can be noticed immediately, the technique involves two main iteration loops, an "inviscid/inviscid" (I/I) loop and the "viscous/inviscid" (V/I) loop. The former loop is an iteration between the external and exhaust inviscid flows with the purpose of modifying the inviscid plume shape according to the pressure distribution on its surface as calculated by the external inviscid program. When the plume shape, which is, in the ideal case, calculated from a longitudinal pressure distribution, causes the external inviscid program to return essentially the same pressure distribution, the iteration is considered to be converged. At this point the V/I loop, which has been described, is entered. Upon convergence of the V/I loop further refinements of the solution may be carried out by returning to the I/I loop with the new effective body shape calculated in the V/I loop.

The Combined Viscous Inviscid (CVI) program performs only the calculations in the V/I loop, that is to say, the running of the two inviscid programs in the I/I loop and the transferral of converged data to the V/I loop are carried out manually. Manual operation of this portion of the complete problem is not an undue hardship, for in the many cases where the body to be analyzed has a solid sting, the I/I loop is not required, and in real plume cases it has been found that more than one iteration is usually not necessary for a

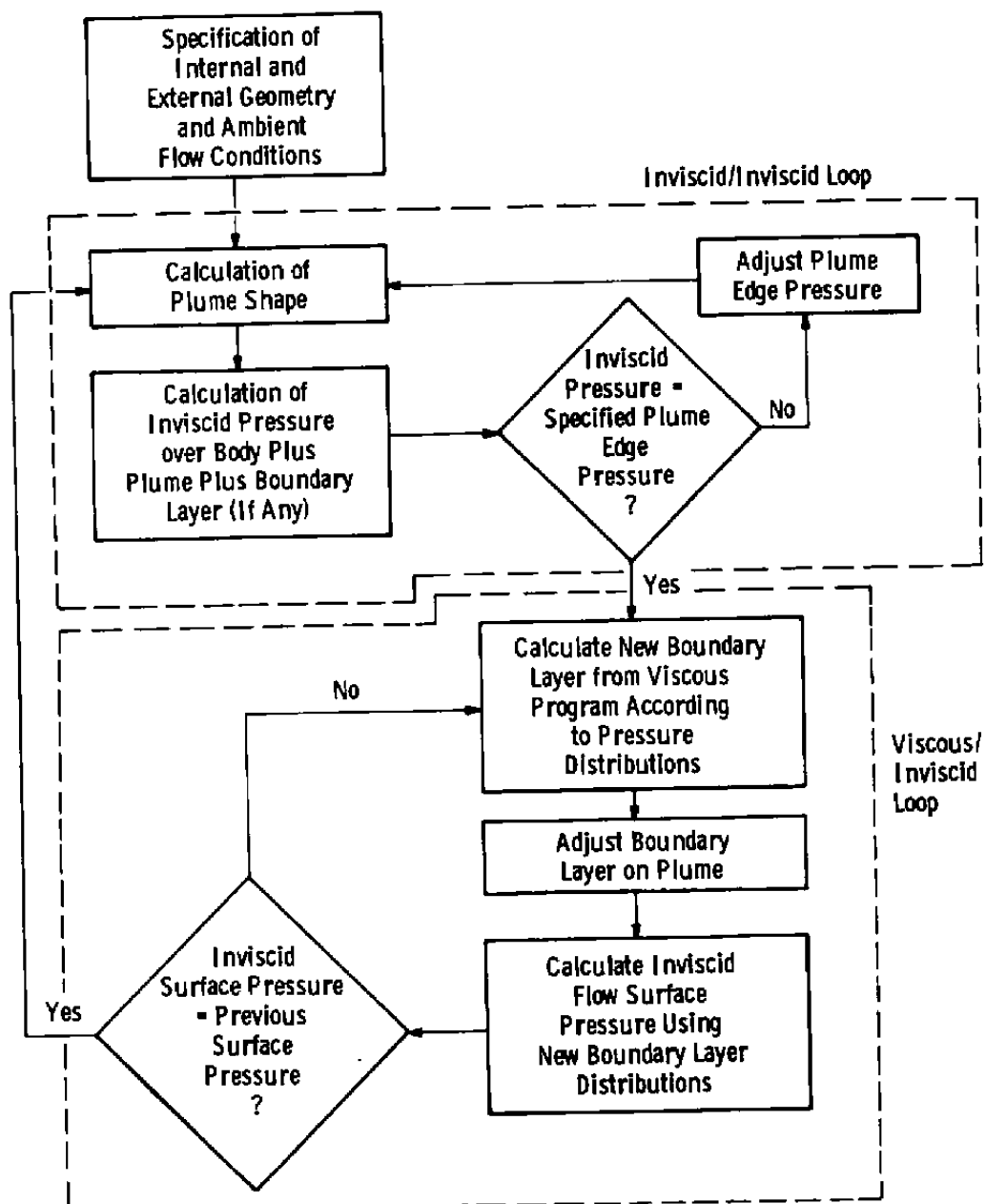


Figure 6. General iteration flow plan.

realistic converged plume shape. In fact, the plume shape as determined from the nozzle pressure ratio pertaining to the ambient external flow is usually very close to the plume shape developed to convergence in the I/I loop, and it is used in the calculations herein. The following discussion will therefore concentrate on input requirements for a given problem and the operation of the CVI program, and the converged inviscid plume shape (or solid sting shape) will be assumed known.

When confronted with a new body configuration, the South-Jameson Transonic Program (RAXBOD) is usually run a number of times for the purpose of obtaining an inviscid solution for the body with no boundary layer. RAXBOD has a number of parameters which control the operation of the program, and it is thus advisable to "tune" the program itself before embarking on a full run with the CVI program. Table IV lists the most important input requirements for RAXBOD along with typical values. Parameters that control output functions, such as card punching or plotting, and parameters that remain the same for most runs are not included in this table.

A brief elaboration on some of the parameters presented in Table IV is in order because of their importance in the operation of RAXBOD. The stretching parameters at the body nose, DSDXIO and BZ, are adjusted so as to provide a nearly square grid at that location. Failure to do this may result in unrealistic solutions in the area of the nose or

TABLE IV  
INPUT TO THE SOUTH-JAMESON TRANSONIC PROGRAM (RAXBOD)

Parameter Name(s)	Explanation	Typical Value(s)
KKN	Number of (XP,YP) body input coordinates	97
XP,YP	(XP,YP) body coordinates	XP=0.0,0.2,..., 70.6,71.4 YP=0.0,0.1,..., 2.3,2.3
IMAX,JMAX	Initial number of XP and YP grids	25,25
MIT	Maximum number of iterations <sup>a</sup>	200
MHALF	Number of mesh halvings	2
COVERG	Convergence limit of transonic disturbance potential <sup>b</sup>	0.001
QF3	Relaxation parameter	0.5
DSDXIO	Stretching parameter for the tangential coordinate system at the body nose	1.0
BZ	Stretching parameter for the normal coordinate system at the body nose	0.0135
DSDXIM	Stretching parameter for the tangential coordinate system in the afterbody region	1.0
X1	XP location of beginning of sheared cylindrical coordinate system	35.6
SMAX	Maximum body length coordinate	71.0
GAM	Ratio of specific heats	1.4
AMINF	Free-stream Mach number	0.8

<sup>a</sup>MIT halved at each mesh halving

<sup>b</sup>Convergence occurs when  $\Delta\phi_{\max} \leq \text{COVERG}$ , where  $\Delta\phi_{\max}$  is defined in Table II, page 24

even lack of convergence. The parameter QF3, which is the relaxation parameter in the South-Jameson finite-difference scheme, assists convergence when it is close to or equal to 0.5 at a small penalty in CPU time. Lower values of QF3 may radically effect the capability of converging for a given body shape and Mach number. Finally, the sheared cylindrical coordinate system, controlled by X1, should be begun ahead of any concavity in the body shape to eliminate any possibility of body-normal coordinate axes intersecting at large distances from the body.

Once an acceptable "body-alone" solution has been obtained from the RAXBOD program, the CVI program may be used for the viscous/inviscid iterative calculations. Required inputs for this program are those of the RAXBOD program plus additional parameters to be used by the viscous portion of the iteration. The most important of these parameters are presented in Table V. It will be noted that there is some duplication of parameters between the inviscid and viscous input, but this was retained so that if difficulties were encountered in the CVI program, the pertinent input data could be transferred directly into either the inviscid or viscous program in order to resolve the particular problem.

The CVI program begins its iterative procedure with an inviscid calculation of the flow about the body with zero boundary layer displacement thickness. This computation is referred to as the "zeroth" iteration, as it is a repeat of the inviscid calculation previously made using RAXBOD alone

TABLE V

## INPUT FOR THE VISCOUS PORTION OF THE CVI PROGRAM

Parameter Name(s)	Explanation	Typical Value(s)
IXTAB	Number of (X,Y) body input coordinates	97
X,Y	(X,Y) body coordinates	X=0.0,0.2,..., 70.6,71.4 (in.) Y=0.0,0.1,..., 2.3,2.3 (in.)
MZETA	Velocity profile power law exponent	7
ITWTAB	Wall temperature option: Adiabatic = -1, Constant = 0, Table = 1	-1
TO	Free-stream stagnation temperature	580 (°R)
PO	Free-stream stagnation pressure	2000 (psf)
GAMD	Ratio of specific heats	1.4
PRANDL	Stagnation Prandtl number	0.7
ZMU0	Viscosity at stagnation temperature	$1.29 \times 10^{-5}$ (lbm/ft-sec)
THETAI	Initial value of momentum thickness	$1.0 \times 10^{-4}$ (ft)
PHII	Initial value of energy thickness	$1.8 \times 10^{-4}$ (ft)
EPSZ	Geometry: Asixymmetric = 1, Two-dimensional = 0	1

during the "tuning" operation. The purpose of the zeroth iteration is to provide the viscous program with an initial longitudinal pressure distribution over the length of the body. It is during the zeroth iteration, and perhaps the next one or two iterations, that unusually steep pressure gradients and extreme pressures may develop, and the boundary layer displacement thickness, which tends to ameliorate the flow expansion and compression in the area of the afterbody, is either non-existent or very small.

The RAXBOD program, irrespective of the (XP,YP) body coordinate pairs furnished as input, provides the converged pressure distribution at longitudinal locations which are functions of the parameters DSDXIO, X1, and SMAX (see Table IV, page 38). Care must be taken that the (X,Y) body coordinate pairs input to the viscous portion of the CVI program (Table V) correspond exactly to the RAXBOD pairs, which have been previously determined during the tuning of the program. Slight errors in the longitudinal location of the pressures may result in erroneous converged solutions of the CVI program, especially in regions of rapidly changing body geometry. Once the boundary layer has been calculated by the viscous portion of the CVI program, the (XP,YP) coordinates of the new effective body are transferred back to the inviscid program using the following relationships (see Figure 7).

$$XP = X_{bod} + \delta * \sin \theta_{bod} = X_{bod} + \delta * \frac{Y'_{bod}}{\sqrt{1 + (Y'_{bod})^2}}$$

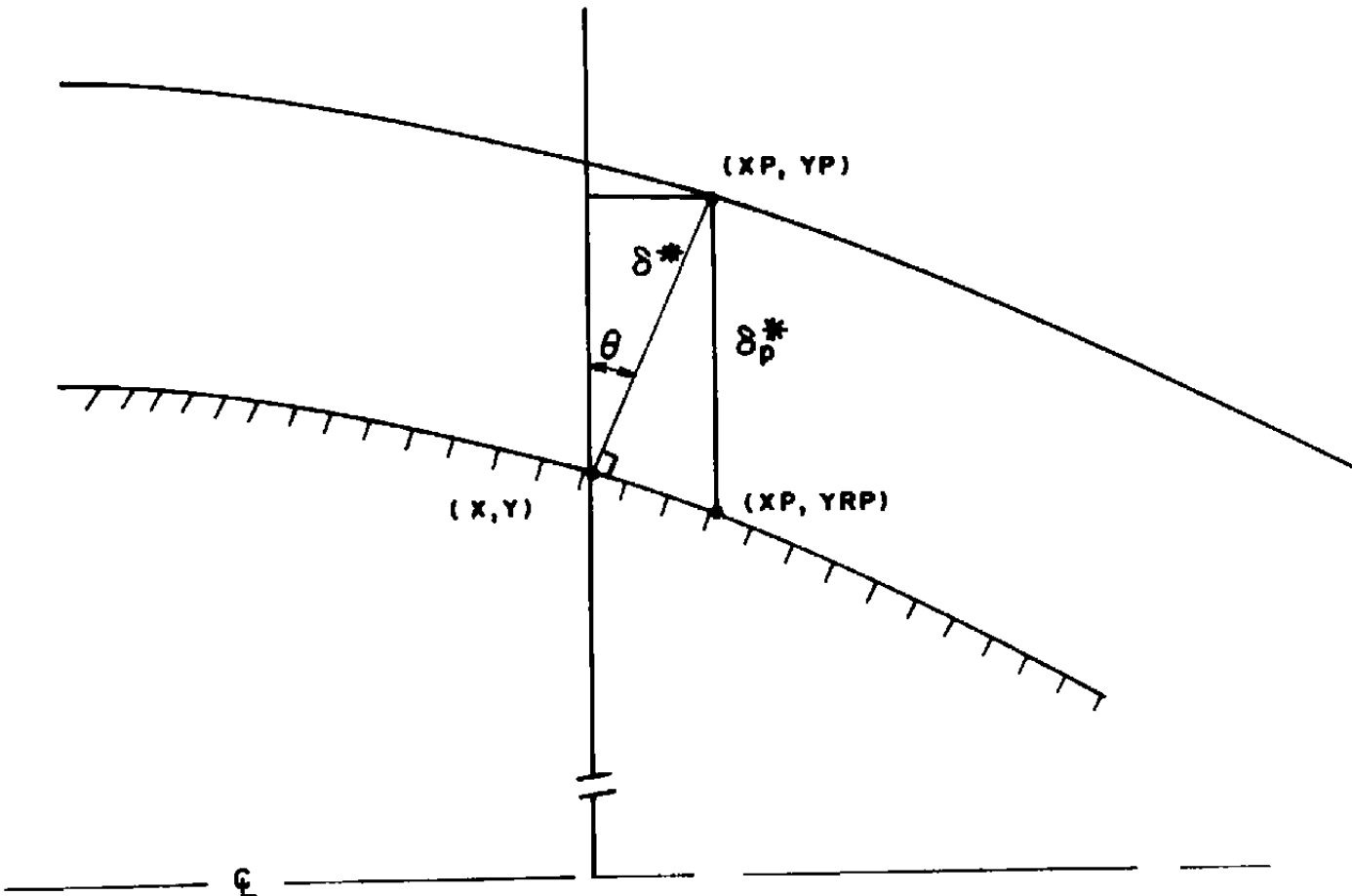


Figure 7. Boundary layer coordinate system used in the viscous portion of the CVI program.

and

$$Y_P = Y_{bod} + \delta^* \cos \theta_{bod} = Y_{bod} + \delta^* \frac{1}{\sqrt{1+(Y'_{bod})^2}},$$

where the longitudinal derivative of the body shape at  $(X, Y)$ , that is,  $Y'_{bod}$ , is calculated numerically. Similarly, the displacement thickness at  $XP$  is then calculated by

$$\delta_p^* = Y_P - Y_{RP},$$

where the body radius at  $XP$ , i.e.  $Y_{RP}$ , is calculated by interpolation using the body coordinates that were input to the viscous program.

With these coordinates of the new effective body, the inviscid calculation is repeated, and a new longitudinal pressure distribution is calculated. This point is then the end of the first complete viscous/inviscid iteration, and the pressure distribution may be compared with that resulting from the zeroth iteration. If there is good agreement between the two pressure distributions, a highly unlikely occurrence, the solution is considered to be converged. If, as is more likely the case at this early stage of the viscous/inviscid iteration, there is little agreement, the second iteration is begun using the pressure calculated at the end of the first iteration. This process is continued until convergence of the pressure distributions is satisfactory.

It has been found helpful, and in some cases necessary, to reduce the amount of the displacement thickness added at each iteration, thus providing a form of "relaxation"

of the incremental displacement thickness. This technique is shown schematically in Figure 8, where  $\delta_p^{*n-1}$  represents the displacement thickness that was used in the (n-1)-st viscous/inviscid iteration, and  $\delta_p^{*n}$  represents the displacement thickness calculated during the n-th iteration based on the pressure distribution from the (n-1)-st iteration. Rather than use the whole magnitude of  $\delta_p^{*n}$ , a "relaxed" displacement thickness is defined:

$$\delta_p^{*n}_{\text{rel}} \equiv \delta_p^{*n-1} + R (\delta_p^{*n} - \delta_p^{*n-1}),$$

where  $R$  is a relaxation factor,

$$0 < R \leq 1,$$

which is usually between 0.3 and 0.6, depending on the severity of the body geometry and flow conditions.

The necessity for such a relaxation arises because of the sensitivity of the transonic flow to small changes in body shape and the resulting effect on the viscous calculations.

An extreme pressure, say at the afterbody plume (or sting) junction, may produce a very large displacement thickness from the viscous program calculations which, at the next inviscid computation, may then result in too low a pressure. This low pressure may then cause an unrealistically low displacement thickness, causing too high a compression in the next inviscid calculation, and then once again, too large a displacement thickness at that point. The solution will then

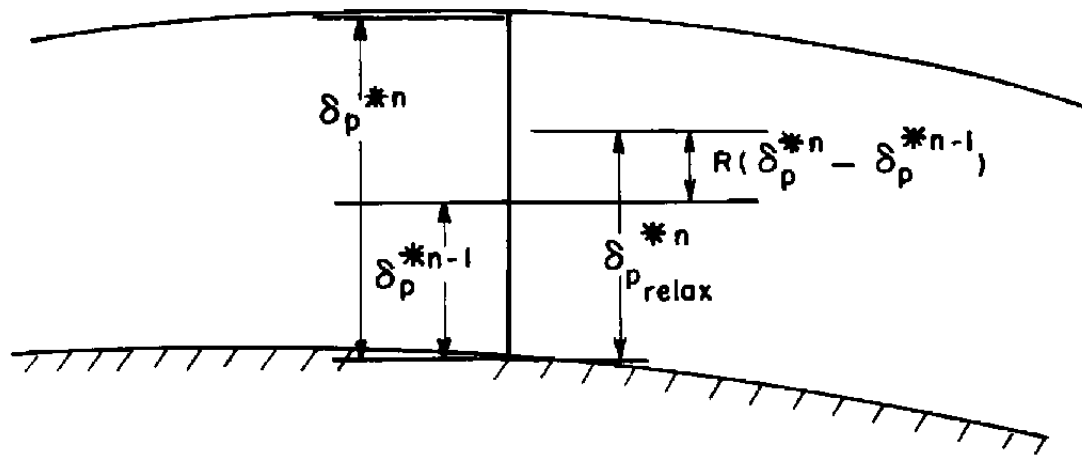


Figure 8. Schematic diagram of boundary layer displacement thickness relaxation technique.

tend not to converge, but to oscillate between two distinct solutions. Relaxation of the displacement thickness increment will greatly aid in reducing the probabilities of such tendencies.

Figure 9 shows the maximum difference in  $C_p$  along the body between a given iteration and the previous iteration for four values of relaxation factor,  $R$ . The body being considered is a sting-mounted cylindrical model with a circular arc afterbody of length to maximum diameter ratio of 1.768, (38). The convergence of the solution with  $R = 1.0$ , which corresponds to no relaxation, is doubtful and the oscillation between two solutions is implied by the regular sawtooth pattern above  $\Delta C_{p\max} = 0$  starting with the thirteenth iteration. A relaxation factor of 0.7 improves the situation, but there is a lightly damped oscillation up to the fifteenth iteration. For values of  $R$  of 0.5 and 0.3, the solution converges rapidly and definitely with no tendency to oscillate in a regular pattern. Both of these relaxation factors would be acceptable from the standpoint of a relatively quick and reliable solution, but the  $R = 0.5$  case seems to be slightly quicker in converging. It should be mentioned that the three lower values of  $R$  converge to the same solution.

Figure 10 shows the pressure coefficient, the effective body shape, displacement thickness as computed by the viscous program, and the build-up of the relaxed displacement thickness in the area of the afterbody and sting by a value of  $R = 0.3$ . At convergence, the relaxed displacement

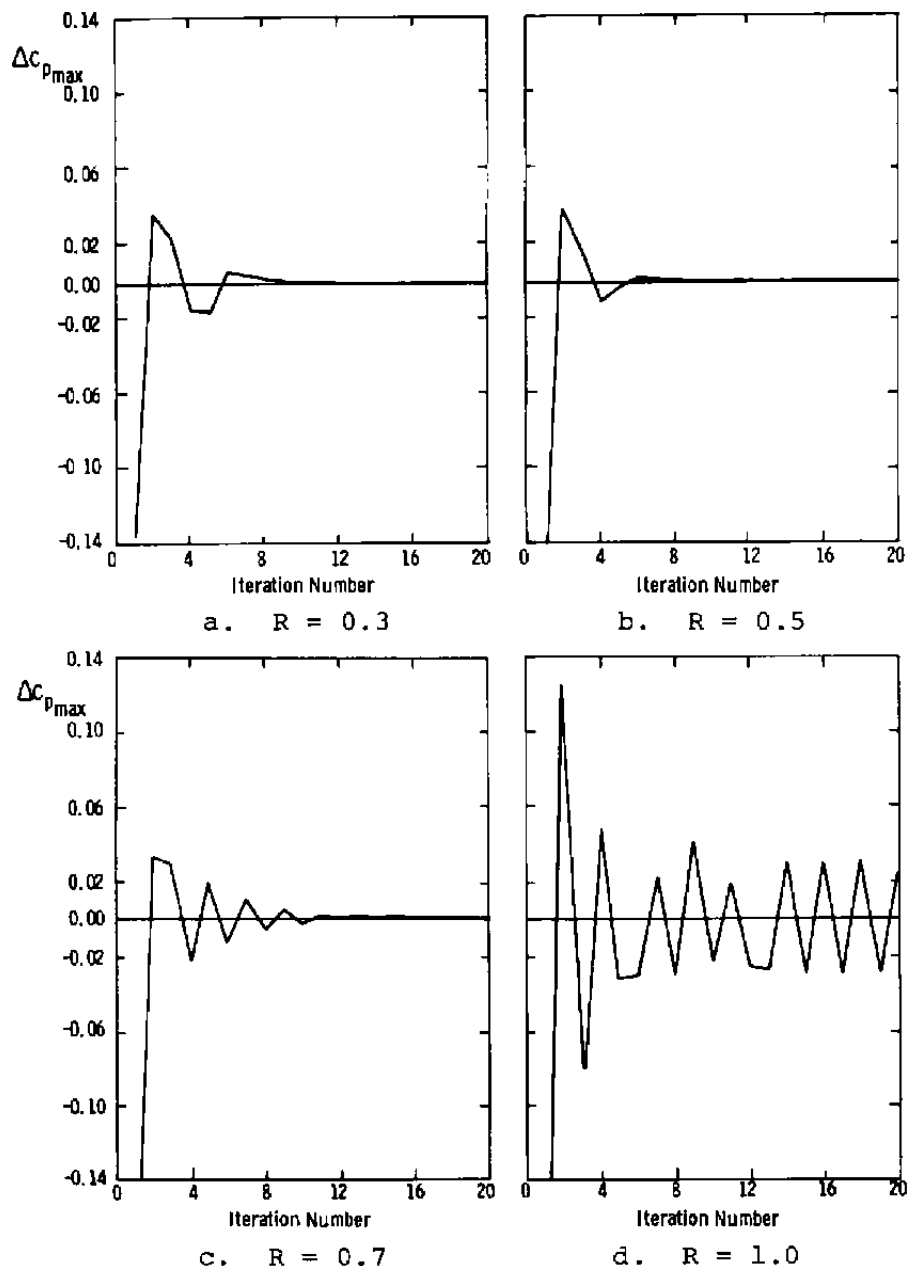


Figure 9. Effect of relaxation factor on convergence,  
 NASA Langley  $l/d_m = 1.768$  afterbody,  $M_\infty = 0.8$ ,  $Re/l = 3.8 \times 10^6$  ft-l.

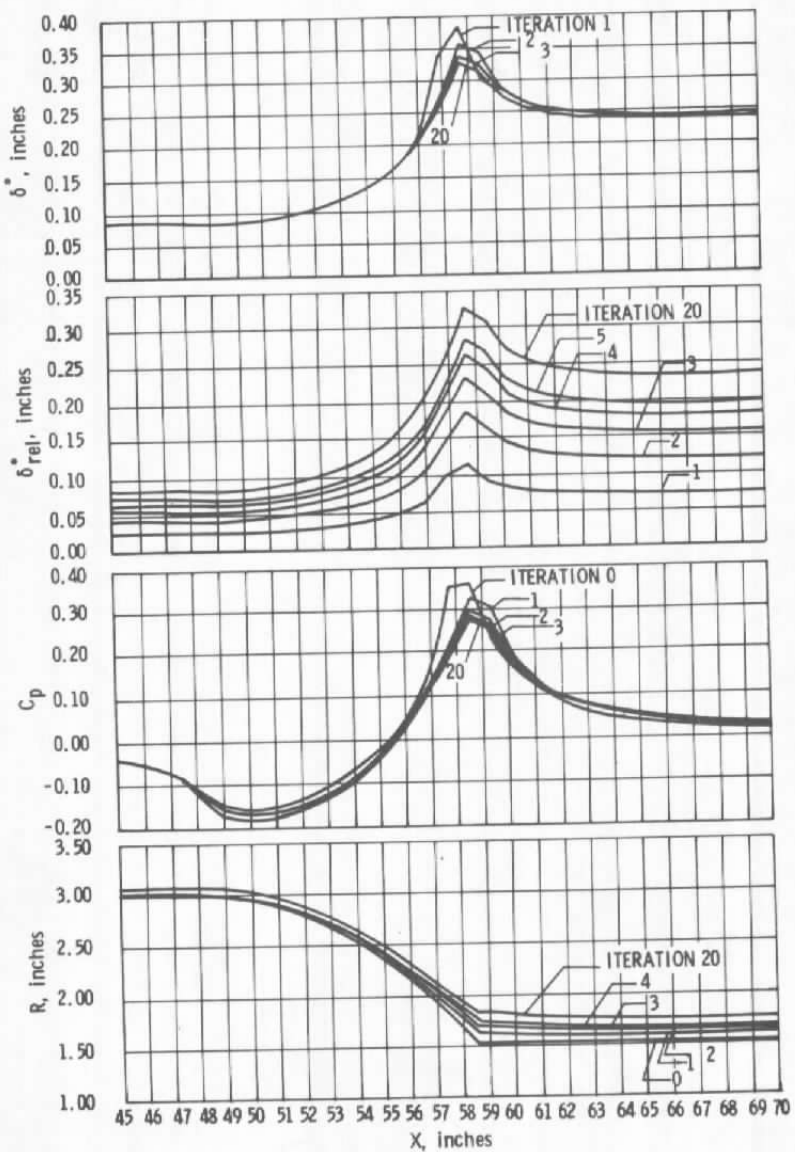


Figure 10. Characteristic pressure, effective body shapes, and displacement thickness distribution of a converging viscous/inviscid iteration.

thickness attains the value of the actual displacement thickness along the body, and this may be seen at high iteration numbers in Figure 11. In this same figure, the relaxation factor may be obtained from the slope of the first iteration line. Figure 12 shows the magnitude of the oscillating pressure coefficient and relaxed displacement thickness for the case of  $R = 1.0$  relative to the well-converged  $R = 0.3$  case. It can be seen that the  $R = 1.0$  solutions for the nineteenth and twentieth iterations bracket the converged  $R = 0.3$  solution, and convergence of the  $R = 1.0$  solutions toward this solution is extremely slow, if at all.

The criterion for convergence of the viscous/inviscid iteration is usually assumed to be  $\Delta C_{p_{max}} \leq 0.001$ , as this is on the order of one-tenth of one percent of the stagnation pressure coefficient and is also less than one percent of the pressure coefficient range in the area of the afterbody and plume. However, each case is examined individually to ensure that the solution exhibits no tendencies toward divergence.

The CVI Program is neither a small program with regard to computer core storage nor a fast program with regard to CPU run times. By far the largest portion of the core storage and run time requirements are attributable to the inviscid portion of the iteration, RAXBOD. It has been found that the tight convergence requirement quoted by South and Jameson on  $\Delta \phi_{max}$  (see Table II, page 24) may be reduced during the course of the viscous/inviscid iteration from 0.0001 to 0.01 with no appreciable change in the converged solution.

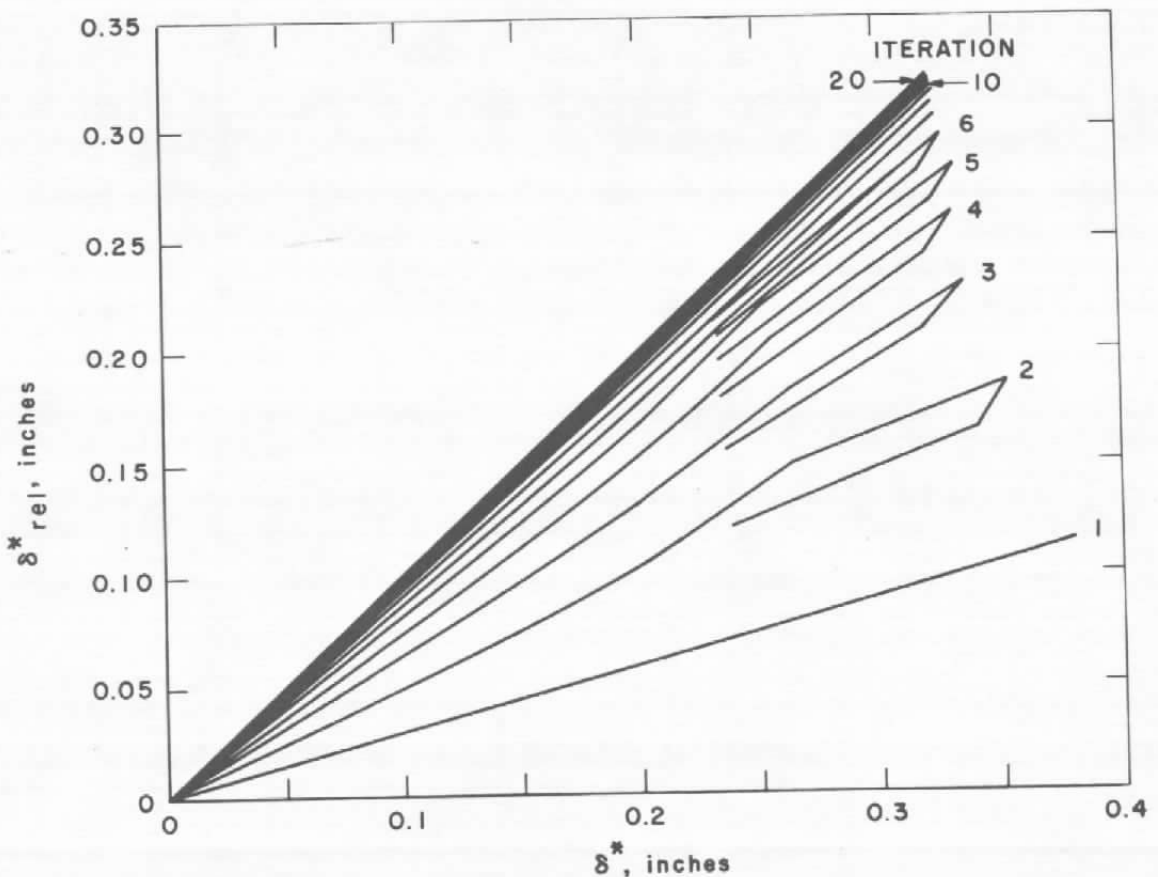


Figure 11. Boundary layer relaxation displacement thickness development relative to calculated displacement thickness.

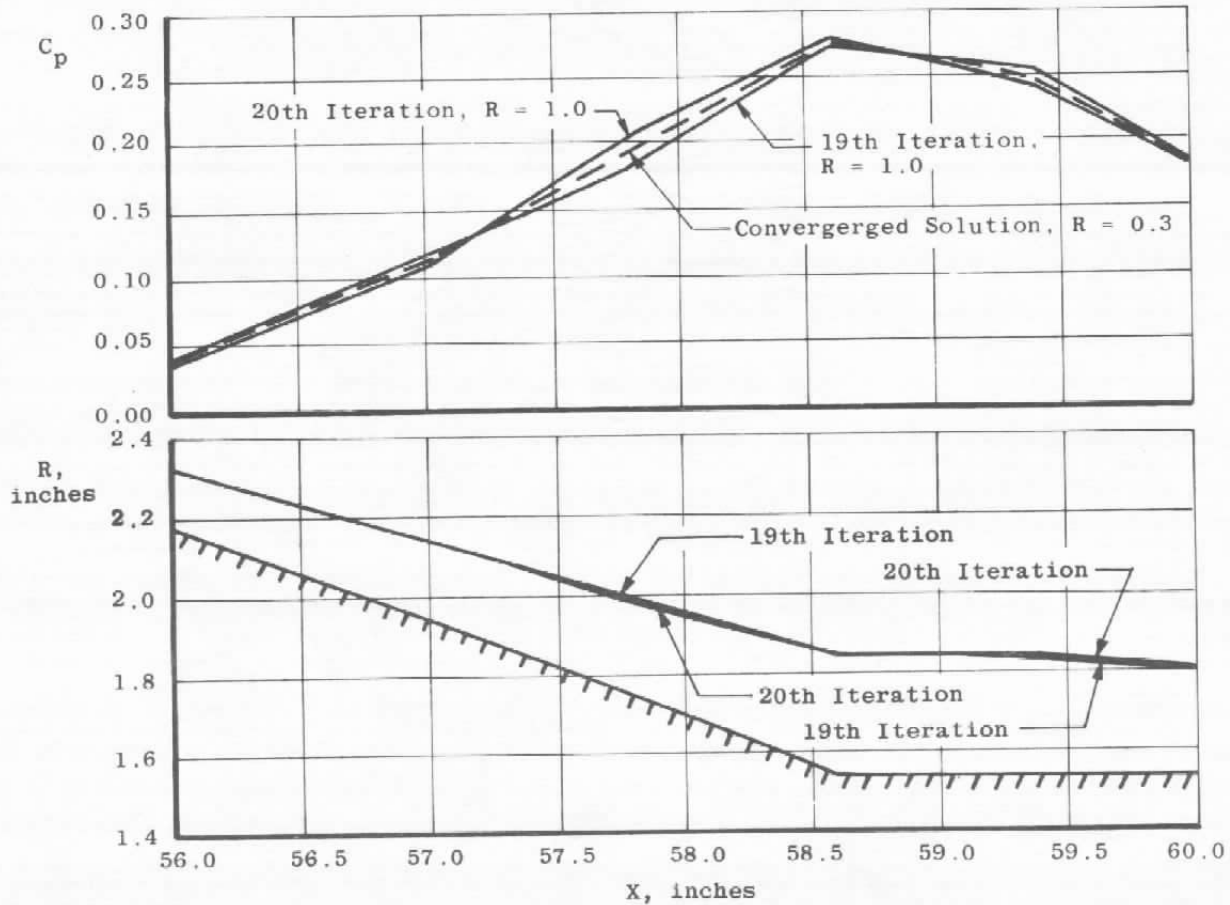


Figure 12. Comparison of the oscillating solution of an  $R = 1.0$  case and the converged solution of an  $R = 0.3$  case.

Even with this and similar methods of making the CVI Program more efficient, the version of the program currently in use requires 540 kilo-bytes of storage, and a typical case will use approximately 30 to 45 minutes of CPU time.

## CHAPTER III

## MIXING ANALYSIS AND THE PLUME ENTRAINMENT MODEL

Introductory Remarks

As was described in the beginning of Chapter II, the effect of a real plume on the external flow over an afterbody may be considered as consisting of two components: (1) a blockage or displacement effect, which causes the external flow to react to the plume by deflecting as if it were a solid body, and (2) an entrainment effect, which accelerates the external flow through the turbulent momentum exchange mechanism between the two flows. If the first effect is treated by considering the plume to be a solid body, as shown in Figure 2, page 14, then the second effect may be approximated by a suitable modification of this solid body plume shape. It is the purpose of this chapter to derive the necessary relationship for the calculation of an effective plume boundary layer displacement thickness correction,  $\delta_e^*$ , relative to the known Inviscid Reference Line (IRL).

The method of analysis used to calculate the displacement thickness correction is based on the mixing analysis usually attributed to Chapman and Korst. The development of this method, in which emphasis was placed on the base flow problem, is presented in References (39-45). Most of the early efforts assumed no initial boundary layer profile which

led to fully developed solutions with velocity profiles of the error function type. Hill (46), following the general method of Chapman and Korst, took the initial boundary layer effect into account in the base flow problem in two ways. In the first, he assumed fully developed velocity profiles for simplicity of computation, but with the origin of the coordinate system displaced so that the "equivalent mixing flow" had the same mass and momentum fluxes as the initial boundary layer flows. In the second, he assumed a linear variation of the eddy viscosity but with no assumption of fully developed velocity profiles. Both methods yielded satisfactory results. Bauer and Matz (47) approached the initial boundary layer problem by applying the principle of conservation of momentum below the dividing streamlines of the two flows and Prandtl's Mixing Length Theory to obtain a streamwise distribution of the shear stress. Bauer's Integral Method (48) was then used for the solution of the resulting relationships. Bauer and Fox (49) have extended this method, using the turbulent kinetic energy (TKE) method, to supersonic nozzle afterbody flows.

The method used in the following analysis is based on the work of Childs (50) and Korst and Chow (51), but is extended to provide the effects of initial boundary layers on all pertinent quantities.

#### Mixing Analysis

The basic flow model to which this mixing analysis

was applied is shown in Figure 13. Two flows, both with initial boundary layers, begin mixing at the end of an infinitely thin flat plate,  $x = 0$ . This point represents the nozzle/afterbody and plume junction. Further downstream, at  $x = x_2$ , after sufficient momentum exchange, the velocity profile attains a smooth, fully developed form with very little indication of the presence of any initial boundary layers. The fully developed velocity profile is characteristic also of the family of profiles formed by the mixing of two uniform streams, i.e. with no initial boundary layers, and it was using this simplified form of the velocity distribution that Korst and Chow developed their analytical results. It was recognized, however, that the initial boundary layers, particularly on the afterbody, could be comparable in size to the dimensions of the afterbody and thus could not be ignored. This analysis will retain the initial boundary layer terms in the velocity profile function and other quantities developed in the derivation.

The most serious restriction within this analysis is that of two-dimensionality of the flow. It was determined, by reviewing the results of previously referenced work on free turbulent mixing, that the displacement thickness correction applied to the plume would be small in comparison with the radius of the plume for the geometric, aerodynamic, and thermodynamic parameters typical of nozzle/afterbody flows. Thus, the axisymmetric effects would normally be of a lower order and could be ignored in the present analysis.

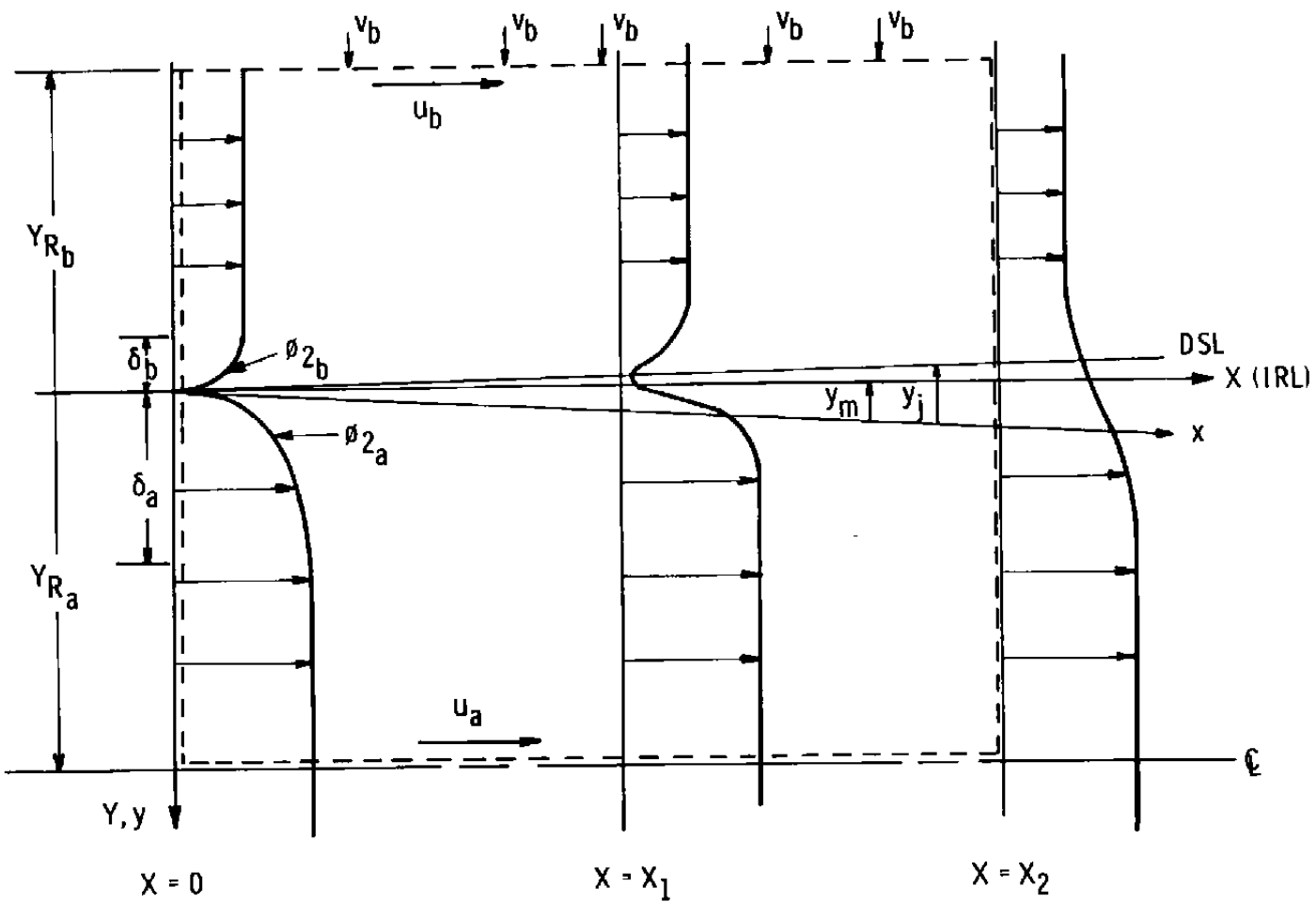


Figure 13. Schematic diagram of the jet mixing region.

Furthermore, it was felt that the availability of theoretical and experimental results for the case of two-dimensional mixing would provide a valuable means of checking the present computation.

The analysis is valid for compressible, turbulent, non-isoenergetic attached flow with a turbulent Prandtl number assumed to be unity. The mixing is furthermore assumed to be isobaric. This is consistent with the approach of Korst and Chow, but is not fully realistic considering the longitudinal pressure distributions occurring in nozzle/afterbody plume flows. However, even though the pressure at the nozzle/afterbody and plume junction may become quite large, recovery to free-stream conditions is usually rapid. It was concluded that this tendency toward rapid pressure recovery and the dominance of the turbulent mixing mechanism would make the isobaric assumption acceptable or, at any rate, introduce no more error than the constant pressure assumption used in the calculation of the inviscid plume shape.

The physical coordinate system, shown in Figure 13, consists of the orthogonal  $\{X, Y\}$  axes, and the inviscid reference line (IRL), or plume boundary, is a straight line coincident with the  $X$ -axis. The physical coordinate system is aligned with the reference flow, the lower flow in Figure 13, which corresponds to the nozzle jet flow. A constant transverse velocity,  $v_b$ , is assumed in the upper flow at a large but finite distance from the  $X$ -axis, corresponding to mass entrainment of the external flow. No corresponding

transverse velocity is assumed for the lower flow, as the physical axes are aligned with this flow and, furthermore, a large and finite distance in this direction could be made to lie on the actual nozzle centerline, about which the flow is symmetric. The transverse velocity is required to provide sufficient mass to attain the fully-developed velocity profile without suffering a velocity deficit elsewhere, analogous to the results of Moulden (52).

The equation of motion for the isobaric mixing may be written as

$$u \frac{\partial u}{\partial x} + v \frac{\partial u}{\partial y} = \epsilon \frac{\partial^2 u}{\partial y^2} \quad (5)$$

where  $\epsilon$  is the eddy viscosity for the turbulent flow. Dimensionless variables are introduced,

$$\phi = \frac{u}{u_a} \quad \psi = \frac{x}{\delta_a} \quad \zeta = \frac{y}{\delta_a}$$

and the eddy viscosity is assumed to be of the form

$$\epsilon = \epsilon_\infty f(\psi)$$

where  $f(\psi)$  is an undetermined function that approaches unity as  $\psi \rightarrow \infty$ , and  $\epsilon_\infty$  is defined, according to Görtler (53), as

$$\epsilon_\infty = \frac{1}{4\sigma^2} \times (u_a + u_b)$$

If, furthermore, it is assumed that  $v$  is negligible and that the non-linear coefficient  $u$  can be approximated by

$$u = \frac{u_a + u_b}{2} ,$$

which is consistent with the small perturbation analysis of Pai (54), then Equation (5) becomes the heat conduction equation with a diffusivity of one:

$$\frac{\partial \phi}{\partial \xi} = \frac{\partial^2 \phi}{\partial \xi^2} \quad (6)$$

$$\text{where } \xi = \frac{1}{2\sigma^2} \int_0^\psi \overline{J} f(\overline{\psi}) d\overline{\psi}.$$

The boundary conditions applicable to this equation are, for the initial velocity profiles,

$$\begin{aligned} \phi(0, \xi) &= \phi_b & \text{for } -\infty < \xi \leq -\frac{\delta_b}{\delta_a} \\ \phi(0, \xi) &= \phi_{2b}(\xi) & \text{for } -\frac{\delta_b}{\delta_a} < \xi \leq 0 \\ \phi(0, \xi) &= \phi_{2a}(\xi) & \text{for } 0 \leq \xi < 1 \\ \phi(0, \xi) &= 1 & \text{for } 1 \leq \xi < \infty \end{aligned} \quad (7)$$

and for the upper and lower boundary conditions

$$\phi(\xi, \xi) \rightarrow \phi_b \text{ for } \xi \rightarrow -\infty$$

$$\phi(\xi, \xi) \rightarrow 1 \text{ for } \xi \rightarrow \infty$$

The functions  $\phi_{2a}(\xi)$  and  $\phi_{2b}(\xi)$  are the initial boundary layer profiles of the jet and external flows, respectively, and are represented in our case by the power-law velocity profiles

$$\phi_{2a}(\zeta) = \zeta^{1/n} \quad \text{and} \quad \phi_{2b}(\zeta) = \phi_b \left( -\frac{\delta_a}{\delta_b} \zeta \right)^{1/n}$$

The solution of Equation (6) subject to the boundary conditions of Equations (7) is

$$\begin{aligned} \phi(n, n_p) &= \frac{1}{2} \left[ (1 + \phi_b) + \operatorname{erf} \left( n - n_p \right) - \phi_b \operatorname{erf} \left( n + \frac{\delta_b}{\delta_a} n_p \right) \right] \\ &+ \frac{1}{\sqrt{\pi}} \int_{n-n_p}^n \phi_{2a} \left( \frac{n-\beta}{n_p} \right) e^{-\beta^2} d\beta + \frac{1}{\sqrt{\pi}} \int_n^{n + \frac{\delta_b}{\delta_a} n_p} \phi_{2b} \left( \frac{n-\beta}{n_p} \right) e^{-\beta^2} d\beta \quad (8) \end{aligned}$$

$$\left. \begin{aligned} \text{where} \quad n_p &= \frac{1}{2\sqrt{\xi}} + \frac{\sigma \delta_a}{x} \\ n &= \zeta n_p \rightarrow \sigma \frac{y}{x} \end{aligned} \right\} \text{for large values of } x$$

and the error function has the usual definition

$$\operatorname{erf} n = \frac{2}{\sqrt{\pi}} \int_0^n e^{-\beta^2} d\beta$$

The velocity profile is thus represented by a family of curves in  $n$  with one parameter,  $n_p$ . The first three terms, within the brackets, represent the contribution to the velocity profile of the fully-developed flow. These terms predominate at small  $n_p$  (far downstream). The last two terms, containing the integrals, represent the contributions of the lower and

upper initial boundary layers, respectively. These terms are most important at large  $\eta_p$  (near the nozzle exit), and become negligible far downstream. The relationship between the terms is shown for an intermediate value of  $\eta_p$  in Figure 14. A quick approximate method for obtaining the integrals is presented in Appendix A.

This family of velocity profiles was interpreted by Chapman, Korst, and subsequent investigators to hold in an orthogonal "intrinsic" coordinate system, not usually coincident with the physical coordinate system, as a result of the approximations inherent in the development of the equation of motion. This system of coordinates, designated  $(x, y)$  in Figure 13, page 56, is related to the physical coordinates by the relationships

$$x \approx X$$

$$y = Y + y_m(x),$$

where  $y_m(0) = 0$ , and  $y_m(x)$  may be determined with the aid of integral relations for the conservation of mass and momentum in the following forms:

$$\rho_b u_b (-\delta_b - Y_{R_b}) + \int_{-\delta_b}^0 \rho u \, dy + \int_0^{\delta_a} \rho u \, dy + \rho_a u_a (Y_{R_a} - \delta_a)$$

$$+ \int_0^x \rho_b v_b \, dx = \int_{Y_{R_b}}^{Y_{R_a}} \rho u \, dy + y_m (\rho_a u_a - \rho_b u_b)$$

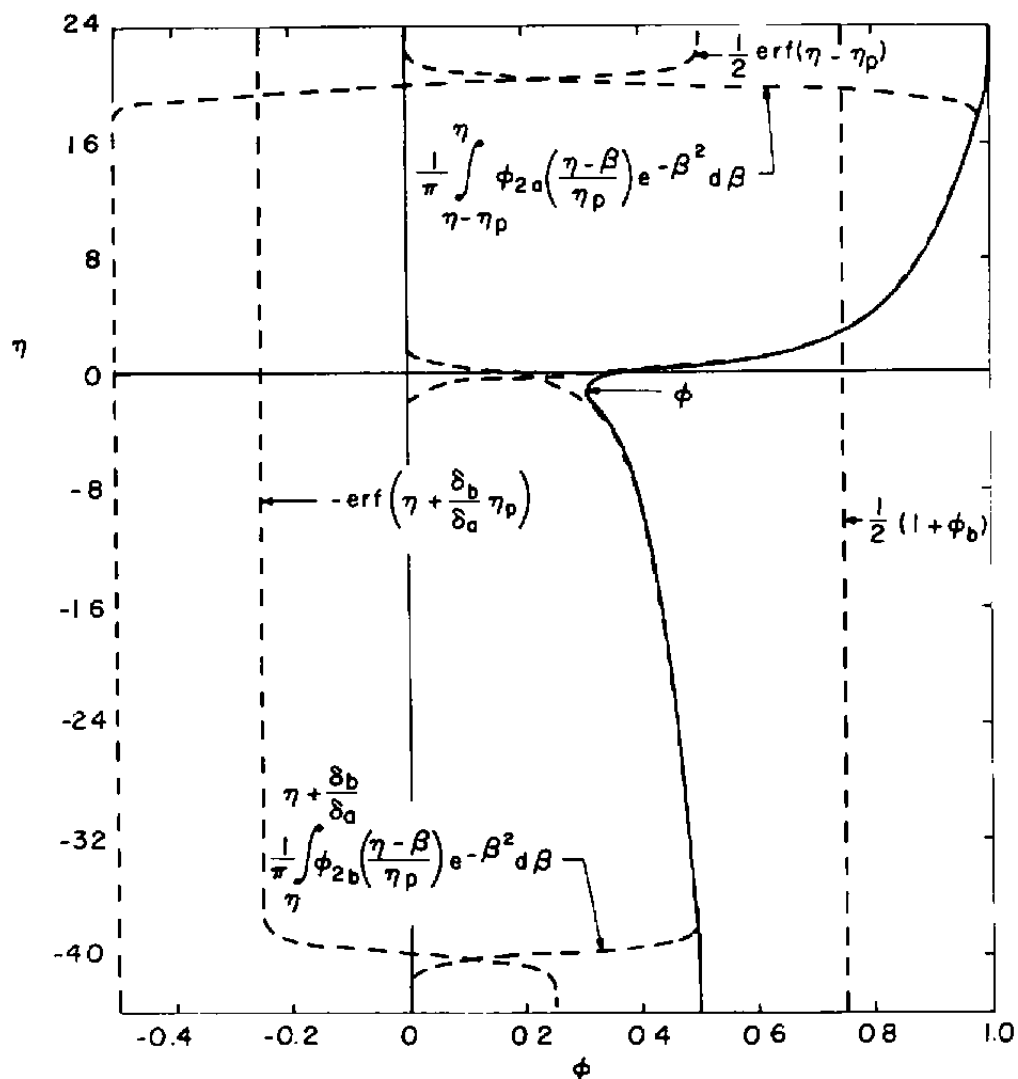


Figure 14. Component velocity function for a flow not yet fully developed.

and

$$\rho_b u_b^2 (-Y_{Rb} - \delta_b) + \int_{-\delta_b}^0 \rho u^2 dy + \int_0^{\delta_a} \rho u^2 dy + \rho_a u_a^2 (Y_{Ra} - \delta_a)$$

$$+ u_b \int_0^x \rho_b v_b dx = \int_{Y_{Rb}}^{Y_{Ra}} \rho u^2 dy + \eta_m (\rho_a u_a^2 - \rho_b u_b^2)$$

Multiplying the first equation by  $u_b$  and subtracting from the second gives

$$\eta_m = \eta_{Ra} - \frac{1}{1-\phi_b} \left[ (1-C_a^2) \left( \int_{\eta_{Rb}}^{\eta_{Ra}} \frac{\phi^2}{\Lambda-C_a^2\phi^2} d\eta - \phi_b \int_{\eta_{Rb}}^{\eta_{Ra}} \frac{\phi}{\Lambda-C_a^2\phi^2} d\eta \right) \right. \\ \left. + \eta_p \left( \frac{\theta_b}{\delta_a} \frac{\rho_b}{\rho_a} \phi_b^2 + \frac{\theta_a}{\delta_b} + \frac{\delta_a^*(1-\phi_b)}{\delta_a} \right) \right]$$

where Crocco's energy relationship for the stagnation temperature profile has been assumed, i.e.

$$\Lambda = \frac{T_o}{T_{o_a}} = \frac{T_{o_b}}{T_{o_a}} \frac{1-\phi}{1-\phi_b} + \frac{\phi - \phi_b}{1 - \phi_b} ,$$

and the momentum and displacement thicknesses of the flow are known. Using the auxiliary integrals, the equation for  $\eta_m$  may be rewritten:

$$\eta_m = \eta_{Ra} - \frac{1}{1-\phi_b} \left[ I_2(n_{Ra}) - \phi_b I_1(n_{Ra}) \right. \\ \left. + \eta_p \left( \frac{\theta_b}{\delta_a} \frac{\rho_b}{\rho_a} \phi_b^2 + \frac{\theta_a}{\delta_a} + \frac{\delta_a^*(1-\phi_b)}{\delta_a} \right) \right] \quad (9)$$

An expression for the location of the dividing streamline (DSL), which defines the boundary across which no net mass transfer occurs, may be developed by considering the mass flow below the DSL:

$$\int_0^{\delta_a} \rho u dy + \rho_a u_a (Y_{Ra} - \delta_a) = \int_{Y_j}^{Y_{Ra} + \eta_m} \rho u dy$$

After some manipulation, similar to that used to derive the  $\eta_m$  relationship, the following expression involving  $\eta_j$  may be written:

$$I_1(\eta_j) = \frac{1}{1-\phi_b} \left[ I_1(n_{Ra}) - I_2(n_{Ra}) \right. \\ \left. - \eta_p \left( \frac{\rho_b}{\rho_a} \phi_b^2 \frac{\theta_b}{\delta_a} + \frac{\theta_a}{\delta_a} \right) \right] \quad (10)$$

Leaving Equations (9) and (10) for the moment, it is possible, in order to obtain an expression for an effective displacement thickness,  $\delta_e^*$ , due to plume entrainment, to consider mass conservation above the dividing streamline:

$$\rho_b u_b (-\delta_b - Y_{Rb}) + \int_{-\delta_b}^0 \rho u dy = \int_{Y_{Rb} + y_m}^{Y_j} \rho u dy - \int_0^x \rho_b v_b dx$$

If  $v_b$  is assumed constant, the above expression can be rewritten as

$$\phi_b' \times \frac{\eta_p}{\delta_a} = I_1(\eta_j) \left( \frac{\frac{T_{ob}}{T_{oa}} - C_a^2 \phi_b^2}{1 - C_a^2} \right) - \phi_b \eta_m + \phi_b \frac{\eta_p}{\delta_a} \delta_b^* \quad (11)$$

where  $\phi_b' = \frac{v_b}{u_a}$ .

If a correction to the plume shape, that is to say, a displacement thickness due solely to the entrained mass,

$\int_0^x \rho_b v_b dx$ , is defined as

$$- \frac{\delta_e^*}{x} = \frac{v_b}{u_b} = \frac{\phi_b'}{\phi_b} ,$$

then Equation (11) becomes

$$\delta_e^* = - \frac{\delta_a}{\eta_p} \left[ \frac{I_1(\eta_j) \left( \frac{T_{ob}}{T_{oa}} - C_a^2 - \phi_b^2 \right)}{(1 - C_a^2) \phi_b} - \eta_m \right] - \delta_b^* \quad (12)$$

Equation (12) is an explicit expression for the displacement thickness due to plume entrainment, and as such is applied to the plume boundary at each viscous/inviscid iteration. Equations (9) and (10) are explicit equations for

$\eta_m$  and  $I_1(n_j)$ , which are required in Equation (12). The magnitude of  $\delta_e^*$  may be expected to be that of the plume adjustment which would result if the inviscid/inviscid loop were used. A listing of the computer program used in the solution of these equations is presented as Appendix B. A description of this program and a discussion of the required input are presented in the next sub-chapter.

#### Digital Computer Program

A short digital computer program, DELPL, has been generated for the purpose of solving the equations developed in the previous sub-chapter. The program is used as an integral portion of the Combined Viscous/Inviscid Program, supplying values of the displacement thickness due to plume entrainment at longitudinal locations along the plume as specified by the calling subroutines. This adjustment of the plume shape is performed at each iteration according to the relationship below:

$$\text{New } YP^n = YP^n + \delta_e^*$$

where the value of  $YP$  on the right-hand side is the value calculated by the viscous portion of the CVI Program with the plume assumed a solid body. Correspondingly, the displacement thickness may be written as

$$\text{New } \delta_p^* = \delta_p^* + \delta_e^*.$$

$\delta_e^*$  is calculated using Equation (12),  $I_1(n_j)$  is computed directly from Equation (10), and Equation (9) is used

for  $\eta_m$ . Notice that it is not necessary to determine  $\eta_j$ , as only the value of the integral  $I_1(\eta_j)$  is needed. The two auxiliary integrals,  $I_1(\eta_{R_a})$  and  $I_2(\eta_{R_a})$ , are calculated using a 96-point Gaussian integration formulation (55). This quadrature has proven to be of very good accuracy, being comparable to a trapezoidal integration of one-thousand points, as determined by check calculations.

Computation of the integrals in the velocity equation is performed using a closed-form approximation described in Appendix A. This approximation provides a decrease in calculation time (CPU) on the order of five, with little or no difference from these integrals when they were evaluated using the 96-point Gaussian integration.

Parameters input to DELPL by the calling subroutine are shown in Table VI. A listing of the program is given as Appendix B. The calculation of  $\delta_e^*$  in DELPL is rapid in spite of the numerical integrations, each calculation of  $\delta_e^*$  requiring about one second of CPU time.

#### Stagnation Temperature Distribution Near the Nozzle/Afterbody

It was assumed, in the development of the equations, that the turbulent Prandtl number,  $Pr_t$ , was everywhere equal to unity. Accordingly, the variation of stagnation temperature throughout the mixing flow field was assumed to be linear with respect to the local velocity, following the relationship developed by Crocco (56), which is valid for turbulent flow with unity turbulent Prandtl number. In particular, the

TABLE VI

INPUT FOR THE PLUME DISPLACEMENT THICKNESS SUB-  
PROGRAM (DELPL), AS PROVIDED BY THE CALLING SUBROUTINE

Parameter Name(s)	Explanation	Typical Value(s)
XP	Axial locations along plume	X = 76.209, 78.163,...(in.)
FB	Velocity ratio of the two streams ( $\phi_b$ )	0.6
TTA	Stagnation temperature of the reference stream	575.0°R
TTB	Stagnation temperature of the secondary stream	575.0°R
CPA	Gas constant, $C_p$ , of the reference stream	6006.0
UA	Velocity of the reference stream	1175.0 ft/sec
DSTRA	Displacement thickness of reference stream	0.0125 ft
DSTRB	Displacement thickness of secondary stream	0.0250 ft
EN	Velocity profile power exponent	7
N	Number of points to be calculated (100 maximum)	10
IWR	Output control parameter	1
DSTRE	Values to the plume displacement thickness returned from DELPL	DSTRE = 0, -0.008, -0.017,... (in.)

relationship chosen by Korst and Chow (51) was

$$\Lambda = \frac{T_o}{T_{o_a}} = \frac{T_{o_b}}{T_{o_a}} \frac{1 - \phi}{1 - \phi_b} + \frac{\phi - \phi_b}{1 - \phi_b} \quad (13)$$

which provided the linear variation with appropriate values of the two free-stream stagnation temperatures at large lateral distances from the dividing streamline. This linear relationship, while valid in the flow far downstream, becomes inappropriate near the nozzle/afterbody, where the stagnation temperature characteristics are more those of boundary layer flows than free mixing. That is to say, one would expect the stagnation temperature distribution to retain its boundary layer characteristics for some distance downstream, gradually changing to the Crocco linear form as the flow becomes more and more fully developed. The difference is shown qualitatively in Figure 15, where the sketch of the stagnation temperature distributions of the boundary layer flows over an adiabatic wall is taken from Shapiro (57). The stagnation temperature distributions are characteristic in that they show an "overshoot" near the boundary layer edge, and that they attain the adiabatic wall temperatures at the wall, which are not necessarily the values obtained from Equation (13) at  $\phi = 0$ . These phenomena were analyzed by van Driest (58), who assumed a variation in the turbulent Prandtl number across the boundary layer, subdividing the boundary layer into three regions. A concise summary of a number of analytical studies devoted to this problem is provided by Whitfield (33).

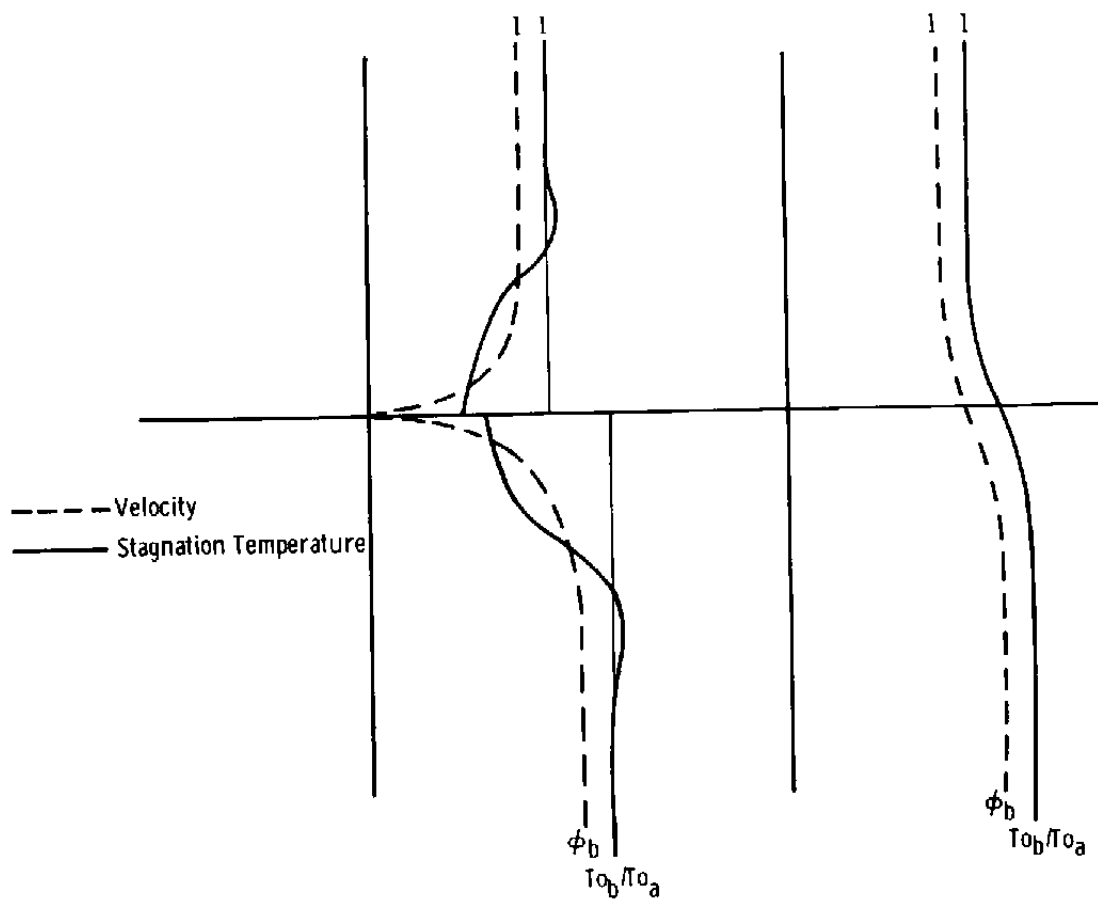


Figure 15. Qualitative examples of the stagnation temperature and velocity distribution for boundary layer and fully-developed flow.

The inadequacy of the Crocco relationship became apparent during the initial calculations of the mixing program, DELPL. Far downstream, the results of the numerical solutions of the integrals involved in the calculations and, indeed, the effective displacement thickness,  $\delta_e^*$ , agreed well with the computations of Korst and Chow (51) for fully developed flow. Close to the beginning of the mixing region, however, there was a small but persistent discrepancy in the value of these quantities. All possible sources of error, such as truncation errors in the integration schemes, were eliminated as sources, and the sole remaining source was the stagnation temperature ratio,  $\Lambda$ , which appears in the integrals  $I_1(\eta_{Ra})$  and  $I_2(\eta_{Ra})$ . In order to demonstrate this, it is first necessary to calculate the values of  $I_1(\eta_{Ra})$ ,  $I_2(\eta_{Ra})$ ,  $I_1(\eta_j)$ ,  $\eta_m$ , and  $\delta_e^*$  that were expected at the nozzle/afterbody junction, that is, at  $\eta_p \rightarrow \infty$ .

Beginning with the definition of  $I_1(\eta_{Ra})$ , i.e.

$$I_1(\eta_{Ra}) = \frac{\eta_{Rb} (1 - C_a^2) \phi_b}{\frac{T_{Ob}}{T_{Oa}} - C_a^2 \phi_b^2} + \int_{\eta_{Rb}}^{\eta_{Ra}} \frac{(1 - C_a^2) \phi}{\Lambda - C_a^2 \phi^2} d\eta \quad (14)$$

it was recognized that at the nozzle/afterbody junction,  $\eta_p \rightarrow \infty$ , the velocity profiles of the two as yet unmixed flows would be essentially the initial boundary layer distributions. The lower flow from the nozzle would consist of a power law distribution from  $\eta = 0$  to  $\eta = \eta_p$ , and the remaining flow, from  $\eta_p$  to  $\eta_{Ra}$ , would be at a constant velocity,  $\phi = 1$ .

Similarly, the upper (external) flow would be a power law velocity distribution from  $\eta = 0$  to  $\eta = -\frac{\delta_b}{\delta_a} \eta_p$ , and the remaining flow to  $\eta = \eta_{Ra}$  would be at a constant velocity,  $\phi = \phi_b$ . Dividing the integral in Equation (14) into the four appropriate integrals gives

$$\lim_{\eta_p \rightarrow \infty} I_1(\eta_{Ra}) = \frac{\eta_{Ra} (1 - C_a^2) \phi_b}{\frac{T_{Ob}}{T_{Oa}} - C_a^2 \phi_b^2} + \int_{\eta_{Ra}}^{-\frac{\delta_b}{\delta_a} \eta_p} \frac{(1 - C_a^2) \phi_b}{\frac{T_{Ob}}{T_{Oa}} - C_a^2 \phi_b^2} d\eta + \int_0^0 \frac{(1 - C_a^2) \phi_{2b}}{1 - C_a^2 \phi_{2b}^2} d\eta + \int_0^{\eta_p} \frac{(1 - C_a^2) \phi_{2a}}{1 - C_a^2 \phi_{2a}^2} d\eta + \int_{\eta_p}^{\eta_{Ra}} d\eta, \quad (15)$$

Using the relationship

$$\frac{T}{T_a} = \frac{\rho_a}{\rho} = \frac{1 - C_a^2 \phi^2}{1 - C_a^2}$$

which results from the expression for constant enthalpy and the isobaric assumption. Equation (15) may be written, after integrating the first and fourth integrals directly, as

$$\lim_{\eta_p \rightarrow \infty} I_1(\eta_{Ra}) = -\frac{\rho_b}{\rho_a} \phi_b \frac{\delta_b}{\delta_a} \eta_p + \int_{-\frac{\delta_b}{\delta_a} \eta_p}^0 \frac{\rho u}{\rho_a u_a} d\eta + \int_0^{\eta_p} \frac{\rho u}{\rho_a u_a} d\eta + \eta_{Ra} - \eta_p, \quad (16)$$

where the definitions of  $\phi_{2a}$  and  $\phi_{2b}$  have replaced them in the remaining integrals. For  $\eta_p \rightarrow \infty$ , the variable of integration,  $\eta$ , becomes the physical coordinate,  $Y$ , under the relationship

$$\eta = \frac{\eta_p}{\delta_a} Y,$$

and if the integrals and their limits are modified accordingly, Equation (16) becomes

$$\lim_{\eta_p \rightarrow \infty} I_1(\eta_{Ra}) = \eta_{Ra} - \eta_p \left( \frac{\delta_a^*}{\delta_a} + \frac{\rho_b}{\rho_a} \phi_b \frac{\delta_b^*}{\delta_a} \right) \quad (17)$$

where the definitions of  $\delta_a^*$  and  $\delta_b^*$  were used to eliminate the integrals in Equation (16).

A similar procedure for the second auxiliary integral,  $I_2(\eta_{Ra})$ , gives

$$\begin{aligned} \lim_{\eta_p \rightarrow \infty} I_2(\eta_{Ra}) &= \eta_{Ra} - \eta_p \left( \frac{\delta_a^*}{\delta_a} + \frac{\theta_a}{\delta_a} \right) \\ &\quad - \eta_p \frac{\rho_b}{\rho_a} \phi_b^2 \left( \frac{\delta_b^*}{\delta_a} + \frac{\theta_b}{\delta_a} \right) \end{aligned} \quad (18)$$

Thus, for  $\eta_p \rightarrow \infty$ , both  $I_1(\eta_{Ra})$  and  $I_2(\eta_{Ra})$  may be evaluated directly, since all of the quantities on the right-hand side of Equations (17) and (18) are known.

Substitution of Equations (17) and (18) into the previously derived expression (Equation (9), page 64) for the displacement of the intrinsic coordinate system,  $\eta_m$ , gives

$$\lim_{n_p \rightarrow \infty} n_m = 0 \quad (19)$$

This identity is physically satisfactory, as the intrinsic coordinate system is not displaced at the beginning of the mixing region. Similar direct substitution of Equations (17), (18), and (19) into the expressions for the integral  $I_1(n_j)$ , Equation (10), page 64, and  $\delta_e^*$ , Equation (12), page 65, yields

$$\lim_{n_p \rightarrow \infty} I_1(n_j) = - n_p \frac{\rho_b}{\rho_a} \phi_b \frac{\delta_b^*}{\delta_a} \quad (20)$$

$$\lim_{n_p \rightarrow \infty} \delta_e^* = 0 \quad (21)$$

Equation (21) indicates that at the beginning of the mixing region there is, as yet, no correction to the external boundary layer displacement thickness,  $\delta_e^*$ , due to entrainment.

The cases analyzed herein are all of the "cold flow" type, that is, the exhaust is provided by pressurized air in a reservoir at essentially ambient temperature rather than by a combustion process. Thus, for our cases,  $T_{ob} = T_{oa}$  may be assumed to a close degree of approximation, and the Crocco relationship reduces to  $\Lambda = 1$  for all  $\phi$ . This simplified stagnation temperature distribution along with a qualitative representation of the actual boundary layer temperature distributions are shown in Figure 16. A linear approximation to the actual stagnation temperature distribution used for computation purposes is shown as a dashed line. The parameter C

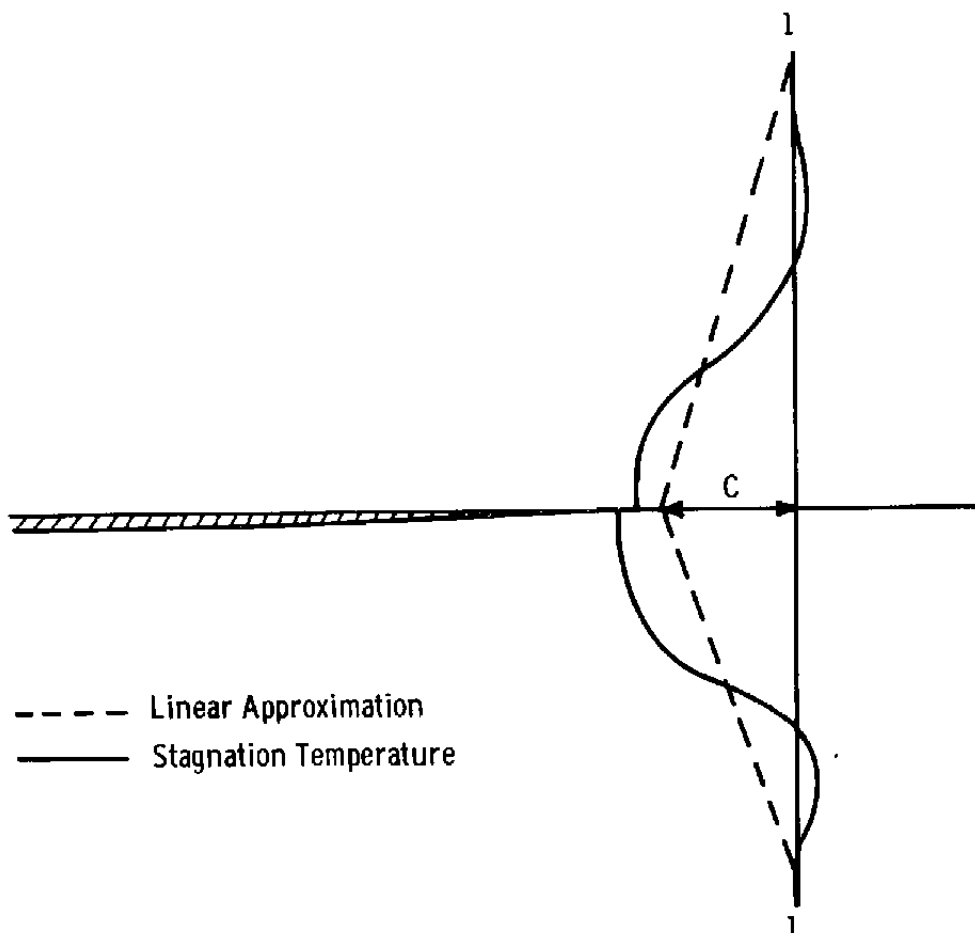


Figure 16. Stagnation temperature distribution for  $T_{ob} = T_{oa}$ .

is a constant evaluated by iteration at the initial station, that is, at the nozzle/afterbody junction, according to the modified relationship

$$\lim_{\eta_p \rightarrow \infty} I_1(\eta_{Ra}) = \frac{(1-c_a^2) \phi_b}{\frac{T_{ob}}{T_{oa}} - c_a^2 \phi_b^2} + \int_{\eta_{Rb}}^{\eta_{Ra}} \frac{(1-c_a^2) \phi}{(\Lambda - f_c c) - c_a^2 \phi^2} d\eta$$

$$= \eta_{Ra} - \eta_p \left( \frac{\delta_a^*}{\delta_a} + \frac{\rho_b}{\rho_a} \phi_b \frac{\delta_b^*}{\delta_a} \right)$$

where, for our cases,  $T_{ob}/T_{oa} = \Lambda = 1$  and  $f_c = 1$  at  $\eta_p \rightarrow \infty$ . Thus, the integral  $I_1(\eta_{Ra})$  is evaluated exactly numerically at the initial X-location, which is usually set at a high value of  $\eta_p$ , approximately  $10^4$ . In order to evaluate  $f_c$ , it is assumed that the mechanism that produces the change in the stagnation temperature distribution is the difference in actual velocity profile from that of the error function distribution in the fully developed case. The necessary function,  $f_c$ , may be written

$$f_c = \frac{\frac{\phi_{act} - \phi_{erf}}{\phi_{act}}}{\frac{\phi_{act_o} - \phi_{erf_o}}{\phi_{erf_o}}}$$

where  $\phi \equiv \int_{\eta_L}^{\eta_U} \phi d\eta$ , and the subscript "act" denotes the

integral of the actual velocity distribution at a given station, the subscript "erf" denotes the integral of the fully developed velocity distribution at that station, and the subscript "o" denotes those integrals evaluated at the initial station. Thus,  $f$  varies from unity at the initial station to zero far downstream, where  $\Phi_{act} = \Phi_{erf}$ . The integration limits  $\eta_L$  and  $\eta_U$  are found by determining the values of  $\eta$  where the velocities are equal to 0.9999 of their free-stream values.

This modification to the  $\Lambda$  function is satisfactory in obtaining the desired results, that is, the effective plume displacement thickness,  $\delta_e^*$ , at the initial station becomes essentially zero. A two-constant approach was also tried, in which not only  $I_1(\eta_{Ra})$  but also  $I_2(\eta_{Ra})$  were matched with their limiting values, but the slight change in results did not justify the added complication.

#### The Mixing Parameter, $\sigma$

One of the most critical parameters in use in this analysis is the mixing parameter,  $\sigma$ , also known as the spreading, spread rate, or similarity parameter. Introduced in the expression for the turbulent viscosity,  $\varepsilon_\infty$  (see page 58), the mixing parameter is essentially a measure of the rate of spreading of the exhaust jet, with high values of  $\sigma$  indicating a low spreading rate. Görtler's (53) original analysis assumed that the velocity profiles downstream were simply functions of  $(y/x)$ , hence the designation "similarity

parameter." Analyzing the case of two-dimensional mixing of a single stream and a quiescent atmosphere, he determined the incompressible value of  $\sigma$  to be 13.5, based on the data of Reichardt (59). Further investigations of the incompressible single stream case by Leipmann and Laufer (60) based on their data indicated that a value of  $\sigma = 11$  best suited the data, while in comparison with their data using Tollmien's theory (61), they chose  $\sigma = 12$ . Using Tollmien's data, Cordes (62) determined  $\sigma$  to be 11.95. Generally, a value of  $\sigma = 12$  is accepted as the "round-number" value for the incompressible one-stream case. Other investigations have shown that  $\sigma$  increases with increasing Mach number, with the relationship developed by Korst and Chow (51) being accepted as in reasonable agreement with available data, i.e.

$$\sigma = 12 + 2.758 M. \quad (22a)$$

More recent efforts in determining the values of  $\sigma$  for the base flow problem using a variety of turbulence models have been summarized by Greenwood (63) in his doctoral thesis. Since the emphasis in his summary is the effect of compressibility at Mach numbers up to eight on the single-stream configuration, the results have limited applicability to the present study.

For the two-stream mixing case, that is, where both streams have non-zero velocities, Weinstein's experiments (64) showed that  $\sigma$  varied greatly with the initial velocity ratio of the two streams. The most commonly accepted measure of this effect is approximated by a relationship developed by Korst and Chow (51), i.e.

$$\sigma_{II} = \frac{1 + \phi_b}{1 - \phi_b} \sigma_I \quad (22b)$$

In choosing acceptable models of  $\sigma$  for use in the mixing portion of the CVI Program, this author was influenced by the pragmatic viewpoint of Gauthier in his justification for the choice of turbulence models for his numerical boundary layer program, PETULA:

Mais il ne faut pas perdre de vue que nous poursuivons un travail d'ingénieur, c'est-à-dire que notre objectif n'est pas de contribuer à une amélioration de nos connaissances théoriques sur la turbulence, mais de fournir une méthode pratique de calcul qui soit un compromis raisonnable entre précision et coût. (65)

(However, it is necessary not to lose sight that we are pursuing the work of an engineer, that is to say, our objective is not to contribute to the improvement of our theoretical knowledge of turbulence, but to furnish a practical method of calculation that is a reasonable compromise between precision and cost - author's translation.)

It was decided to use commonly accepted values of  $\sigma$  in the viscous/inviscid iterations in order to determine their validity in the cases analyzed. Accordingly, each configuration was run at least three times in the CVI Program using the following values of  $\sigma$ :

- (a) One-stream  $\sigma$  from Equation (22a),  $\sigma_I$ ,
- (b) Two-stream  $\sigma$  from Equation (22b),  $\sigma_{II}$ ,
- (c) At least one value of  $\sigma$  empirically chosen from the results of (a) and (b).

Both of the values of  $\sigma$  in (a) and (b) are further modified for the effect of the initial boundary layer by means of the relationship

$$\frac{\sigma}{\sigma_\infty} = \left[ \frac{x/(\delta_a + \delta_b)}{37} \right]^{1/7}$$

which was the result of a curve-fit of data from Chapman and Korst (66), Figure 17. The choice of  $\sigma$  in the third case, (c), was based on the results of (a) and (b) and, as such, indicated the magnitude of the deficiencies in the values of  $\sigma$  predicted under the multitude of assumptions and simplifications previously described. The choices for (c) will be described for each configuration as appropriate.

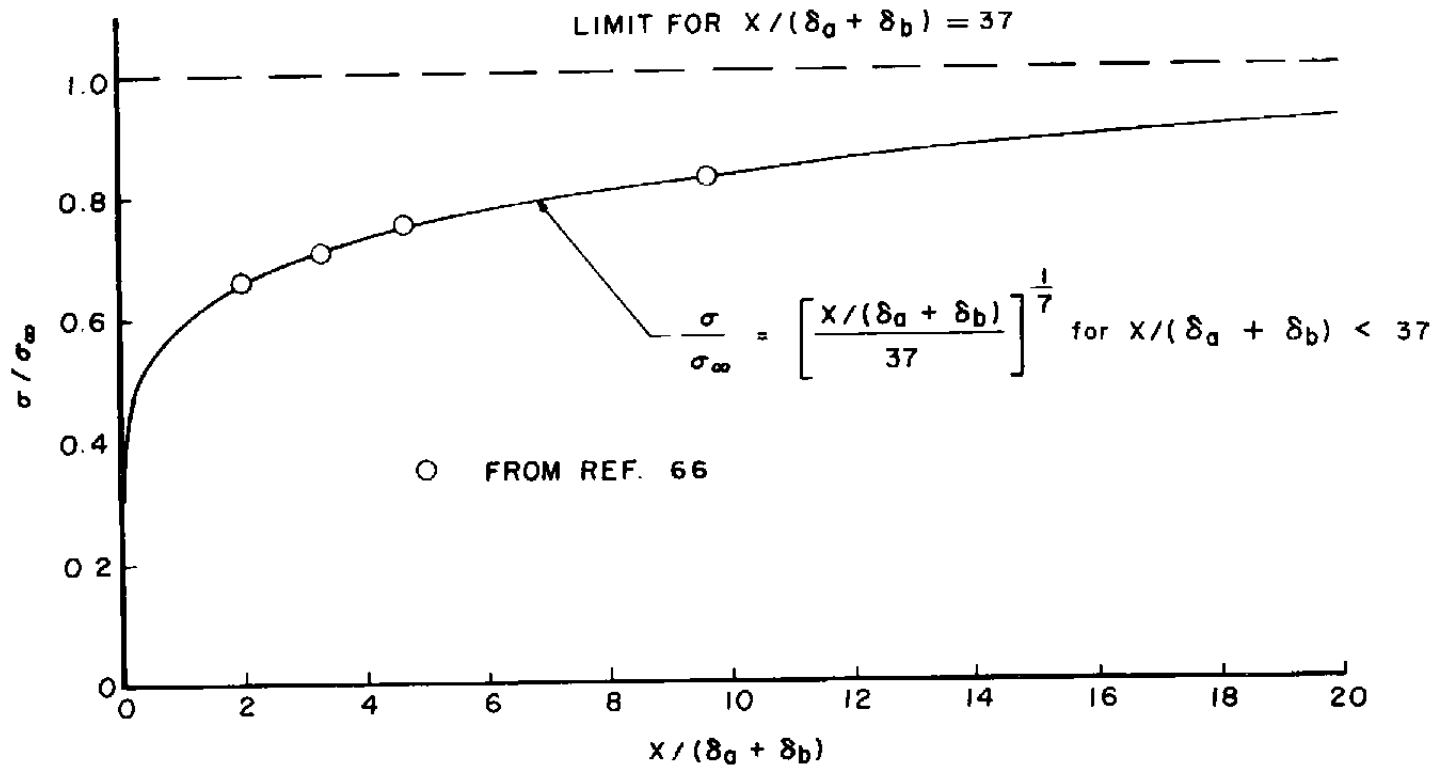


Figure 17. Variation of mixing parameter,  $\sigma$ , with downstream distance.

## CHAPTER IV

## ANALYTICAL RESULTS IN COMPARISON TO EXPERIMENT

Introductory Remarks

There have been, over the course of the years, numerous wind tunnel tests of a variety of isolated axisymmetric body shapes, both with solid stings and real plumes, in transonic flows. Many of the configurations would be directly applicable for comparison with the flow predictions of the CVI Program. Reference to the recent AGARD efforts toward improved nozzle testing techniques (67) and the extensive bibliography presented by the U. S. Army Missile Command (68), to cite just two, will indicate the level of such efforts in recent years.

The choice of configurations to be analyzed in this chapter was strongly influenced by the works presented at the Propulsion Interactions Workshop at Langley Research Center in May 1976 (16) and recent work at the Arnold Engineering Development Center. It was felt that such configurations truly represented current areas of interest in the field, and furthermore, that future efforts would probably be directed toward similar configurations for some time to come. This necessary narrowing of the field left, unfortunately, a great number of works untouched, but the analyses presented may be considered representative and pertinent.

Solid Sting Cases

Equivalent body. One of the earliest uses of the CVI Program was in the analysis of a body of revolution whose cross-sectional area distribution was designed to be representative of that of a typical twin jet fighter aircraft, that is to say, an "equivalent body." The wind tunnel tests were carried out in the 16-foot Transonic Wind Tunnel at the Arnold Engineering Development Center (69), and the model was equipped with interchangeable contoured, cylindrical, and 15-degree boattails. Only the contoured boattail was analyzed, as prime interest at that time was centered about the capability of the CVI Program to predict pressures along the entire length of an axisymmetric body, and it was felt that the analysis of one boattail configuration would be sufficient to demonstrate this capability.

As Figure 18 shows, the equivalent body has a somewhat exotic geometry, particularly in the areas around Sta. 20, Sta. 90, and along the boattail. These areas first presented some problems for the inviscid portion of the CVI Program as the body-normal coordinates tended to intersect at great distances from the body, but these problems were remedied by moving the beginning point of the sheared coordinate system ahead of this area. Also to be noted is the step of 1.268 inches at the end of the contoured boattail (Sta. 130.053). Appealing to the "wake-body" concept, in which an effective body shape is sought in order to represent the

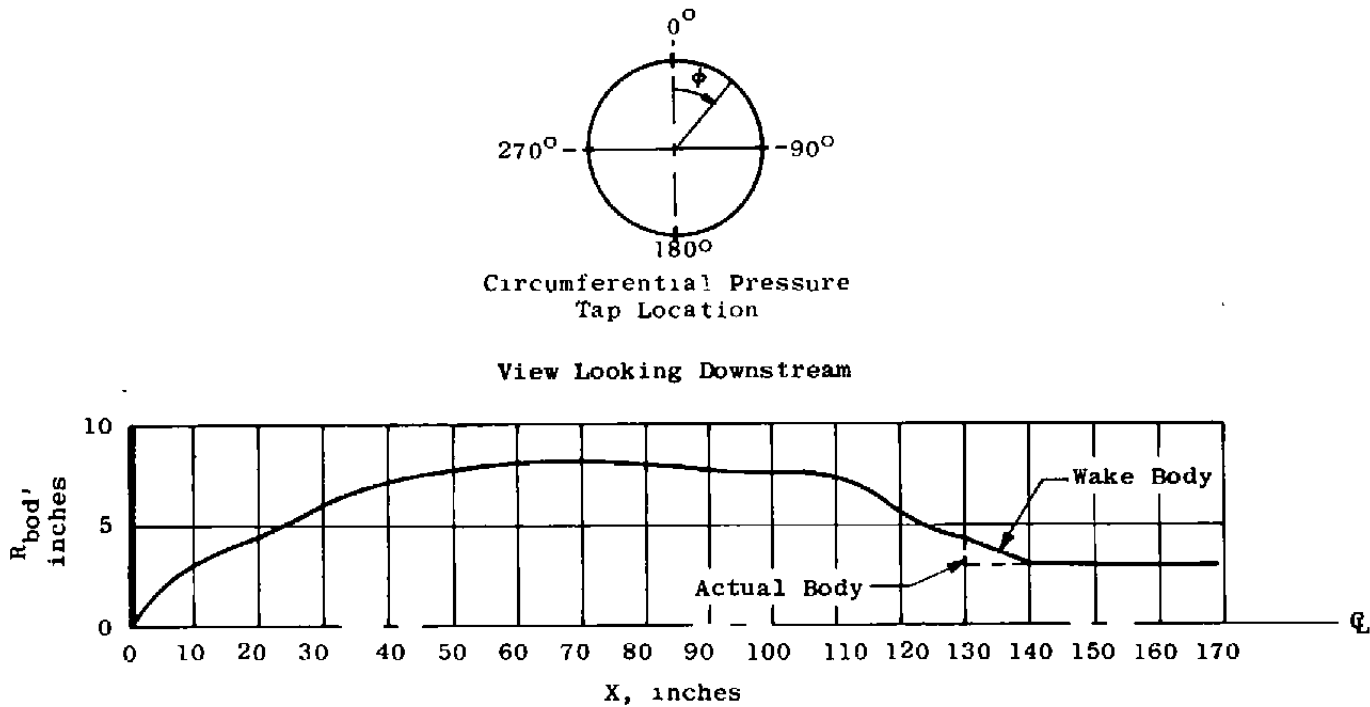
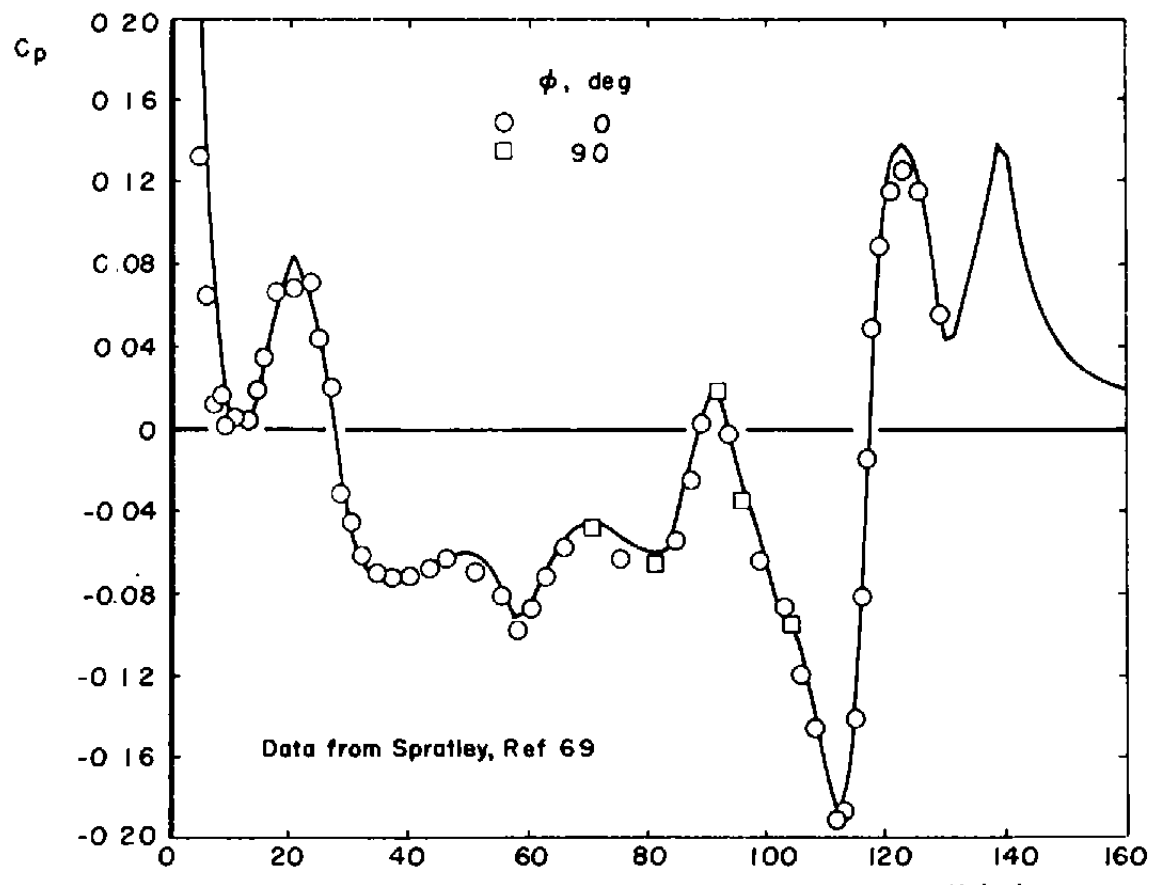


Figure 18. Equivalent body shape and circumferential pressure tap locations.

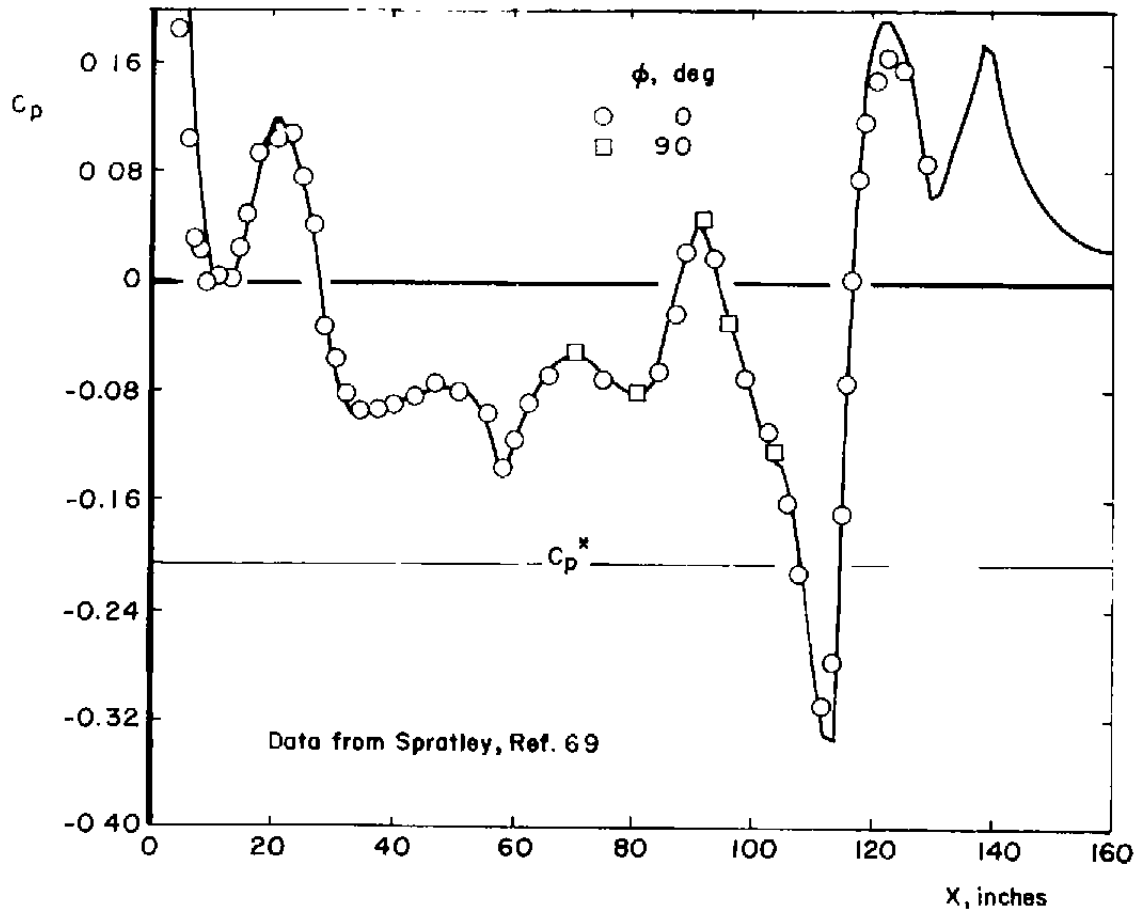
separated region after the step, it was decided to modify this area by means of a conical surface from the end of the boattail to the sting. The angle of the conical surface to the horizontal axis was chosen to be 7.5 degrees, based on extrapolation of the Mach number dependent analytic results of Mueller (70) and the transonic results of Wu, et al. (71) and Chen (72). It was found by the investigators in the last two references that this angle is a weak function of the Mach and Reynolds numbers in transonic flow. This angle was used for all Mach numbers analyzed and was, in fact, little more than a realistic estimate, but the effect on the flow over the equivalent body as a whole was anticipated to be negligible.

The equivalent body was analyzed at three Mach numbers: 0.598, 0.892, and 1.196. The nominal unit Reynolds number for all three cases was  $2.5 \times 10^6 \text{ ft}^{-1}$ . The results are presented in Figures 19a-c. In the two subsonic cases, Figures 19a and b, the agreement between the predicted and experimental values of pressure coefficient are extremely good. All of the variations in pressure due to the concave body geometry are accounted for. The CVI Program predicts too high of a pressure along the boattail, in the area of Sta. 123, but considering the rough estimate of cone angle used in the wake-body approximation, agreement is still very good. In the supersonic case, Figure 19c, it is apparent that the nose region is not well predicted, and this error results in deviations from the measured pressures up to Sta.



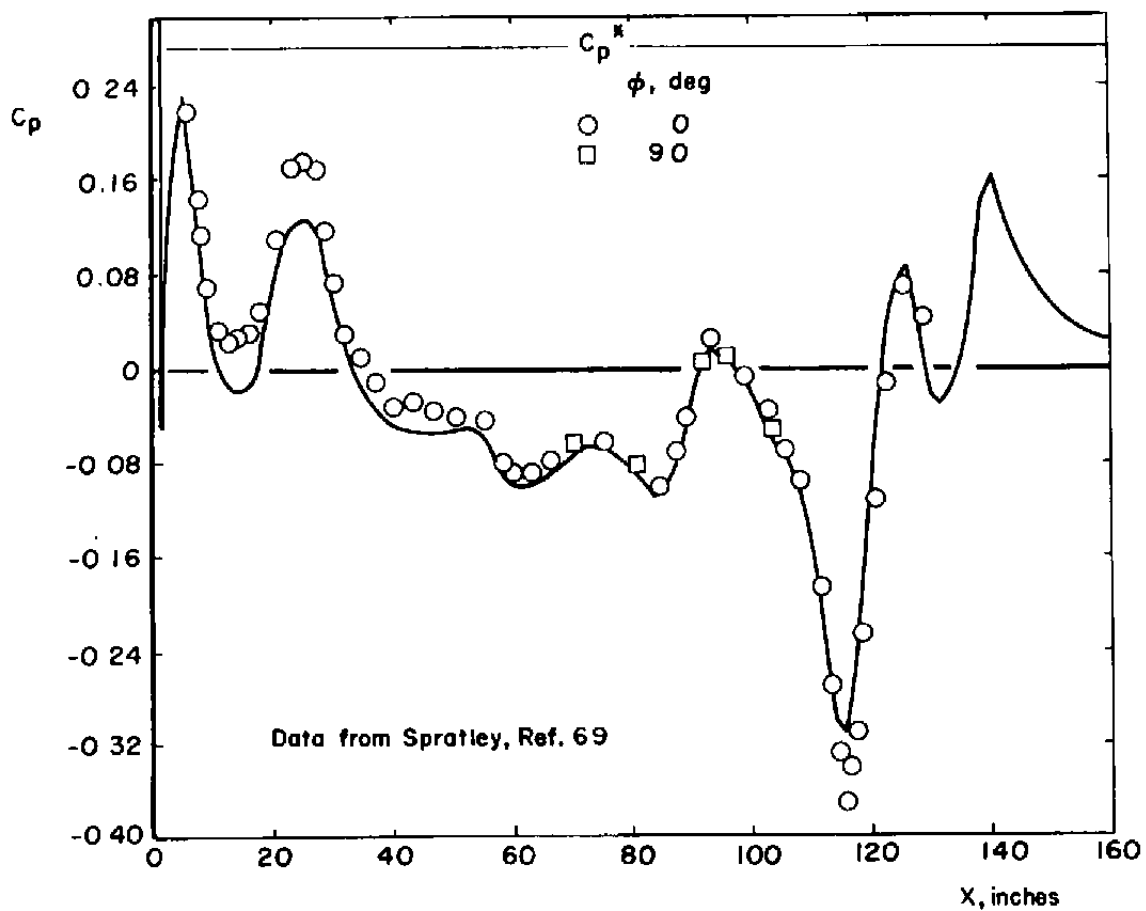
a. Mach Number = 0.598

Figure 19. Longitudinal pressure coefficient distribution for the equivalent body.



b. Mach Number = 0.892

Figure 19. (Continued)



c. Mach Number = 1.196

Figure 19. (Continued)

60. This problem can sometimes be eliminated by changing the grid spacing in that area. Farther downstream the agreement is good, and the CVI Program predicts the compression pressure fairly well, lending credence to the wake-body concept for small steps in supersonic flow.

NASA Langley circular arc boattail. Efforts at NASA Langley Research Center in recent years have centered around the effect of jet exhausts on boattail pressure drag. Pressure and drag measurements on three circular arc boattails of different lengths but with identical closure ratios of 0.50 were carried out by Reubush and Runckel (73). Published at the same time were the results of Reubush (74) on different boattail length models with closure ratios of 0.6 and 0.7. Basic conclusions regarding the effects of boattail length and closure ( $d_{ex}/d_m$ ) were stated in these reports, but any definite correlations were obviated by the very strong effects of Mach number and flow separation on the pressure distribution over the boattail.

The emphasis at NASA Langley were then directed toward determining the applicability of solid plume simulators for afterbody wind tunnel tests. These simulators, in actuality cylindrical stings, would have the advantage of providing the support for the model, thus relieving any necessity of a large and disruptive strut, and would also eliminate the need of extensive internal plumbing required by the jet exhaust models at a great reduction in cost. The

results of the experimental investigations were published by Reubush (75), and a much fuller treatment was later presented also by Reubush (38). It is from this last document that data were obtained which were used for comparison with the CVI Program predictions at various Mach numbers.

The wind tunnel tests in Reference (38) were performed in the Langley 16-foot transonic tunnel, which has a Mach number range, in continuous operation, from 0.20 to 1.30. It is important to note that this wind tunnel is atmospheric, thus each Mach number differs slightly in Reynolds number (Reynolds number effect will be compared later with data from Reference (17)). These small changes in Reynolds number were accounted for in the CVI Program by adjusting the input parameters in the viscous portion of the program accordingly.

The model was strut supported, and the plume simulator was eleven inches in length, giving a length-to-model maximum diameter ratio of 1.83. The model support installation is shown in Figure 20. Eight circular arc boattails, varying in afterbody length and closure ratio, were tested. Of the eight boattails available, the one with a fineness ratio ( $\lambda/d_m$ ) of 1.768 and a closure ratio ( $d_{ex}/d_m$ ) of 0.50 was chosen for analysis. A sketch of this boattail is shown in Figure 21. This particular configuration was chosen because its fineness ratio permitted the flow to be attached at most Mach numbers, and yet its low closure ratio allowed

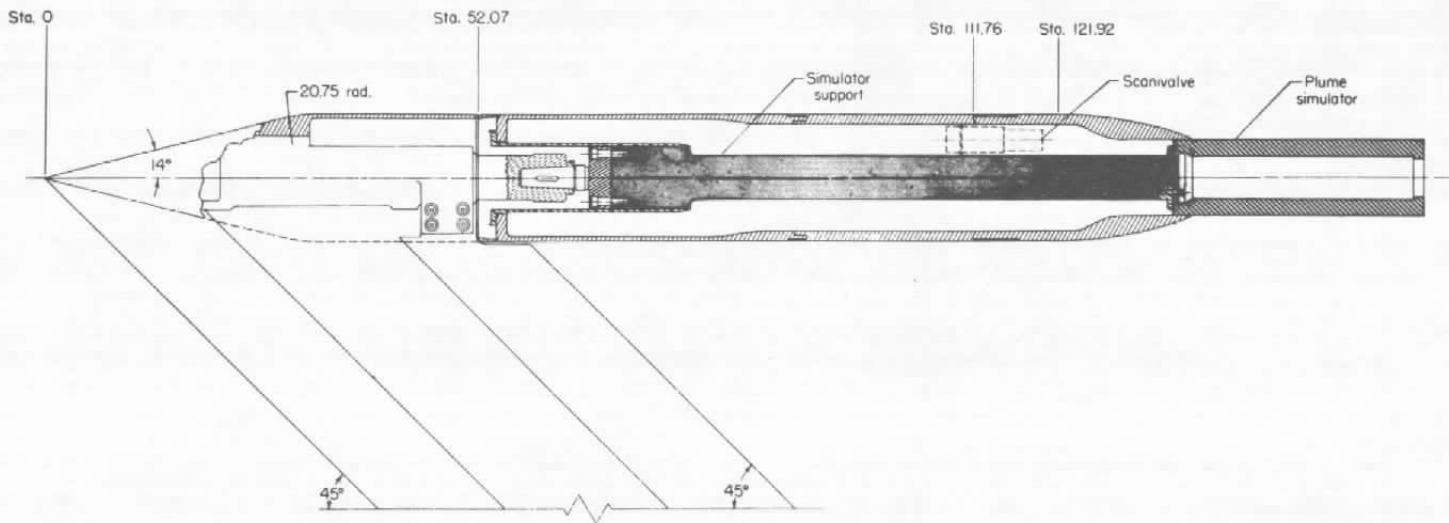
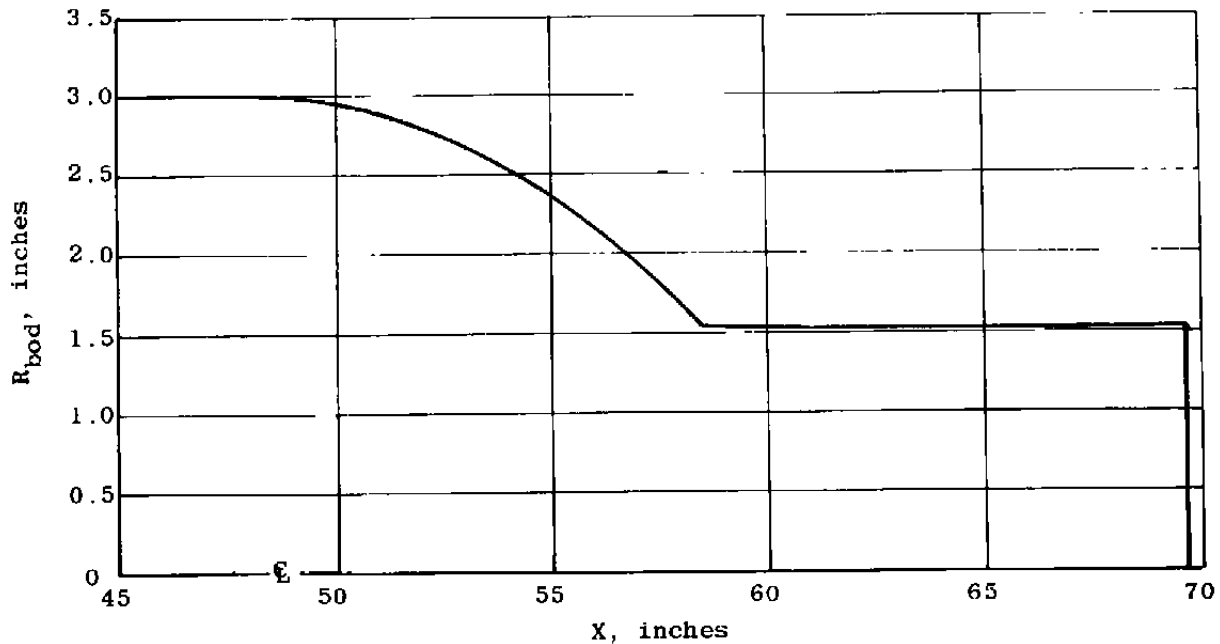


Figure 20. Sketch of the NASA Langley  $l/d = 1.768$  circular arc boattail model showing internal sting arrangement for support of simulators.



$$X \leq 48$$

$$R_{bod} = 3$$

$$48 < X < 58.608 \text{ inches}$$

$$R_{bod} = -36 + \sqrt{-x^2 + 96x - 783}$$

$$58.608 \leq X \leq 69.608$$

$$R_{bod} = 1.53$$

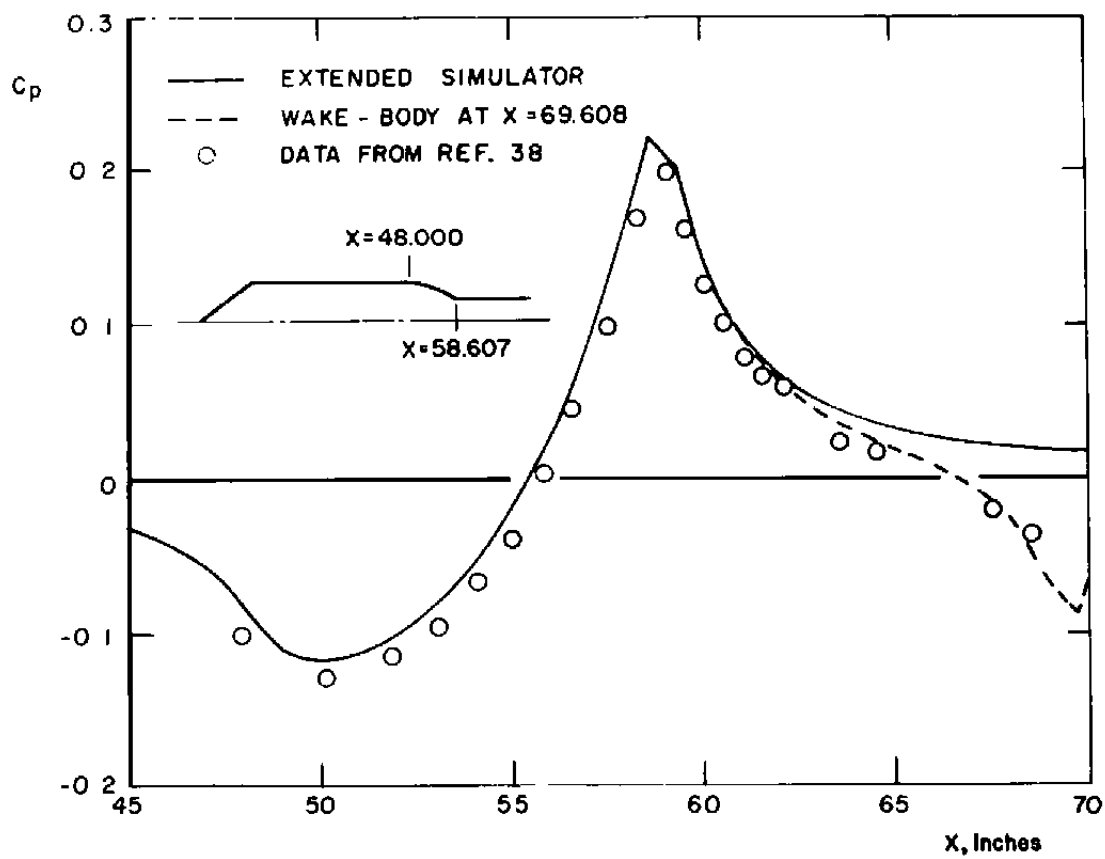
Note: All dimensions in inches in the above equations.

Figure 21. Shape of the NASA Langley  $l/d_m = 1.768$  circular arc boattail and cylindrical plume simulator.

ample opportunity for axisymmetric effects to be present.

Results of the CVI Program predictions for Mach numbers ranging from 0.4 to 1.3 are presented in Figures 22a-g. Because the Langley 16-foot wind tunnel is atmospheric, the unit Reynolds number varied with Mach number from a value of  $2.40 \times 10^6 \text{ ft}^{-1}$  at  $M_\infty = 0.4$  to  $4.22 \times 10^6 \text{ ft}^{-1}$  at  $M_\infty = 1.3$ . Flow predictions are presented only for the boattail/sting areas of the model, as the data were only available for this portion of the model. The CVI Program, however, utilized the full model and sting in both its viscous and inviscid portions during the course of the iterations.

In general, the predictions agree well with the data. Some general statements may be made concerning the characteristics of the converged iterative solutions. Firstly, in the subsonic cases, the expansion of the flow over the shoulder of the boattail, from Sta. 45 to approximately Sta. 55, is underestimated slightly. As the Mach number is increased, however, this tendency becomes less, and the shoulder predictions are very good at the higher subsonic Mach numbers. Secondly, at the afterbody/sting junction, the CVI Program generally overpredicts the peak compression pressure, although data were not available at the exact point of the junction, so it is difficult to estimate exactly the magnitude of the error. The prediction of a higher peak pressure at this location may indicate a small separated area there, as its magnitude increases as Mach number is increased.



a.  $M_\infty = 0.4$

Figure 22. Longitudinal pressure coefficient distribution for the NASA Langley  $l/d = 1.768$  circular arc boattail in the Langley 16-ft transonic Wind tunnel.

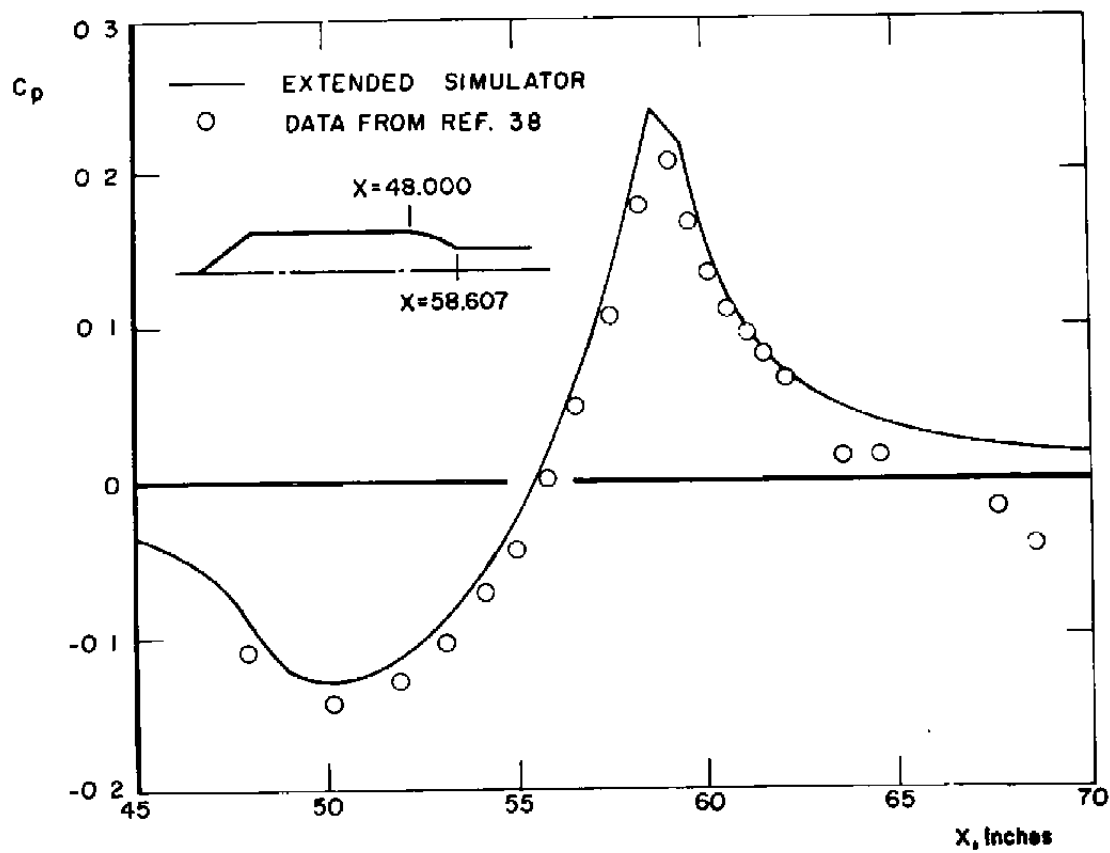
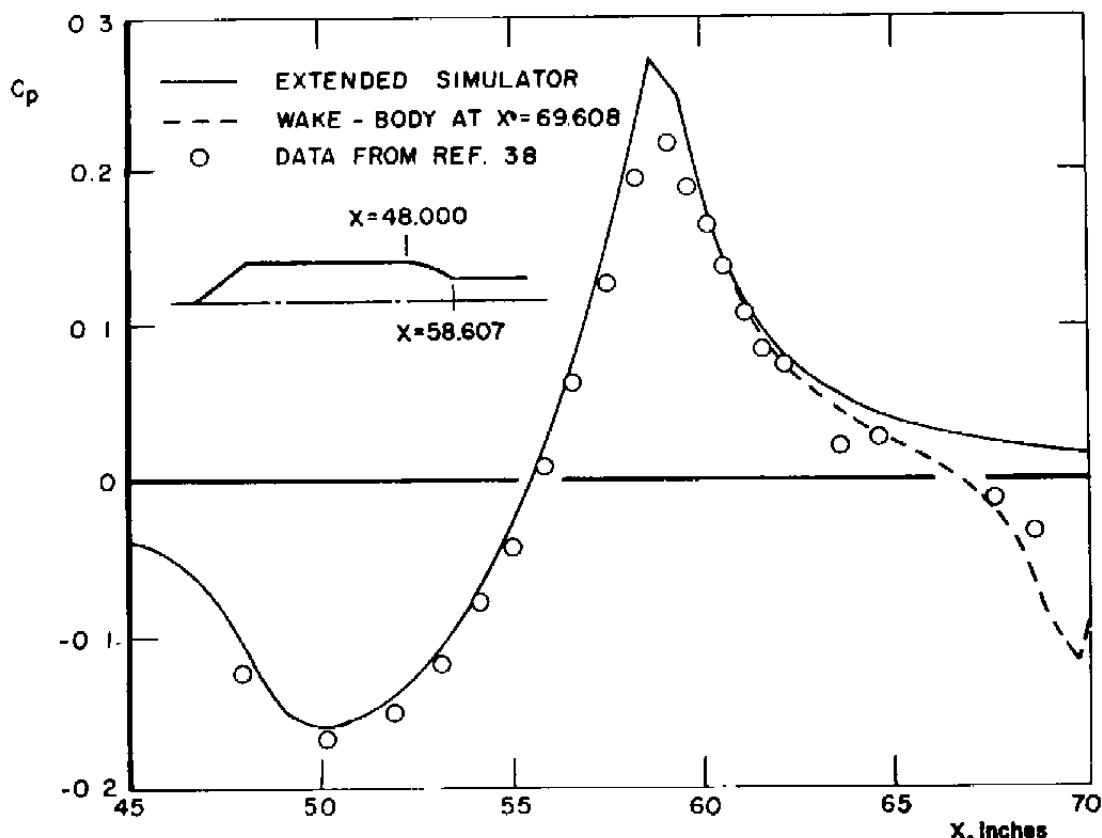
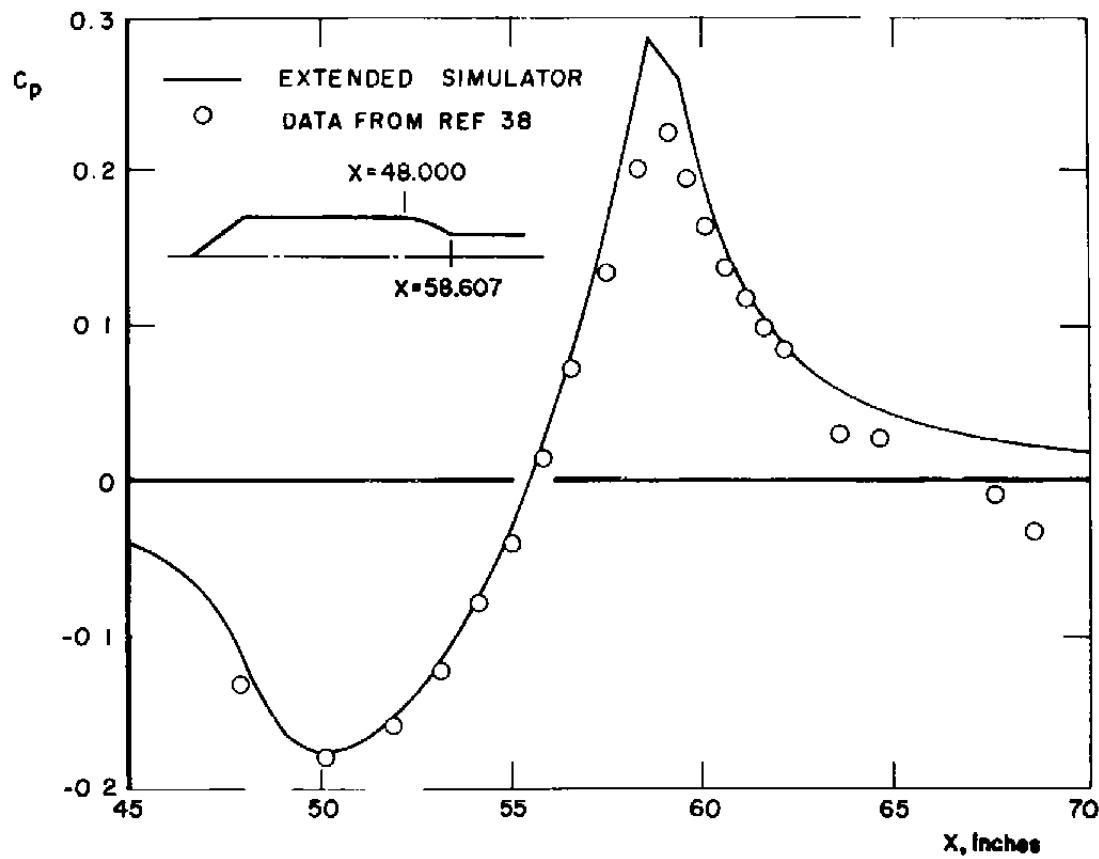


Figure 22. (Continued)

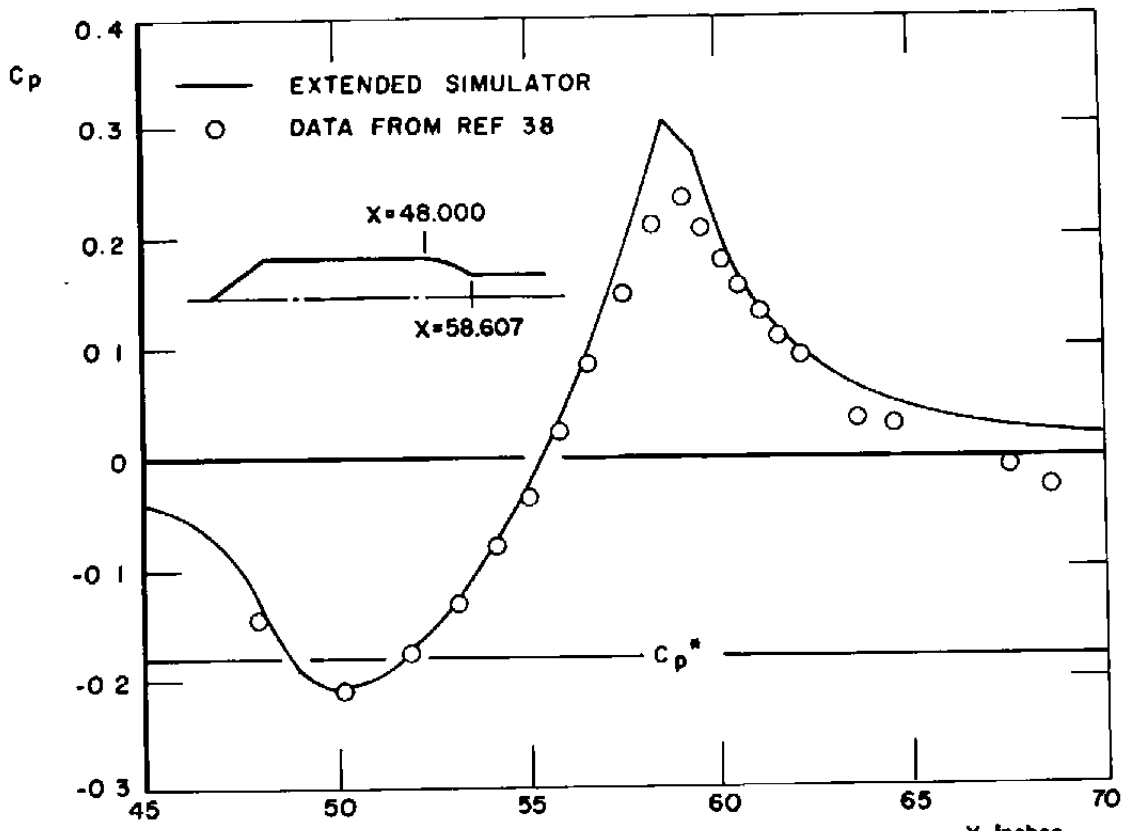


c.  $M_\infty = 0.8$   
Figure 22. (Continued)



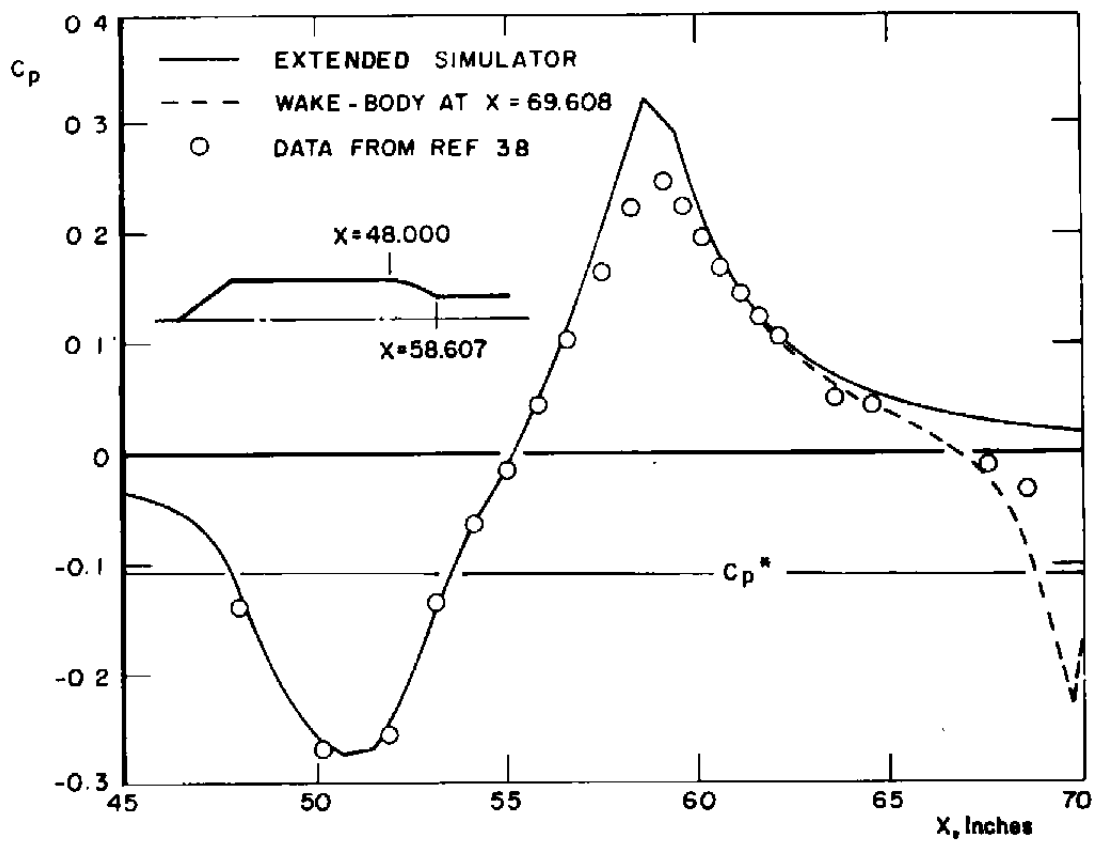
$$d, M_\infty = 0.85$$

Figure 22. (Continued)



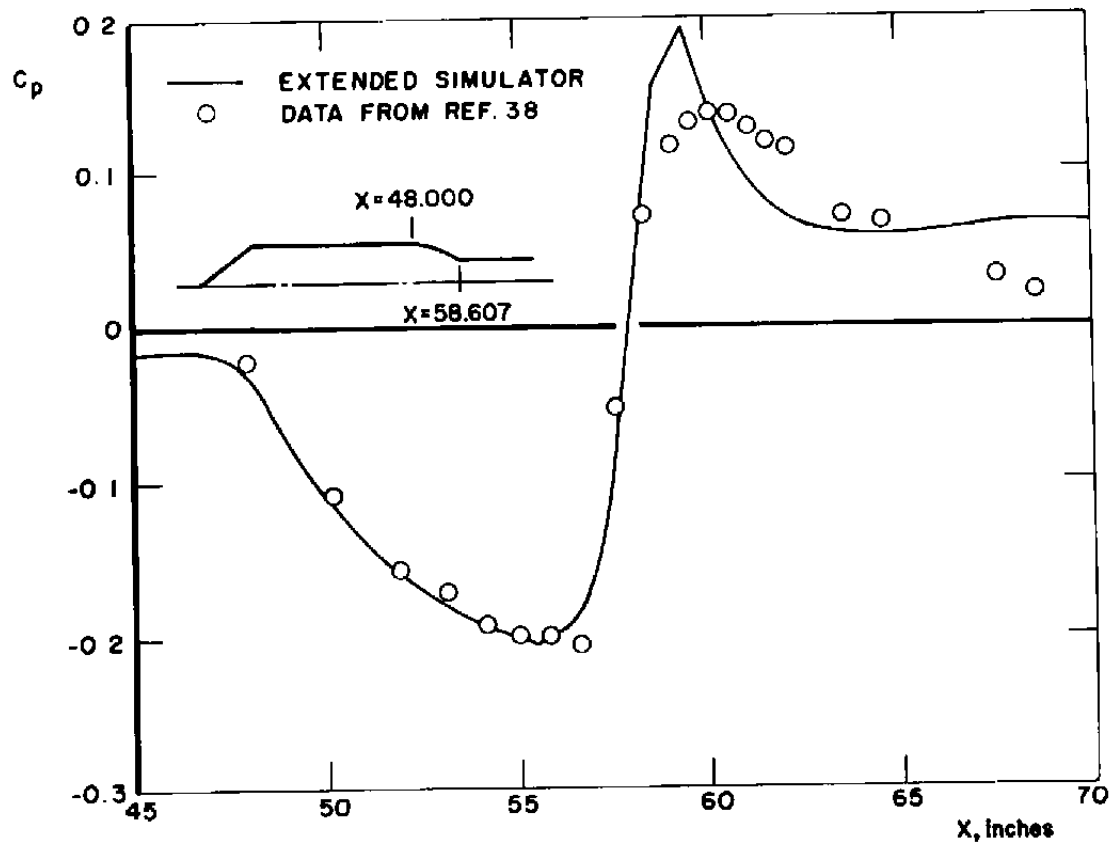
e.  $M_\infty = 0.9$

Figure 22. (Continued)



f.  $M_\infty = 0.94$

Figure 22. (Continued)



g.  $M_\infty = 1.3$

Figure 22. (Continued)

It should be noted that for Mach numbers greater than 0.90 the shoulder area is supersonic, and the rapid compression downstream of this area, but upstream of the boattail/sting junction, suggests the formation of a weak shock wave.

In the supersonic case, Figure 22g, the steep gradient of the compression indicates the presence of a strong shock wave. The CVI Program predicts the expansion over the shoulder quite well, differing in shape as it does from the expansions in the subsonic cases. After the shock wave, however, the prediction is less satisfactory. The tendency of the data to assume a slightly curved plateau aft of the boattail/sting junction indicates an area of flow separation much larger than that found in the subsonic cases. This, of course, moves the flow out of the realm of applicability of the CVI Program. Addition of a transonic separation criterion, such as found in Reference (14), could be valuable in this and similar cases.

It was mentioned before that the length of the cylindrical plume simulator was eleven inches. The effect of this short sting is reflected in Figures 22 by the continued decrease of the last four data points to pressures even lower than free-stream, a result of the flow separation and expansion at the end of the sting. The wake-body model was applied in a manner similar to its application with the equivalent body, that is to say, a 7.5-deg cone was assumed at the end of the cylindrical plume cylinder, and the improvement in the predictions is shown as dashed lines for Mach numbers

of 0.4, 0.8, and 0.94.

As a point of interest, Figure 23 shows the results of the CVI Program when the boundary layer was calculated as two-dimensional for a Mach number of 0.8. Although this prediction is about as good in the shoulder region, when the displacement thickness is small, as the case with the axisymmetric boundary layer (Figure 22c, page 96), it suffers at and downstream of the boattail/sting junction. Clearly, the axisymmetric boundary is necessary when adverse pressure gradients and changing body geometry demand a rapid increase in boundary layer displacement thickness.

To measure the effect of Reynolds number changes on the pressure distribution over this boattail, data from more recent work by Reubush and Putnam (17) were utilized. The data were taken at three azimuths about the body, but differences were small. The wind tunnel used for these tests was the NASA Langley 1/3-meter cryogenic tunnel, the test section of which is essentially a smaller version of the NASA Langley 16-foot wind tunnel. By varying tunnel stagnation pressure and stagnation temperature, Reynolds numbers (based on the length of the model from the nose to the beginning of the boattail) from  $5 \times 10^6$  to over  $50 \times 10^6$  are obtainable. Six models were tested, and the model chosen for analysis was the same  $l/d_m = 1.768$  circular arc boattail chosen previously in this section. It was, of course, much smaller, being one-sixth the size of the model used in the NASA Langley 16-foot tunnel. The model had a cylindrical plume simulator, but

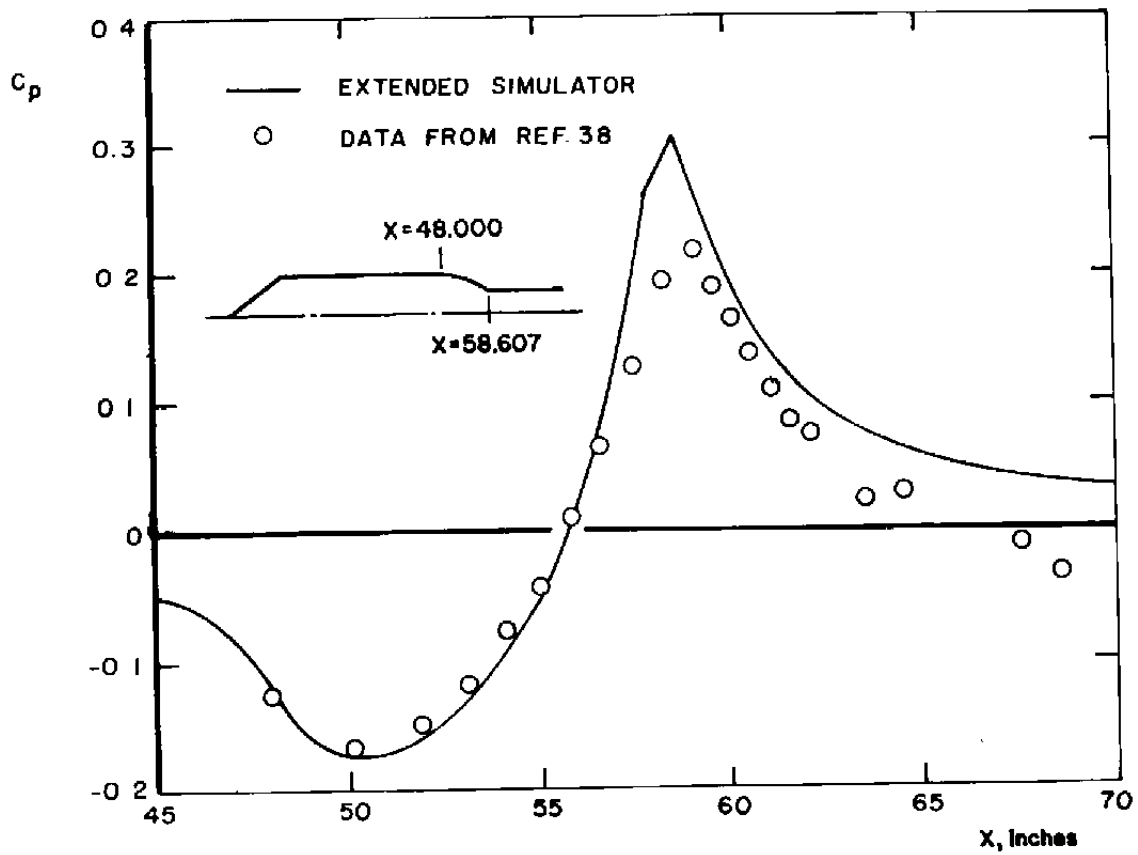
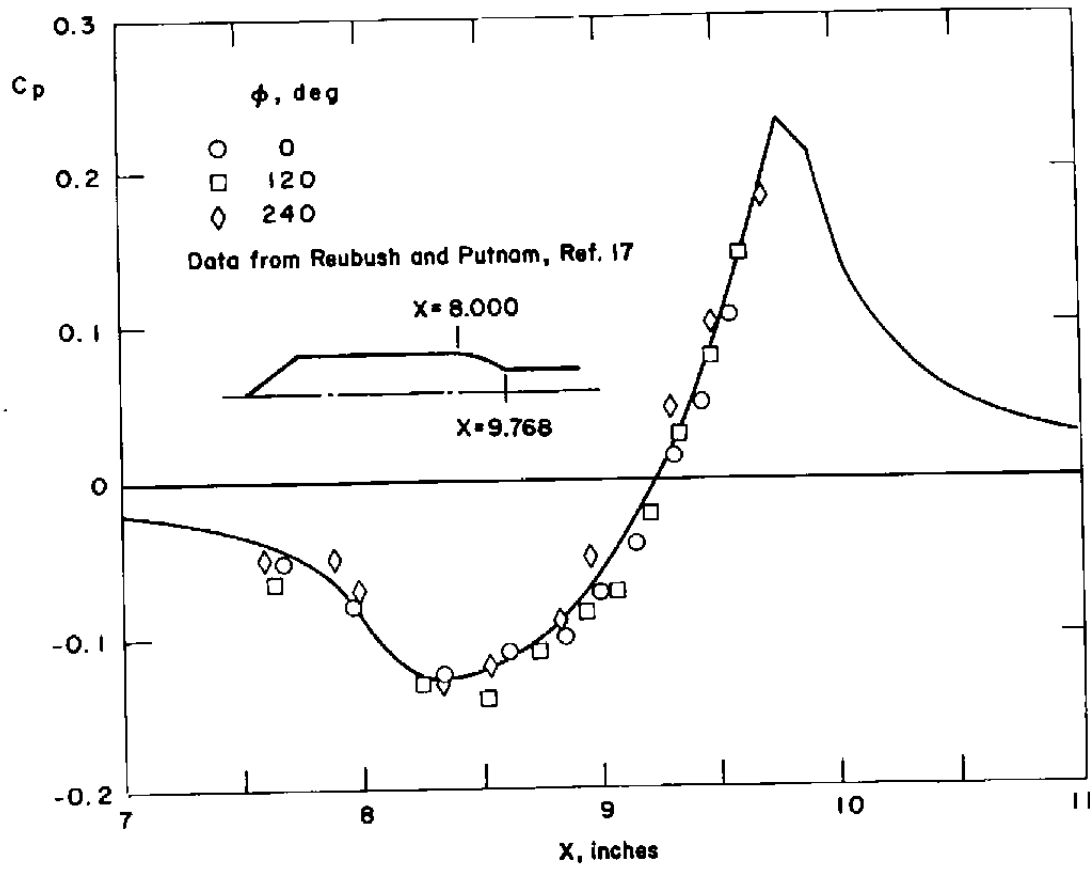


Figure 23. Longitudinal pressure coefficient distribution for the NASA Langley  $l/d_m = 1.768$  circular arc boattail using a two-dimensional boundary layer in the CVI program.

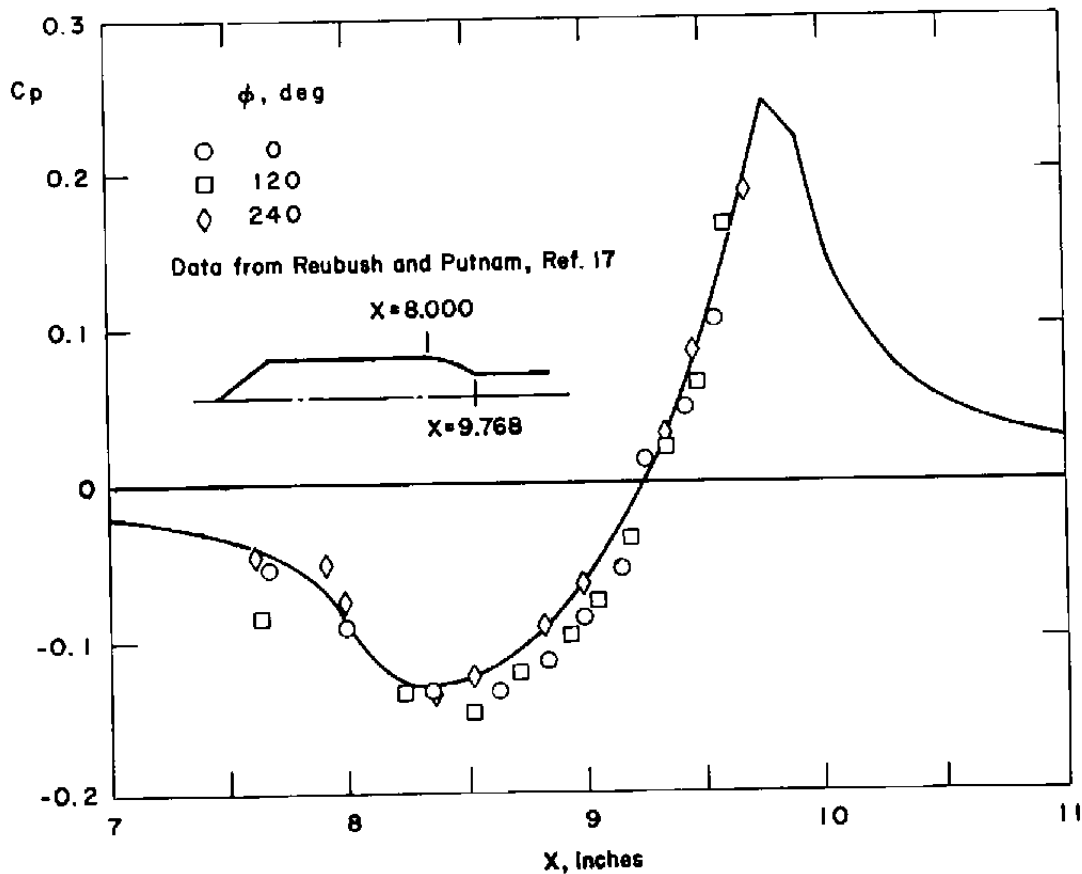
it was not instrumented, and hence no sting data are available. The results of the CVI Program in comparison with the data are shown in Figures 24a-f for three Reynolds numbers at both of two Mach numbers, 0.6 and 0.9. Although there is some scatter of the data, particularly in the area of the expansion over the boattail shoulder, the CVI Program predictions agree well with the data. For both Mach numbers, the effect of increasing Reynolds number is to decrease the pressure at the shoulder expansion and to increase the compression at the boattail/sting junction. This is a result of the decrease of boundary layer displacement thickness as Reynolds number is increased. The effective body shape for a high Reynolds number will be closer to the actual body shape, and thus the pressure distribution will tend to resemble the body-alone inviscid solution more so than a low Reynolds number case. Both the data and the CVI Program predictions exhibit this characteristic, but the effect, even with a change in Reynolds number of almost a magnitude, is very small. The one exception is the expansion pressure in Figure 24e, which appears to be slightly too low. This may be due to a slight difference in test Mach number (about 1% higher) for this case versus the higher Reynolds case, Figure 24f.

CBA Boattail. The CVI Program was also applied to a boattail configuration with a cylindrical sting similarly analyzed by Chow, Bober, and Anderson (9), and this configuration is denoted by the acronym "CBA Boattail." The



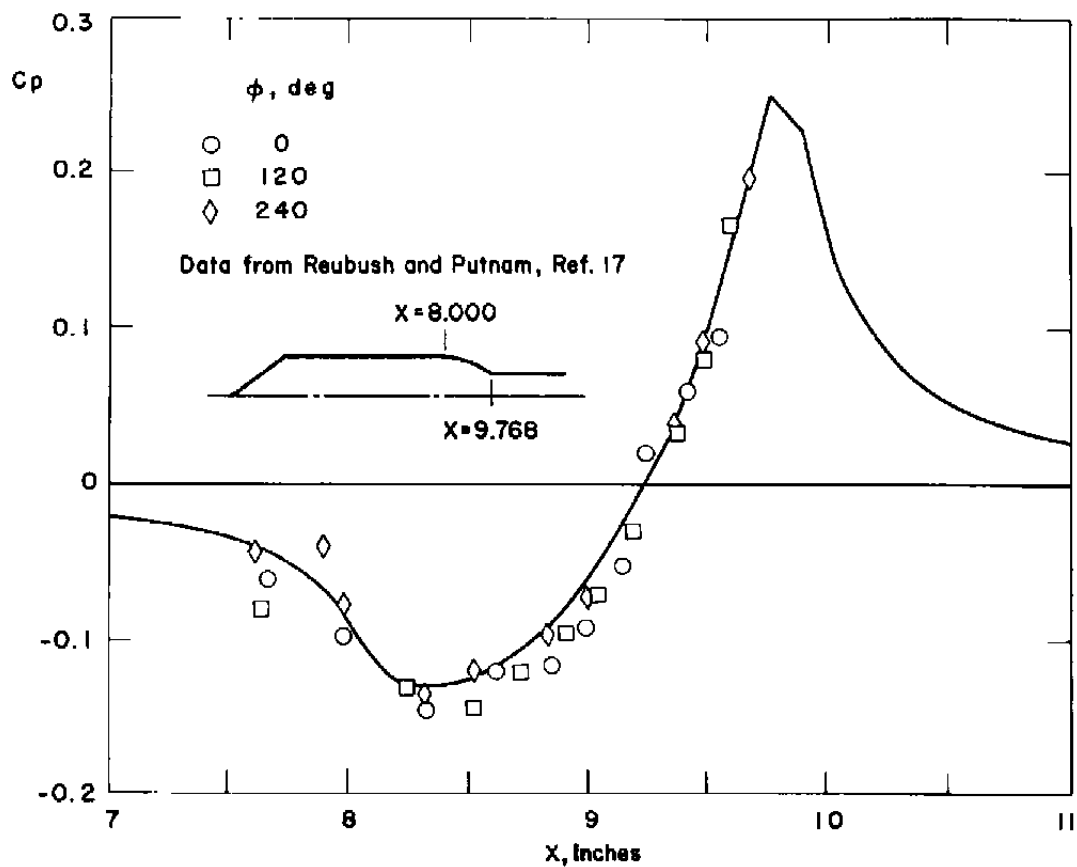
a.  $M_\infty = 0.6$ ,  $Re = 7 \times 10^6$

Figure 24. Longitudinal pressure coefficient distribution for the NASA Langley  $l/d = 1.768$  circular arc boattail in the Langley 1/3-meter cryogenic tunnel.



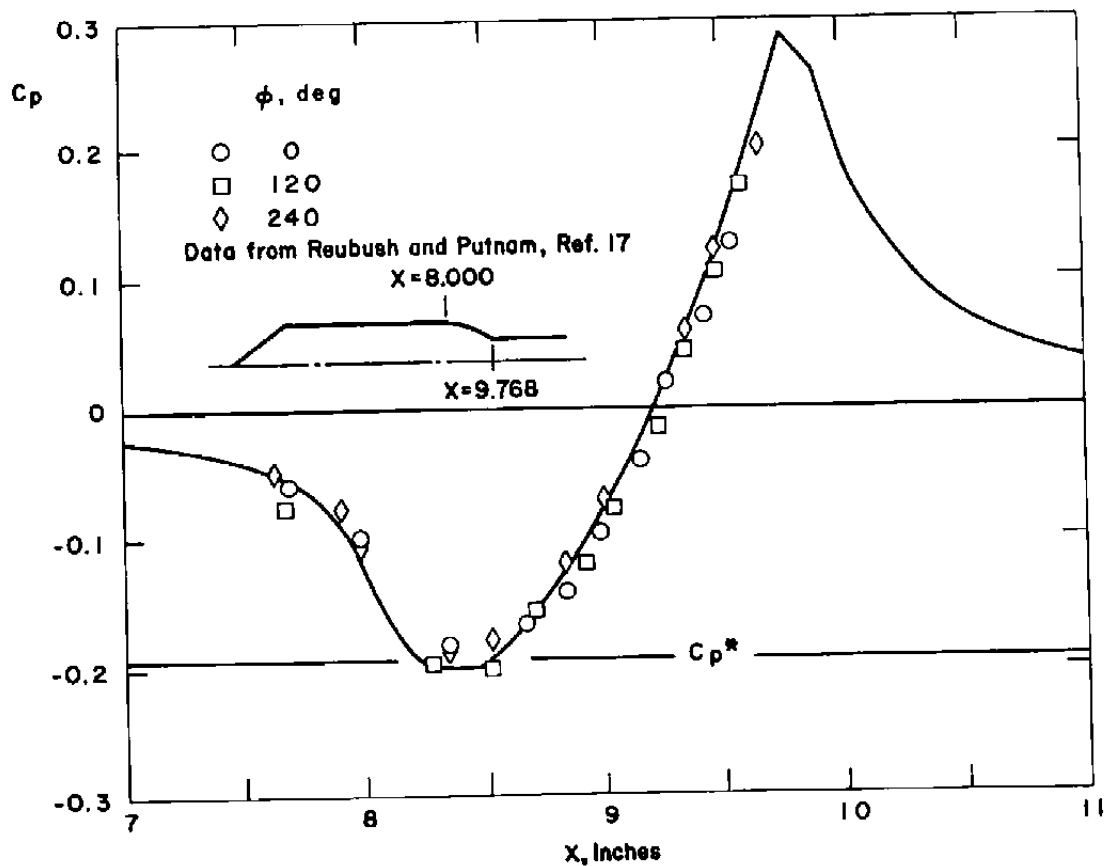
b.  $M_\infty = 0.6$ ,  $Re = 26 \times 10^6$

Figure 24. (Continued)



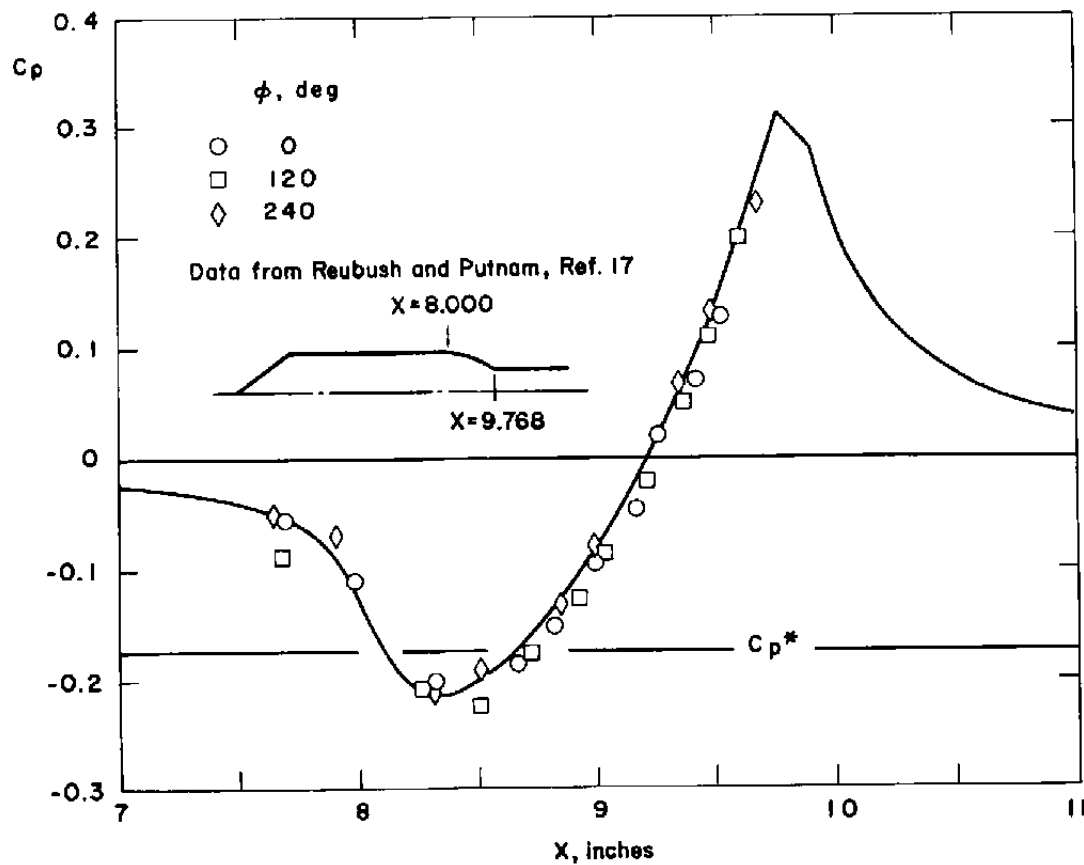
c.  $M_{\infty} = 0.6$ ,  $Re = 45 \times 10^6$

Figure 24. (Continued)



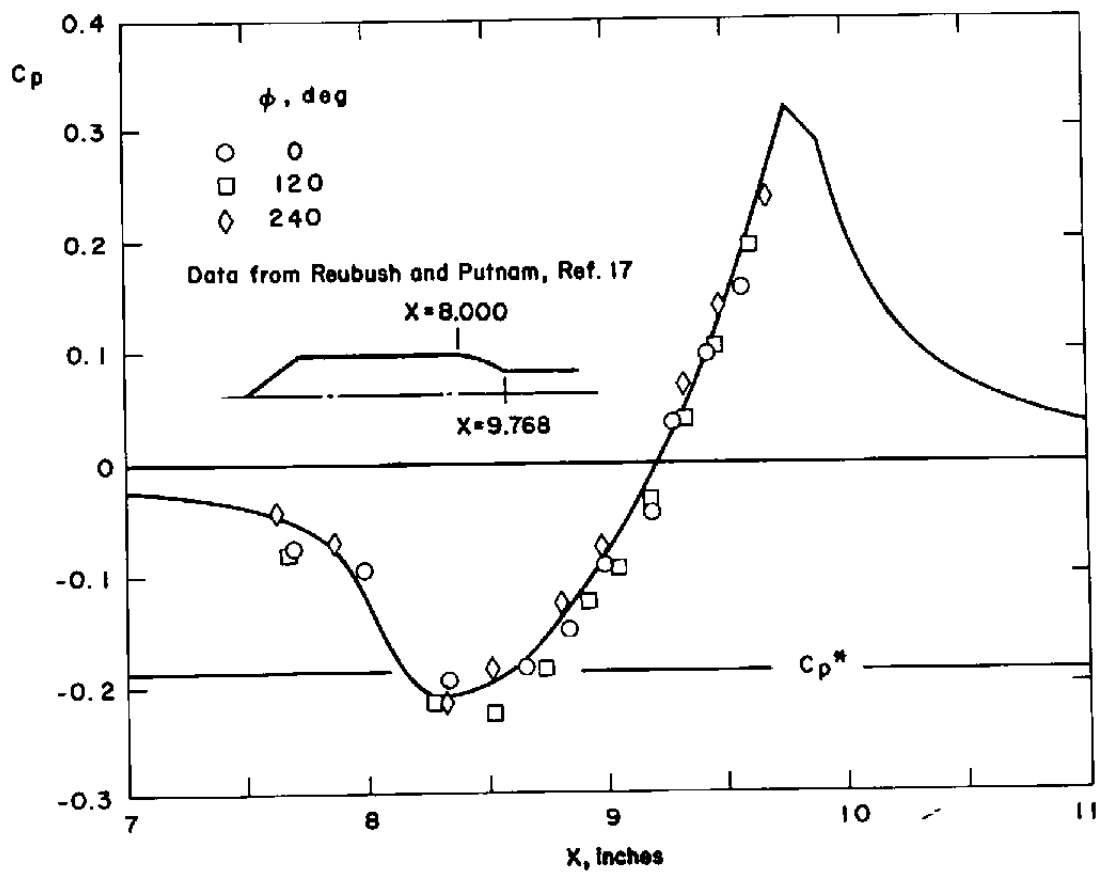
d.  $M_\infty = 0.9, Re = 7 \times 10^6$

Figure 24. (Continued)



e.  $M_\infty = 0.9$ ,  $Re = 22 \times 10^6$

Figure 24. (Continued)



f.  $M_\infty = 0.9$ ,  $Re = 53 \times 10^6$

Figure 24. (Continued)

experimental results used for comparison were those of Shrewsbury (76). The results of the CVI Program were anomalous at high Mach numbers, and as such are presented as Appendix C.

#### Real Plume Cases

NASA Langley circular arc boattail. The model used for the first real plume analysis, the NASA Langley  $l/d_m = 1.768$  circular arc boattail, was identical in external shape to the solid sting model presented earlier in this chapter, page 89, less, of course, the plume simulator. It was strut mounted, and the internal plumbing arrangements, used to furnish a "cold" plume, are shown in Figure 25.

Reubush and Runckel (73) tested a number of configurations at Mach numbers from 0.4 to 1.3 and nozzle pressure ratios (NPR's) from one (jet-off) to about six. The analysis and data presented herein are for the  $l/d_m = 1.768$  circular arc boattail at a Mach number of 0.8 for NPR's of approximately two and four.

The high pressure air was provided at essentially ambient conditions, and the wind tunnel used for the tests was the Langley 16-foot transonic tunnel, which was atmospheric. It was thus judged reasonable to assume the ratio of stagnation temperatures of the external and internal flows to be unity for the purposes of the plume and mixing calculations.

The plume was calculated using the Lockheed Method

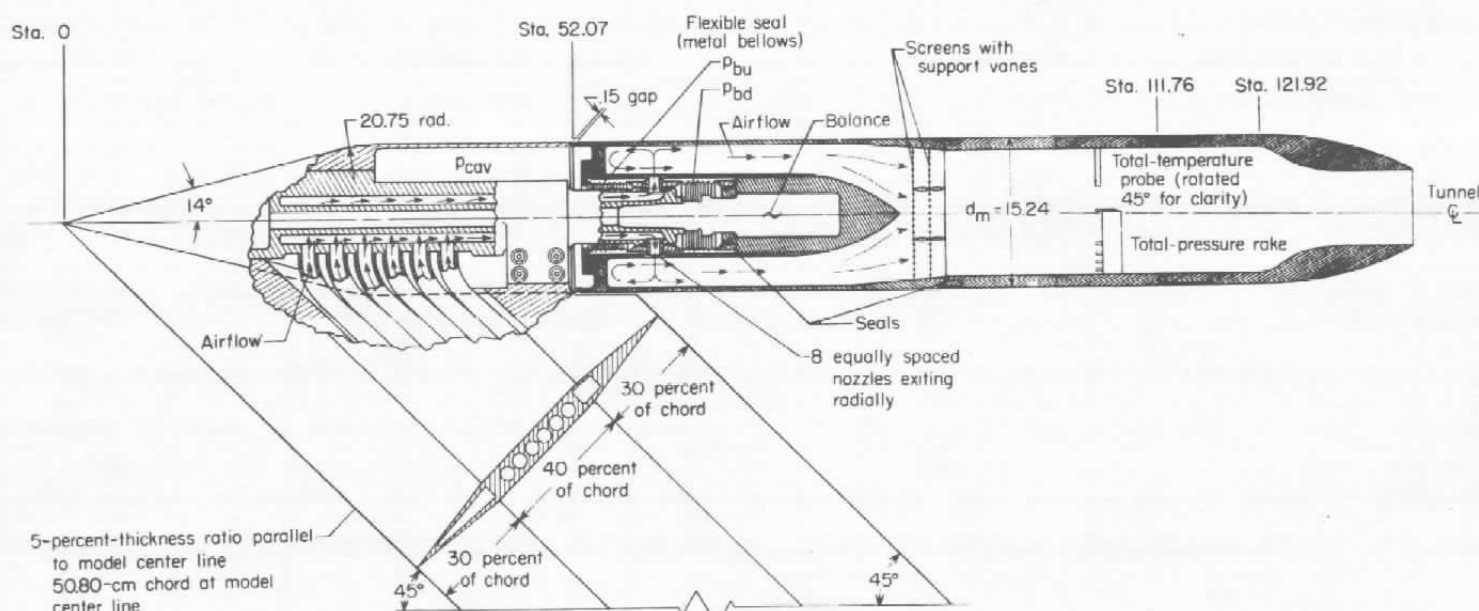


Figure 25. Sketch of air-powered cone-cylinder model with a typical circular-arc convergent nozzle installed.

of Characterisitcs Program based on the appropriate NPR. No inviscid/inviscid iteration was performed, that is to say, the external pressure was assumed to be a constant ambient value with no longitudinal variation. Thus, it must be realized that the plume shapes used in the analysis were most likely too large by a small amount, as the increased pressure in the compression at the end of the boattail, relative to tunnel ambient pressure, would tend to decrease the plume size in that area. Recovery to near ambient tunnel conditions was, however, fairly rapid.

To provide the velocity ratio,  $\phi_b$ , for use in the mixing program, DELPL, the velocity of the exhaust flow undergoing isentropic expansion to tunnel ambient pressure was used, along with the velocity of the wind tunnel evaluated also under ambient conditions. To furnish the appropriate conditions at the end of the nozzle, including the internal boundary displacement thickness at this point, a one-dimensional isentropic analysis was used based on plenum and nozzle geometries and known plenum conditions. The resulting boundary layer growth, calculated using the Bartz program, is shown in Figure 26. Also shown in this figure for comparison purposes is the result of the same calculation done with the recently available axisymmetric version of the Kuhn-Nielsen Separated Turbulent Boundary Layer Program (77), utilizing its boundary layer option. The final value of the displacement thickness of the nozzle was the value used as input to the mixing program. The corresponding value of the external boundary layer displacement thickness at this point was provided by the most recent calculation of the viscous portion of the CVI Program.

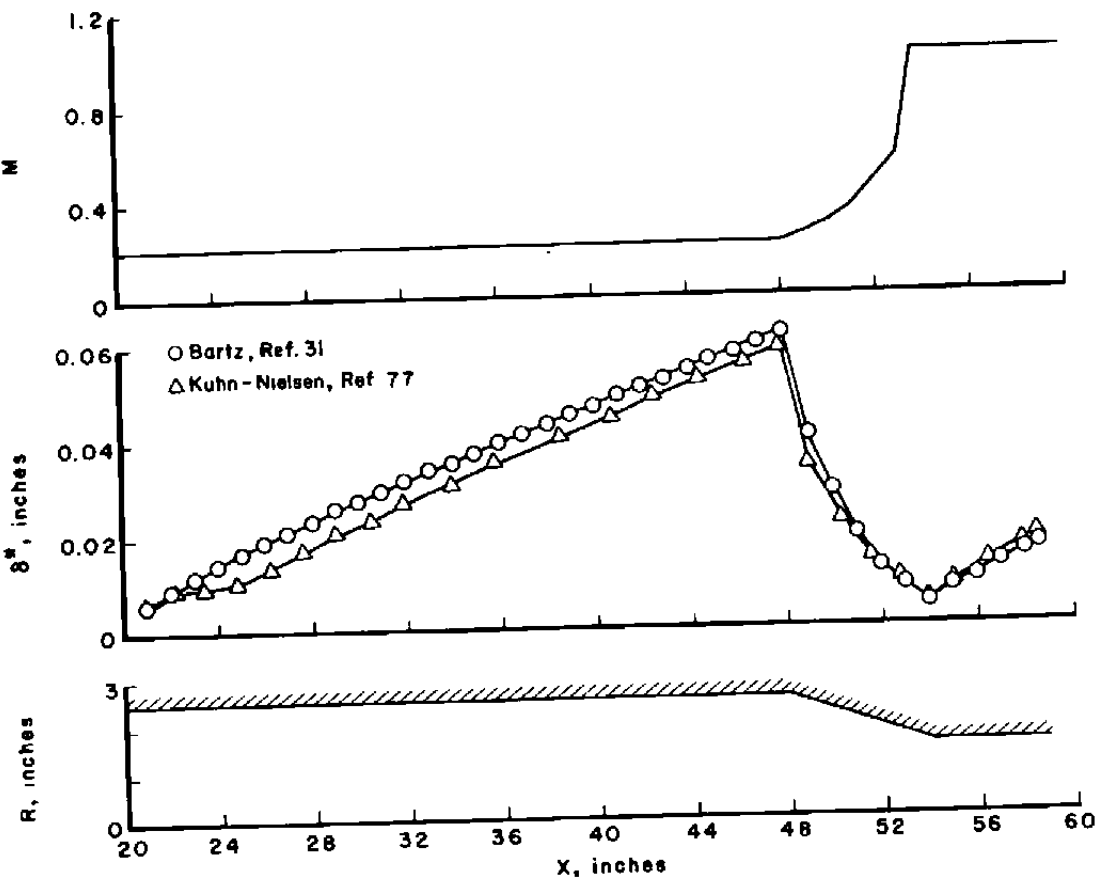


Figure 26. Boundary layer displacement calculation for the plenum and nozzle of the NASA Langley  $l/d_m = 1.768$  air-powered model.

Having specified all of the requirements of the mixing program, a number of calculations were made with the CVI Program, including DELPL, for different values of the mixing parameter,  $\sigma$ . As shown in Figures 27a and b, for NPR's of two and four, respectively, the circular arc boat-tail was analyzed with the appropriate plume shape for the "solid-body plume" case and for the mixing cases with the following values of  $\sigma$ , which were described in Chapter III, page 79:

- (a)  $\sigma_{II}$
- (b)  $\sigma_I$
- (c)  $\sigma_I/10$

It is emphasized that the plume shape was held constant during this analysis for purposes of isolating the entrainment effect. The value of  $\sigma$  may, in actual cases, never be as small as case (c),  $\sigma_I/10$ , since part of the  $\delta_e^*$  correction would be taken up by the actual changing plume shape. The choice of  $\sigma_I/10$  was arbitrary and was used to note the sensitivity of the solution to changes in  $\sigma$ .

For the two-stream value of  $\sigma$  in case (a), the difference between the  $C_p$  distribution and that of the solid body plume was so small as to be negligible. There is a slight improvement when the one-stream value of  $\sigma$ , case (b), is used particularly in the  $NPR = 4$  case, where the CVI Program prediction agrees well with the data except at the last two data points, which may be an indication of localized separation in that area. A small separated area was also a

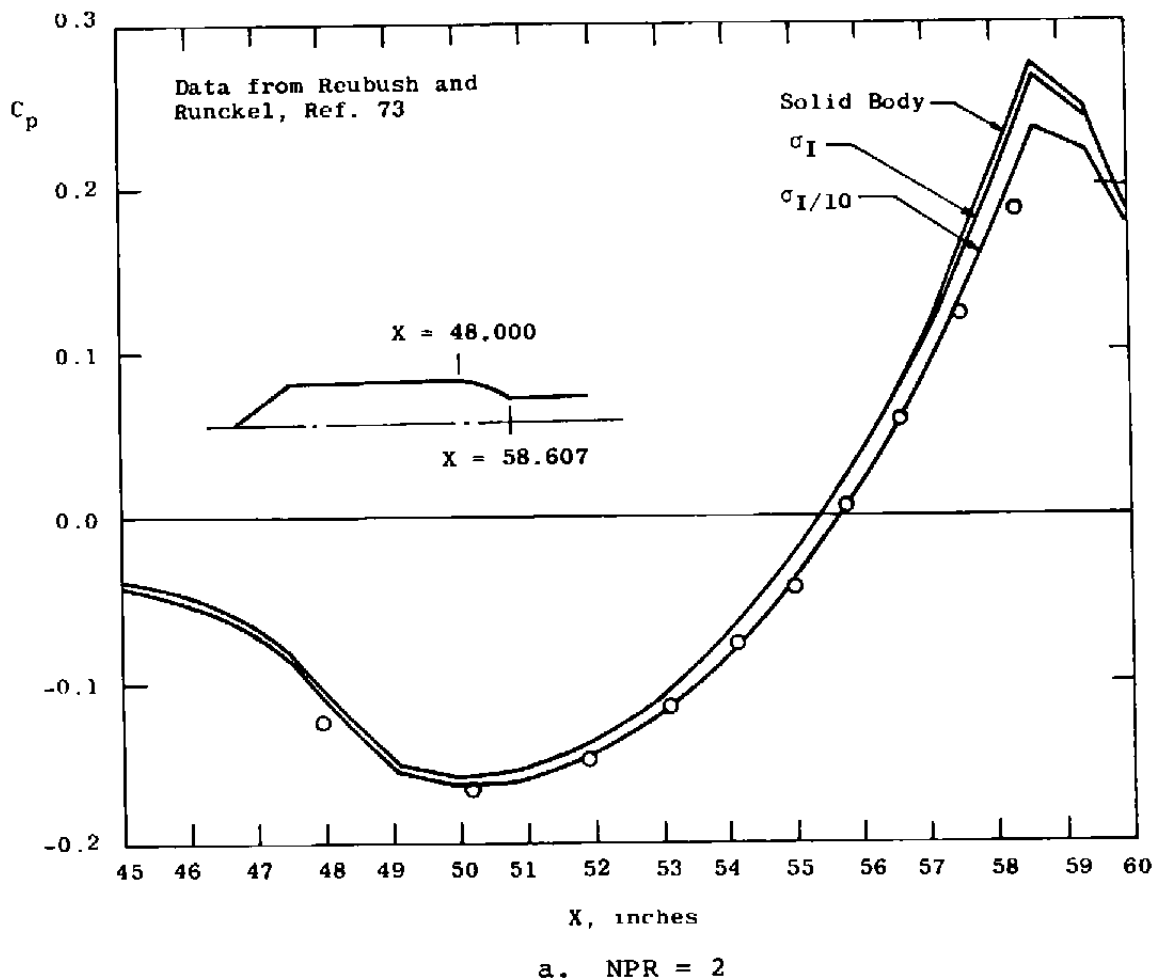


Figure 27. Longitudinal pressure coefficient distribution for the NASA Langley  $l/d_m = 1.768$  circular arc boattail with a real plume.

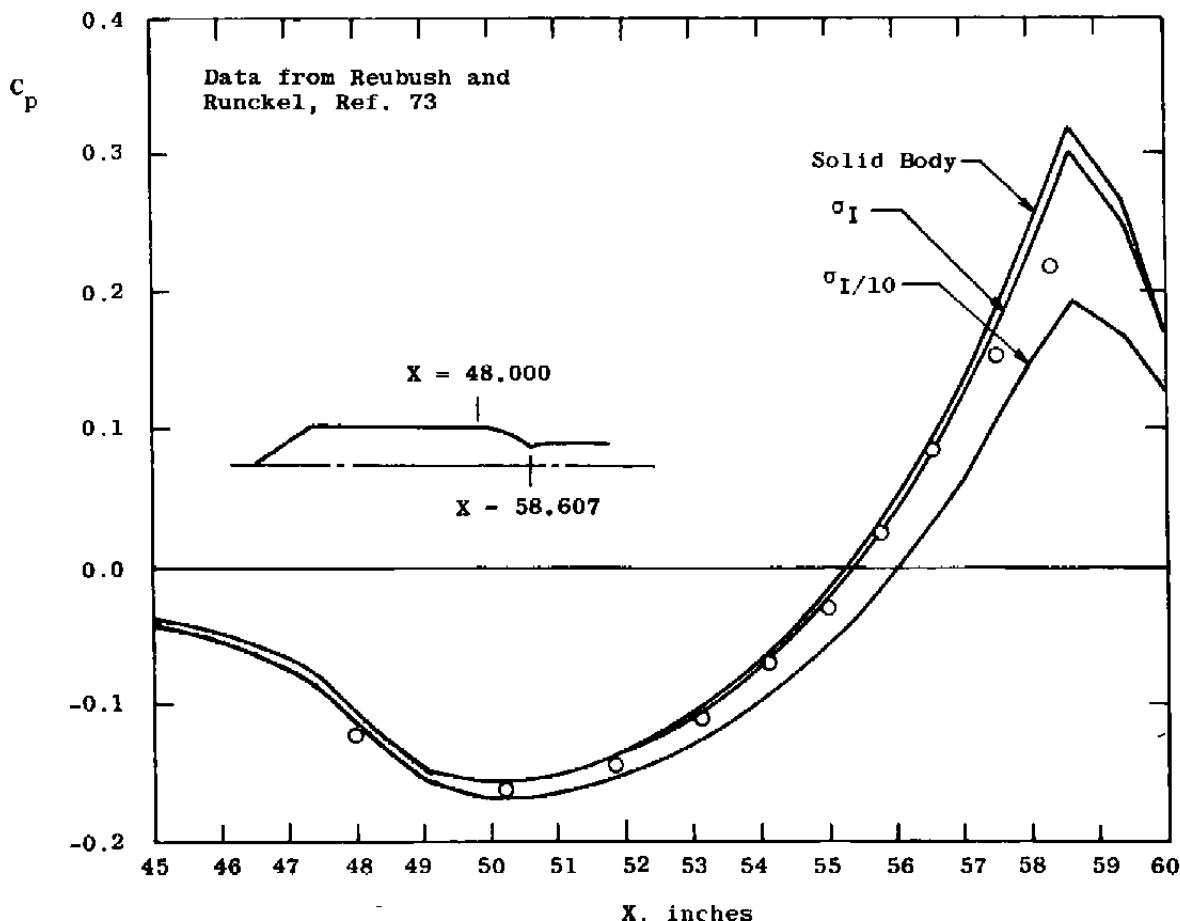


Figure 27. (Continued)

characteristic of the data in the solid sting case.

It was arbitrarily decided to run these cases with an extremely low value of  $\sigma$ , case (c), which would be indicative of very high mixing. As can be seen from Figure 27, this improves the results considerably for the  $NPR = 2$  case, yet causes a large over-correction in the  $NPR = 4$  case. This is a result of the much higher entrainment rate at a given  $\sigma$  value for the  $NPR = 4$  case, which has a  $\phi_b$  value of 0.585, compared to the rate for the  $NPR = 2$  case, which has a  $\phi_b$  value of 0.790, due to the difference in  $\phi_b$ . The large entrainment rate produces a much larger  $\delta_e^*$  in the  $NPR = 4$  case.

It may be seen from these cases that there is great room for improvement in the choice of  $\sigma$  for each point in the mixing calculation for a given configuration. But, qualitatively, it has also been shown herein that applying the  $\delta_e^*$  correction at points downstream of the nozzle exit is sufficient to influence correctly the pressures over the entire afterbody and, thus, that the displacement thickness correction method is a valid approach to the plume entrainment problem.

An example of the typical behavior of the  $\delta_e^*$ ,  $\delta_{rel}^*$ , and  $y$  in the area of the boattail and plume is shown in Figure 28.

AGARD 15-deg boattail. Another axisymmetric "cold" flow exhaust plume model was also analyzed with the CVI Program and compared with data. This model was the AGARD 15-deg

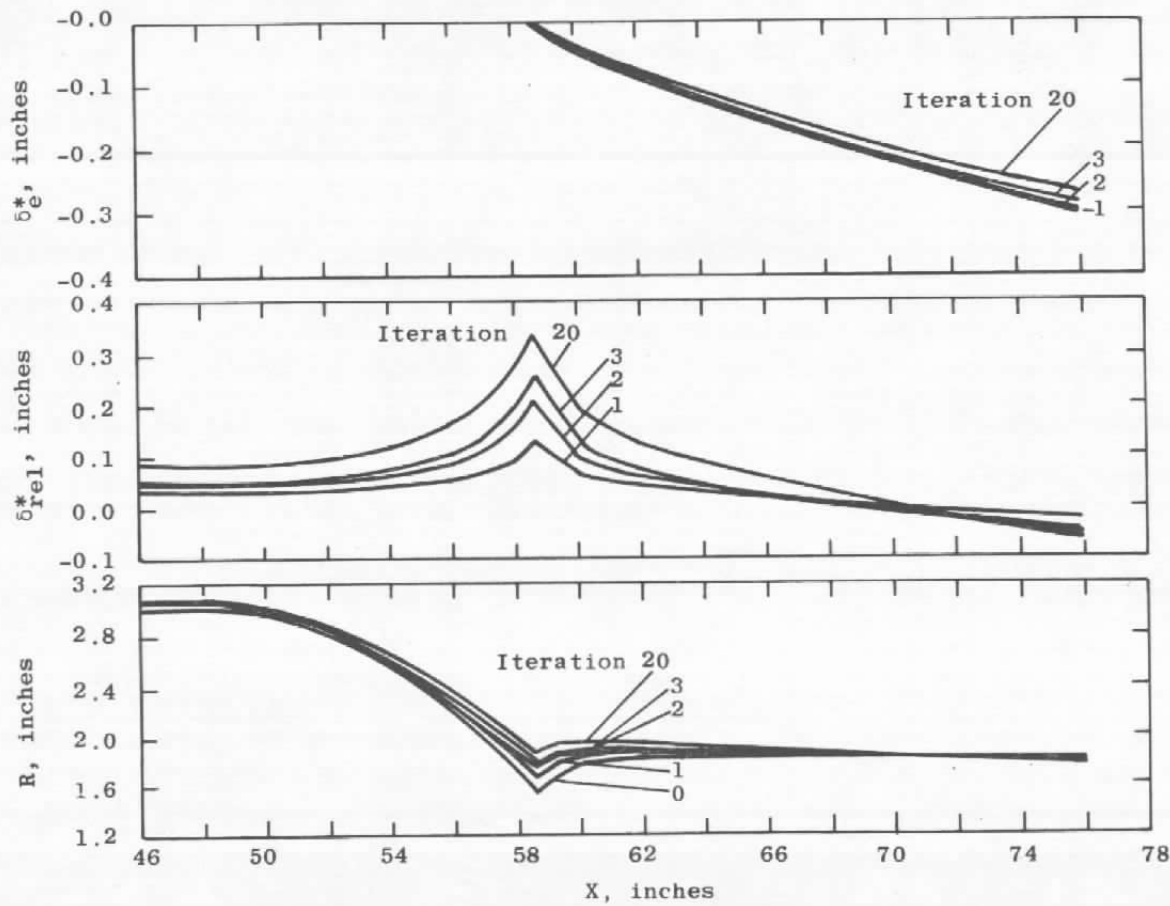


Figure 28. Boundary layer correction due to entrainment for the NASA Langley  $l/d_m = 1.768$  circular arc boattail for  $M_\infty = 0.8$ ,  $NPR = 4$ ,  $\sigma = \sigma_I$ .

Boattail (23), and it was chosen because of its geometry and the NPR's at which it was tested. As can be seen from Figure 29, the boattail is not only steeper near the exhaust plane than the Langley  $l/d_m = 1.768$  circular arc boattail, but it has a slightly lower closure ratio ( $d_{ex}/d_m$ ). In addition, the NPR's at which the AGARD 15-deg boattail was tested covered a greater range than those for the Langley boattail, three to seven in this case versus two to four in the former case. It was felt that the combination of these two effects would provide a more challenging case than the previous one.

The CVI Program Analysis was carried out at the two NPR's at a Mach number of 0.8. The results were compared with data from Reference (23), in which the model was tested in the AEDC 16-foot Transonic Wind Tunnel. The internal plumbing arrangements to provide high pressure air to the jet exhaust were very similar to those of the Langley tests, thus an isentropic one-dimensional analysis was utilized to obtain conditions in the plenum and at the nozzle exit. The methods of estimating the necessary boundary layer and velocity parameters for use in the mixing program were also used exactly as in the previous subchapter.

The comparisons between the theory and the data are shown in Figures 30a and b. General agreement between the two is fair in both cases, but some points must be made concerning the comparisons. Firstly, the grid points at the shoulder of the boattail, where the flow is expanding the most, miss the point of minimum pressure. This particular misplacement of

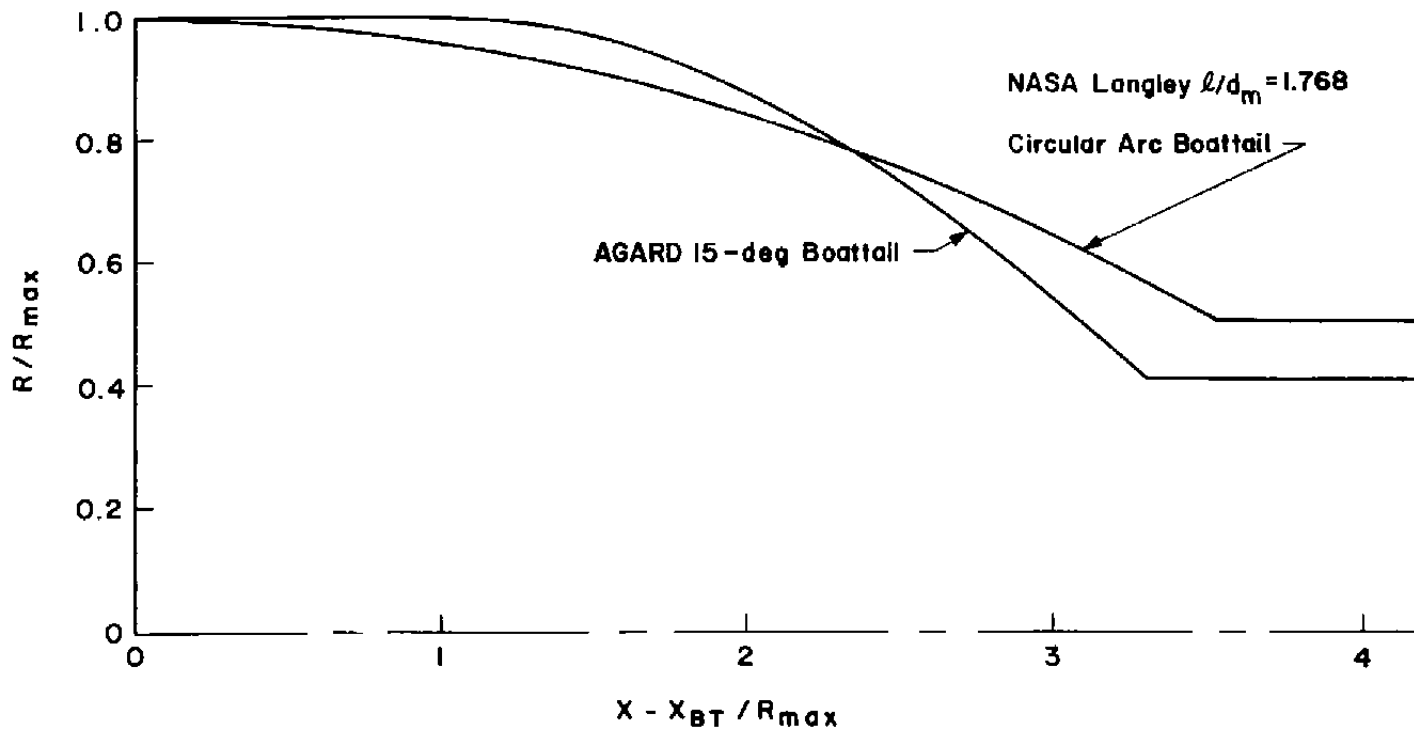
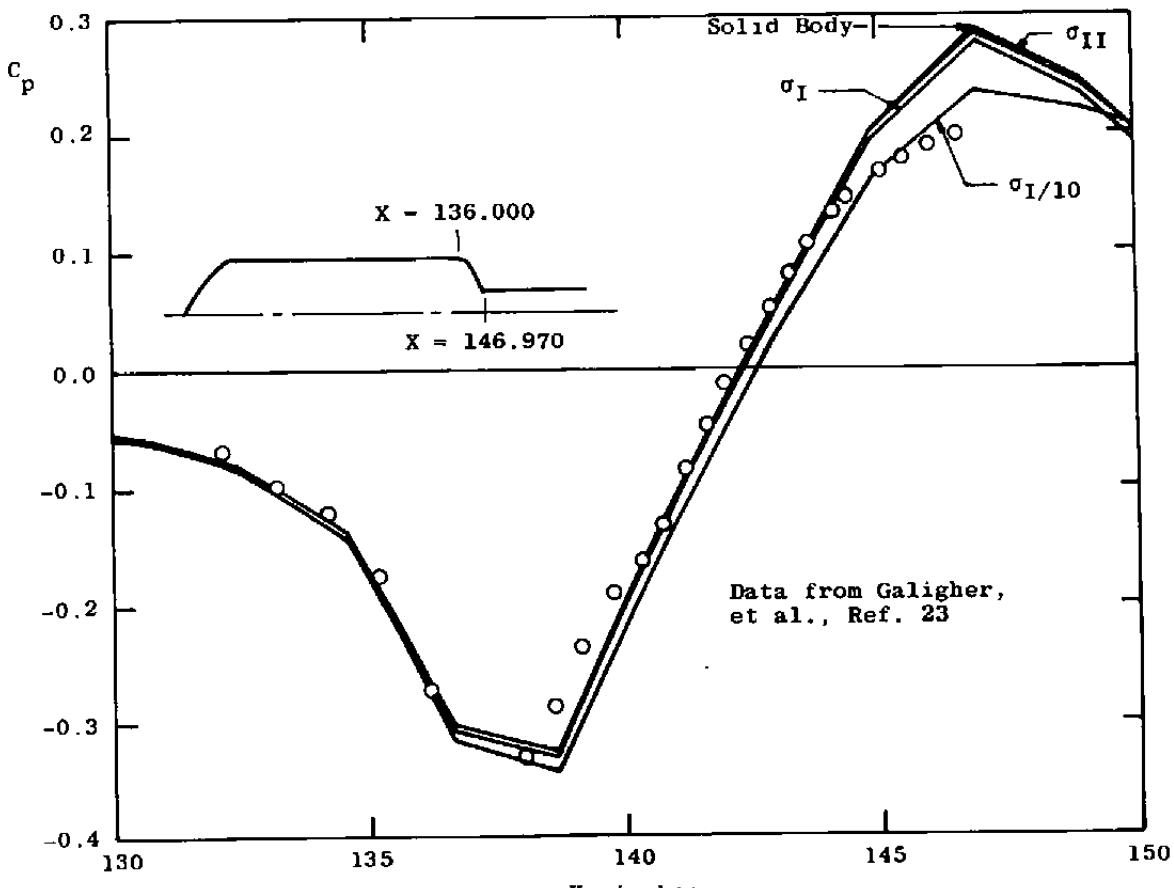
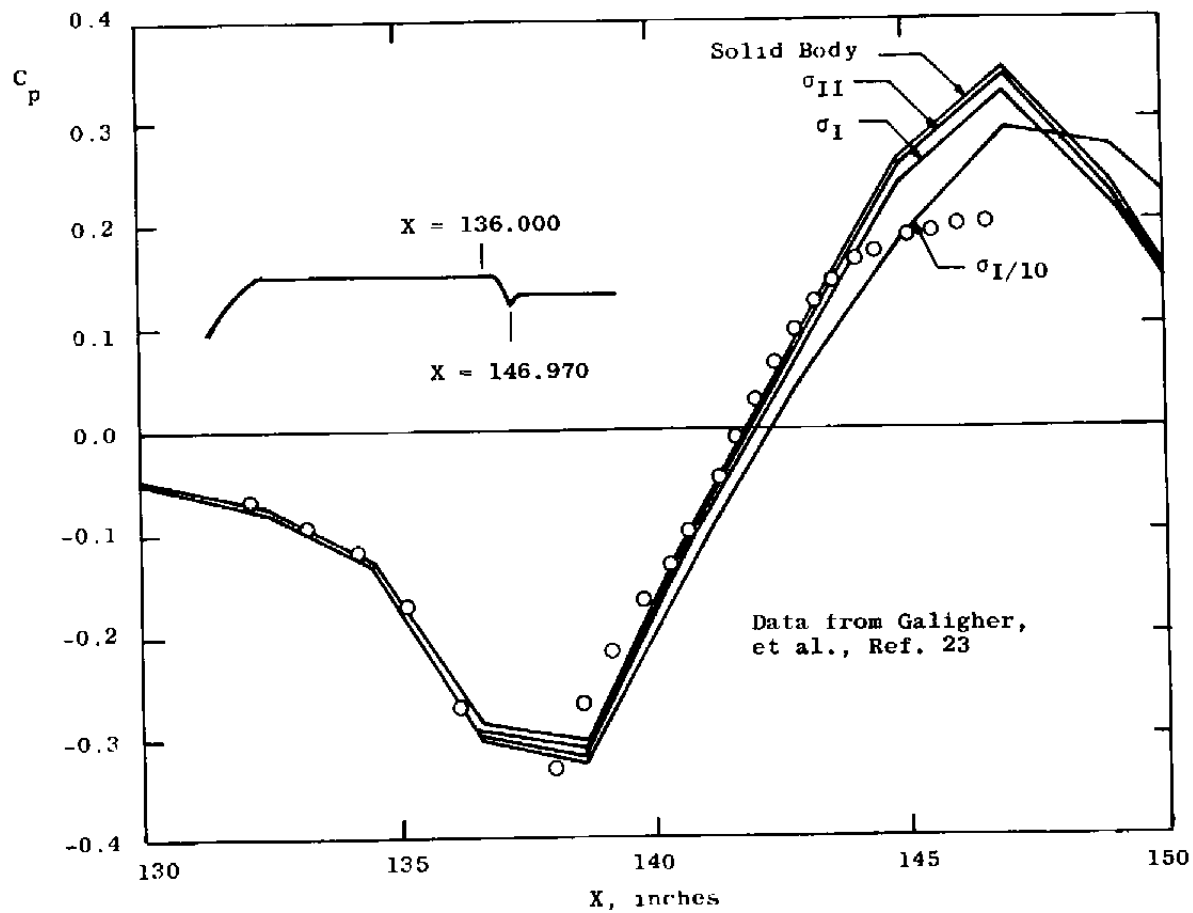


Figure 29. Comparison of boattail and plume simulator shapes between the NASA Langley  $l/d_m = 1.768$  circular arc boattail and the AGARD 15-deg boattail.



a.  $NPR = 3$

Figure 30. Longitudinal pressure coefficient distribution for the AGARD 15-deg boattail.



b.  $NPR = 7$   
Figure 30. (Continued)

points could not have been predicted, nor could it have been recognized without the comparison with the data shown in this figure. It would be suggested, then, that future analyses cluster the points in this area, and that once a successful analysis has been completed, the grid points be shifted slightly to check for sharp gradients near the shoulder. Secondly, there appears to be a rather large separated region near the end of the boattail. This is especially noticeable in the  $NPR = 7$  case. This invalidates the results of the CVI Program in this area of the analysis.

Thirdly, the results of changing the value of  $\sigma$  from  $\sigma_{II}$  to  $\sigma_I$  and then to  $\sigma_I/10$  are more consistent in these cases than in the Langley circular arc boattail case. This may be due to the fact that the values  $\phi_b$  in this case were closer than in the previous case, 0.653 and 0.530 versus 0.790 and 0.585. Thus, the difference in entrainment characteristics and hence  $\delta_e^*$  variations were not as pronounced in this case as in the previous case.

The analysis of the AGARD 15-deg boattail thus points out the qualitative ability of the CVI Program and the mixing model to predict real plume flows, but it is apparent that further work must be done on the determination of the longitudinal variation of  $\sigma$  at each iteration, and that the important and complex interaction between the plume, external inviscid flow, and separated boundary layer must be studied in detail.

## CHAPTER V

## CONCLUSIONS AND RECOMMENDATIONS

The objective of this study was to develop a method for prediction of the transonic flow about an arbitrary axisymmetric body. The impetus for the effort was the desire to compute the flow over nacelle afterbodies for purposes of drag estimation, but this objective was quickly extended to include other axisymmetric bodies, such as equivalent bodies of revolution. Such flows may exhibit strong interactions between the external inviscid flow and the viscous flow near the body, which may include large regions of locally sonic flow, near-normal shock waves, and extensive separated areas. If the axisymmetric body also includes a jet exhaust plume, the interactions are even more complex, including now the inviscid flow of the plume and the turbulent mixing between the plume flow and the external flow.

Many analytic methods for solving problems of this sort were examined. Following this effort, a combined viscous/inviscid iterative digital computer program was developed which served as a means for obtaining the flow predictions, including the effect of boundary layer, for comparison with various data. Finally, a turbulent mixing analysis, based on the Chapman-Korst mixing theory, was used to determine the effect of plume entrainment on the afterbody

pressures. The conclusions and recommendations below are the result of all of the efforts outlined above.

1. Examining contemporary works revealed that the viscous/inviscid approach to problems of this sort was by far the most popular. One interesting approach used the Navier-Stokes equations in the afterbody/sting area.
2. The comparison of the results of the method of analysis developed herein to data leads to certain conclusions with respect to the physical phenomena involved:
  - (a) The predictions agree well with the data if the flow is unseparated. This restricts the angle of the end of the boat-tail to approximately 20 degrees, with larger angles tending to cause separation of the flow at almost all Mach numbers.
  - (b) Care must be taken in analyzing the results of the method at the upper transonic Mach numbers, where the separation problem is greatly intensified.
  - (c) The slight overcompression predicted at the junction of the afterbody and solid sting is there even in otherwise well behaved cases. This may indicate a small separated area or an inaccuracy in the value

of  $\delta^*$  at this point for all configurations and Mach numbers, even quite moderate ones. Thus, slight inaccuracies at this point are to be expected even if the extreme condition of (a) and (b) are avoided.

- (d) The standing shock developing at the afterbody shoulder which increases in strength and moves backward with increasing Mach number, is predicted quite accurately by this method.
- (e) For most bodies, the boundary layer effect is not important upstream of the boattail. This will not be true for bodies with exotic forebody curvatures, however.

### 3. Concerning the CVI Program:

- (a) Relaxation of the addition of the boundary layer displacement thickness may increase the rate of convergence or, in some cases, make the difference between convergence or divergence.
- (b) The South-Jameson Transonic Program (RAXBOD) is well suited for use in the CVI Program. Care should be taken, however, in the results of some of the calculations for bodies with high body radius gradients at high subsonic Mach numbers, particularly if the results vary noticeably in form from

from results at lower Mach numbers (see Appendix C).

(c) The Bartz boundary layer program has the capability of continuing the solution through areas of high pressure gradients, which makes it valuable in the initial stages of the viscous/inviscid iteration. This same characteristic will sometimes produce converged solutions in the CVI Program even if the flow is actually separated. Any unusual behavior of the Bartz program, particularly any unusual variation of the displacement thickness calculation, must be considered suspect. It is recommended that this program be replaced by a more accurate boundary layer program in the latter stages of the CVI Program iterations.

(d) It is recommended that a method of characteristics program be incorporated into the CVI Program to enable calculation of a real plume. This would provide an automated inviscid/inviscid iteration capability in addition to the viscous/inviscid iteration capability presently existing.

4. The application of the Chapman-Korst mixing theory to the modification of the plume boundary has the advantage of easy implementation as well as being physically satisfying. The derivation of the equations, although restricted to two-dimensional isobaric flow, included terms accounting for the variation from the fully developed similar solution of Korst and Chow (51) due to initial boundary layer shape. The displacement thickness correction,  $\delta_e^*$ , due to plume entrainment was applied directly to the boundary layer which was calculated assuming the plume to be, at first, a solid body. Certain modifications of the theory, however, are recommended: (a) the basic equations should be rederived for the axisymmetric case and a longitudinal pressure distribution, and (b) the mixing parameter,  $\sigma$ , should be calculated on the basis of conservation of momentum considerations at each longitudinal point, as in the work of Bauer and Matz (47), rather than computed on the basis of previous work, as is currently done. The values of  $\sigma$  should be recalculated at least everytime that the plume shape is redefined.
5. It is felt that the highly complex problem of turbulent separated flow with plume entrainment

effects is of sufficient practical importance to be investigated in future efforts. In particular, it is recommended that the recently developed Kuhn and Nielsen Axisymmetric Turbulent Separated Boundary Layer Program (77) be modified by the addition of a plume entrainment segment of the program based on the Chapman-Korst mixing theory similar to the work contained herein.

## BIBLIOGRAPHY

1. Calarese, W. "Review of Methods of Solution of Afterbody/Exhaust Nozzle Flow Fields," AFFDL-TR-74-108, January 1974.
2. Grossman, B. and Melnik, R. "Some Preliminary Results of the Numerical Computation of Two Classes of Transonic Interaction Problems," Grumman Research Department Memorandum RM-577, August 1973, AD766599.
3. Grossman, B. and Melnik, R. "The Numerical Computation of the Transonic Flow over Afterbodies Including the Effect of Jet-Plume and Viscous Interactions," AIAA Paper No. 76-62, AIAA 13th Aerospace Sciences Meeting, Pasadena, California, January 1975.
4. Green, J. E., Weeks, D. J., and Brooman, J. W. F. "Prediction of Turbulent Boundary Layers by a Lag-Entrainment Method," R.A.E. Technical Report 72231, January 1973.
5. Yaeger, L. S. "Transonic Flow over Afterbodies Including the Effects of Jet-Plume and Viscous Interactions with Separation," AIAA Paper No. 77-228, AIAA 15th Aerospace Sciences Meeting, Los Angeles, California, January 1977.
6. Presz, W. "Turbulent Boundary Layer Separation on Axisymmetric Afterbodies," Ph.D Dissertation, University of Connecticut, Storrs, Connecticut, 1974.
7. Keith, J. S., Ferguson, D. R., Merkle, C. L., Heck, P. H., and Lahti, D. J. "Analytical Method for Predicting the Pressure Distribution about a Nacelle at Transonic Speeds," NASA CR-2217, July 1973.
8. Rom, J. and Bober, L. J. "Calculation of the Pressure Distribution on Axisymmetric Boattails Including Effects of Viscous Interactions and Exhaust Jets in Subsonic Flow," NASA TM X-3109, September 1974.
9. Chow, W. L., Bober, L. J., and Anderson, B. H. "Numerical Calculation of Transonic Boattail Flow," NASA TN D-7984, June 1975.

10. Bower, W. W. "An Analytical Procedure for the Calculation of Attached and Separated Subsonic Diffuser Flows," AIAA Paper No. 74-1173, Presented at the AIAA/SAE 10th Propulsion Conference, San Diego, California, October 1974.
11. Calarese, W. "An Analytical Method to Compute Viscous-Inviscid Transonic Flow on Axisymmetric Afterbodies Including Jet Effects and Boattail Bleed in Separated Regions," AIAA Paper No. 75-1293, AIAA/SAE 11th Propulsion Conference, Anaheim, California, September-October 1975.
12. McDonald, H. and Hughes, P. F. "A Correlation of High Subsonic Afterbody Drag in the Presence of a Propulsive Jet or Support Sting," Journal of Aircraft, Vol. 2, No. 3, May-June 1965. Pp. 202-207.
13. Moulden, T. H., Wu, J. M., and Spring, D. J. "A Discussion of Transonic Base Flows in the Presence of a Propulsive Jet," Progress in Astronautics and Aeronautics, Vol. 40, 1976. Pp. 425-447.
14. Wu, J. M., Moulden, T. H., and Uchiyama, N. "Aerodynamic Performance of Missile Configurations at Transonic Speeds Including the Effects of a Jet Plume," U. S. Army Missile Command Technical Report RD-76-23, March 1976.
15. Nash, J. F. "A Practical Calculation Method for Compressible Turbulent Boundary-Layer in Two-Dimensional Flows," Lockheed Georgia Research Memo, ER9428, 1967.
16. Proceedings of the Propulsion Interactions Workshop held at Langley Research Center, Hampton, Virginia 23665, May 19-20, 1976, Sponsored by the Propulsion Aerodynamics Branch, High-Speed Aerodynamics Division, Mail Stop 189.
17. Reubush, D. E. and Putnam, L. E. "An Experimental and Analytical Investigation of the Effect on Isolated Boattail Drag of Varying Reynolds Number up to  $130 \times 10^6$ ," NASA TN D-8210, May 1976.
18. Putnam, L. E. and Abeyounis, W. K. "Experimental and Theoretical Study of Flow Fields Surrounding Boattail Nozzles at Subsonic Speeds," AIAA Paper No. 76-675, Presented at the AIAA/SAE 12th Propulsion Conference, Palo Alto, California, July 1976.

19. Wilmoth, R. G. "Analytical Study of Viscous Effects on Transonic Flow over Boattail Nozzles," AIAA Paper No. 77-223, Presented at the AIAA 15th Aerospace Sciences Meeting, Los Angeles, California, January 1977.
20. Cosner, R. R. and Bower, W. W. "A Patched Solution of the Transonic Flow Fields About an Axisymmetric Boattail," AIAA Paper No. 77-227, Presented at the AIAA 15th Aerospace Sciences Meeting, Los Angeles, California, January 1977.
21. Yaros, S. F. "Prediction of Pressure Distributions on Axisymmetric Bodies in Transonic Flow," AIAA Paper No. 77-226, Presented at the AIAA 15th Aerospace Sciences Meeting, Los Angeles, California, January 1977.
22. Holst, T. L. "Numerical Solution of Axisymmetric Boat-tail Fields with Plume Simulators," AIAA Paper No. 77-224, Presented at the AIAA 15th Aerospace Sciences Meeting, Los Angeles, California, January 1977.
23. Galigher, L. L., Yaros, S. F., and Bauer, R. C. "Evaluation of Boattail Geometry and Exhaust Plume Temperature Effects on Nozzle Afterbody Drag at Transonic Mach Numbers," AEDC-TR-76-102, October 1976.
24. South, J. D., Jr. and Jameson, A. "Relaxation Solutions for Inviscid Axisymmetric Transonic Flow over Blunt or Pointed Bodies," Proceedings of the AIAA Computational Fluid Dynamics Conference, Palm Springs, California, July 19-20, 1973. Pp. 8-17.
25. Lipnitskii, Iu. M. and Lifshits, Iu. B. "Analysis of Transonic Flow Past Solids of Revolution," PMM, Vol. 34, No. 3, 1970. Pp. 508-513.
26. Yoshihara, H. "A Survey of Computational Methods for 2D and 3D Transonic Flows with Shocks," GDCA-ERR-1726, General Dynamics Convair Aerospace Division, December 1972.
27. Akima, H. "A New Method of Interpolation and Smooth Curve Fitting Based on Local Procedures," Journal of the Association for Computing Machinery, Vol. 17, No. 4, October 1970. Pp. 589-602.
28. Keller, J. D. and South, J. C., Jr. "RAXBOD: A Fortran Program for Inviscid Transonic Flow over Axisymmetric Bodies," NASA TM X-72831, February 1976.

29. Kuhn, G. D. and Nielsen, J. N. "Prediction of Turbulent Separated Boundary Layers in Subsonic and Transonic Flows," AIAA Paper No. 73-663, Presented at the AIAA 6th Fluid and Plasma Dynamics Conference, Palm Springs, California, July 1973.
30. Tucker, M. "Approximate Calculation of Turbulent Boundary-Layer Development in Compressible Flow," NACA Technical Note 2337, April 1951.
31. Bartz, D. R. "Turbulent Boundary-Layer Heat Transfer from Rapidly Accelerating Flow of Rocket Combustion Gases and of Heated Air," Advances in Heat Transfer, Vol. 2, Academic Press, New York, 1965.
32. Mayne, A. M., Jr. "A Method for Computing Boundary-Layer Flows, Including Normal Pressure Gradient and Longitudinal Curvature Effects," AEDC-TR-75-21, April 1975.
33. Whitfield, D. L. "Analytical, Numerical, and Experimental Results on Turbulent Boundary Layers," AEDC-TR-76-62, July 1976.
34. Patankar, S. V. and Spalding, D. B. Heat and Mass Transfer in Boundary Layers. CRC Press, Cleveland, Ohio, 1968.
35. Chou, Y-L. "An Analysis by the Green's Function Method for Flow over Axisymmetric Bodies Including the Transverse Curvature Effect," Ph.D Thesis, University of Tennessee, Knoxville, Tennessee, August 1976.
36. Moulden, T. H., Wu, J. M., and Spring, D. J. "Model of the Engine Exhaust System at Transonic Flight Speeds," Journal of Aircraft and Rockets, Vol. 12, No. 7, July 1975. Pp. 428-433.
37. Ratliff, A. W., Smith, S. D., and Penny, M. M. "Rocket Exhaust Plume Computer Program Improvement, Volumes I-IV," Lockheed Missiles and Space Company Reports LMSC/HREC D162220-I, -II, -III, and -IV, Huntsville, Alabama, January 1972.
38. Reubush, D. R. "Experimental Study of the Effectiveness of Cylindrical Plume Simulators for Predicting Jet-On Boattail Drag at Mach numbers up to 1.30," NASA TN D-7795, 1974.
39. Chapman, A. J. "Mixing Characteristics of a Free-Jet Boundary with Consideration of Initial Boundary Layer Configuration," Ph.D Thesis, University of Illinois, July 1953.

40. Korst, H. H., Page, R. H., and Childs, M. E. "Compressible Two-Dimensional Jet Mixing at Constant Pressure," University of Illinois, Mechanical Engineering Department, ME Technical Note 392-1, April 1954.
41. Korst, H. H., Page, R. H., and Childs, M. E. "A Theory for Base Pressures in Transonic and Supersonic Flow," University of Illinois, Mechanical Engineering Department, ME Technical Note 392-2, March 1955.
42. Korst, H. H., Page, R. H., and Childs, M. E. "Compressible Two-Dimensional Jet Mixing at Constant Pressure - Tables of Auxiliary Functions for Fully Developed Mixing Profiles," University of Illinois, Mechanical Engineering Department, ME Technical Note 392-3, April 1955.
43. Korst, H. H. and Chow, W. L. "Compressible Non-Isoenergetic Two-Dimensional Turbulent ( $Pr_t = 1$ ) Jet Mixing at Constant Pressure - Auxiliary Integrals, Heat Transfer and Friction Coefficients for Fully Developed Mixing Profiles," University of Illinois, Mechanical Engineering Department, ME Technical Note 392-4, January 1959.
44. Korst, H. H., Chow, W. L., and Zumwalt, G. W. "A Research on Transonic and Supersonic Flow of a Real Fluid at Abrupt Increases in Cross Section (with Special Consideration of Base Drag Problems) - Final Report," University of Illinois, Mechanical Engineering Department, ME Technical Note 392-5, December 1959.
45. Chow, W. L. and Korst, H. H. "On the Flow Structure Within a Constant Pressure Compressible Turbulent Jet-Mixing Region," University of Illinois, Department of Mechanical and Industrial Engineering, ME-TN-393-1, July 1962.
46. Hill, W. G., Jr. "Initial Development of Compressible Turbulent Free Shear Layers," Ph.D Thesis, Rutgers-The State University, May 1966.
47. Bauer, R. C. and Matz, R. J. "Influence of Initial Boundary Layer on the Two-Dimensional Turbulent Mixing of a Single Stream," AEDC-TR-71-79, April 1971.
48. Bauer, R. C. "An Analysis of Two-Dimensional Laminar and Turbulent Compressible Mixing," AIAA Journal, Vol. 4, No. 3, March 1966. Pp. 392-395.

49. Bauer, R. C. and Fox, J. H. "An Application of the Chapman-Korst Theory to Supersonic Nozzle-Afterbody Flows," AEDC-TR-76-158, January 1977.
50. Childs, M. E. "Two-Dimensional Turbulent Mixing Between Parallel Incompressible Jets Considering Effects of Initial Boundary Layer Configuration," Ph.D Thesis, University of Illinois, 1956.
51. Korst, H. H. and Chow, W. L. "Non-Isoenergetic Turbulent ( $Pr_t = 1$ ) Jet Mixing Between Two Compressible Streams at Constant Pressure," University of Illinois, Department of Mechanical and Industrial Engineering, ME Technical Note 393-2, April 1965.
52. Moulden, T. H. "On the Motion of a Viscous Fluid," Ph.D Thesis, University of Tennessee, Knoxville, Tennessee, June 1973.
53. Görtler, H. "Berechnung von Aufgaben der freien Turbulenz auf Grund eines neuen Naherungsansatzes," ZAMM 22, 1942. Pp. 244-254.
54. Pai, S. I. "Two-Dimensional Jet Mixing of a Compressible Fluid," Journal of the Aeronautical Sciences, August 1949. Pp. 463-469.
55. Abramowitz, M. and Stegun, I. A. (Eds.) "Handbook of Mathematical Functions with Formulas, Graphs, and Mathematical Tables," National Bureau of Standards, Applied Mathematics Series, 55, U. S. Government Printing Office, Washington, D. C., Ninth Printing, November 1970. Pp. 887-888.
56. Crocco, L. "Sulla Transmissione del Calore da una Lamina piana a un Fluide Scorente ad alta Velocita," L'Aerotechnica, Vol. XII, No. 2, February 1932. Pp. 181-197. (Transmission of Heat from a Flat Plate to a Fluid Flowing at a High Velocity, NACA TM No. 690, October 1932.)
57. Shapiro, A. H. The Dynamics and Thermodynamics of Compressible Fluid Flow. Vol. II, The Ronald Press Company, New York, 1954. P. 1115.
58. van Driest, E. R. "The Turbulent Boundary Layer with Variable Prandtl Number," in 50 Jahre Grenzschichtforschung, Friedr. Vieweg und Sohn, Braunschweig, 1955. Pp. 257-271.
59. Reichardt, H. "Gesetzmässigkeiten der freien Turbulenz," VDI - Forschungsheft, 414, Berlin, 1942.

60. Liepmann, H. W. and Laufer, J. "Investigations of Free Turbulent Mixing," NACA TN 1257, August 1947.
61. Tollmien, W. "Berechnung der Turbulenten Ausbreitungsvorgänge," ZAMM, 6, 1926. Pp. 468-478. Also NACA TM 1085, September 1945.
62. Cordes, G. "Untersuchung zur Statischen Druckmessung in Turbulenter Stromung," Ing. Arch., Vol. 8, No. 4. Pp. 245-270.
63. Greenwood, T. "An Integral Model for the Turbulent, Supersonic Near Wake Employing Strong Interaction Concepts," Ph.D Thesis, University of Texas, Austin, Texas, 1971.
64. Weinstein, A. S. "Diffusion of Momentum from Free and Confined Slot Jets into Moving Secondary Streams," Ph. D Thesis, Carnegie Institute of Technology, 1955.
65. Gauthier, M. F. "PETULA (Programme d'Ecoulements Turbulents ou Laminaires) Un Exemple de Modèle Mathématique Complexe en Mécanique des Fluides," AGARD Lecture Series AGARD-LS-48, AD-744603, May 1972. P. 313.
66. Chapman, A. J. and Korst, H. H. "Free Jet Boundary with Consideration of Initial Boundary Layer," Proceedings of the Second U. S. National Congress of Applied Mechanics, University of Michigan, Ann Arbor, Michigan, June 14-18, 1954.
67. Ferri, A. (Ed.) "Improved Nozzle Testing Techniques in Transonic Flow," AGARDograph No. 208, from papers and discussions at the 35th AGARD Fluid Dynamics Panel Meeting, Rome, Italy, September 4-10, 1974.
68. Batiuk, G. "A Bibliography of Plume Effects Investigations Conducted by the Army Missile Command," Technical Report RD-76-16, December 1975.
69. Spratley, A. V. "An Investigation of Boattail Geometry and Reynolds Number Effects on Forebody and Afterbody Drag at Transonic Mach Numbers," AEDC-TR-76-161, February 1977.
70. Mueller, T. J. "Determination of the Turbulent Base Pressure in Supersonic Axisymmetric Flow," AIAA Paper No. 67-446, Presented at the AIAA 3rd Propulsion Joint Specialist Conference, Washington, D. C., July 17-21, 1967.

71. Wu, J. M., Moulden, T. H., Elfstrom, G. M., Reddy, K. C., Chen, C. W., Nygaard, R., Shen, L., Venhaus, H. H., and Anjaneyulu, K. "Fundamental Studies of Subsonic and Transonic Flow Separation - Summary Report," AEDC-TR-75-95, Part I, September 1975, Parts II and III, to be published.
72. Chen, C. H. "Study of Subsonic and Transonic Flow Separation - with and without Upstream Disturbance," Ph.D Thesis, University of Tennessee, Knoxville, Tennessee, March 1975.
73. Reubush, D. E. and Runckel, J. F. "Effect of Fineness Ratio on the Boattail Drag of Circular-Arc After-bodies Having Closure Ratios of 0.50 with Jet Exhaust at Mach Numbers up to 1.30," NASA TN D-7192, May 1973.
74. Reubush, D. E. "Effects of Fineness and Closure Ratios on Boattail Drag of Circular-Arc Afterbody Models with Jet Exhaust at Mach Numbers up to 1.3," NASA TN D-7163, May 1973.
75. Reubush, D. E. "An Experimental Investigation of Jet Plume Simulation with Solid Circular Cylinders," NASA TM X-71963, 1974.
76. Shrewsbury, G. D. "Effect of Boattail Juncture Shape on Pressure Drag Coefficients of Isolated After-bodies," NASA TM X-1517, 1968.
77. Kuhn, G. D. "Computer Program for Calculation of Separated Turbulent Flows on Axisymmetric After-bodies," AEDC-TR-77-72, June 1977.
78. Whitfield, D. L. and Yaros, S. F. Private communication. Arnold Engineering Development Center, Arnold Air Force Center, Tennessee, March 1977.

## APPENDIX A

DEVELOPMENT OF AN APPROXIMATE CLOSED FORM SOLUTION  
FOR THE TRANSIENT INITIAL BOUNDARY LAYER INTEGRALS

A method of approximating the integrals encountered in the expression for  $\phi$ , Equation (8), page 60, was suggested to the author by Whitfield (78) and is based on the series expansion work of Chapman and Korst (66). Implementation of this series approximation has decreased the CPU time involved in the evaluation of these integrals using Gaussian quadrature by a factor of five with negligible loss in accuracy, even at extremely high values of  $\eta_p$ , on the order of  $10^4$ .

Basically, the method involves the realization that evaluation of the integral

$$I_{2a} = \frac{1}{\sqrt{\pi}} \int_{\eta-\eta_p}^{\eta} \left( \frac{\eta-\beta}{\eta_p} \right)^{1/m} e^{-\beta^2} d\beta \quad (A-1)$$

depends strongly on the extremely peaked nature of the exponential function. As such, the boundary layer profile in the integrand may be expanded in a Taylor series about the maximum value of the integrand, which occurs at

$$\beta_{\max} = \frac{\eta}{2} - \sqrt{\left( \frac{\eta}{2} \right)^2 + \frac{1}{2m}}$$

The positive root of the differentiation has been rejected since it always falls above the upper limits of

integration. For all intergration limit values of  $\eta$  and  $\eta_p$ , expansion about this maximum is valid, with one exception. Only if the lower limit of integration exceeds the value of  $\beta_{max}$  is this not possible, in which case the integrand may be expanded about the lower limit,  $\eta - \eta_p$ .

Given  $I_{2a}$  as defined in Equation (A-1), the velocity profile of the boundary layer may be expanded in a Taylor series for the case  $\eta - \eta_p < \beta_{max}$ , as follows:

$$g(\beta) = \left( \frac{\eta - \beta}{\eta_p} \right)^{1/m} = g(\beta_{max}) + \frac{dg}{d\beta}(\beta_{max}) \frac{\beta - \beta_{max}}{1!} + \dots$$

thus

$$I_{2a} = \frac{g(\beta_{max})}{\sqrt{\pi}} \int_{\eta - \eta_p}^{\eta} \left( 1 - \frac{1}{m} \frac{\beta - \beta_{max}}{\eta - \beta_{max}} \right) e^{-\beta^2} d\beta$$

or

$$I_{2a} = \frac{g(\beta_{max})}{\sqrt{\pi} m(\eta - \beta_{max})} \left\{ \left[ m + (1-m)\beta_{max} \right] \int_{\eta - \eta_p}^{\eta} e^{-\beta^2} d\beta \right. \\ \left. - \int_{\eta - \eta_p}^{\eta} \beta e^{-\beta^2} d\beta \right\}$$

which becomes, after integration,

$$I_{2a} = \frac{\left(\frac{\eta - \beta_{max}}{\eta_p}\right)^{1/m}}{2\sqrt{\pi}m(\eta - \beta_{max})} \left\{ [mn + (1-m)\beta_{max}] \sqrt{\pi} \left[ \operatorname{erf} \eta - \operatorname{erf}(\eta - \eta_p) \right] + e^{-\eta^2} - e^{-(\eta - \eta_p)^2} \right\}$$

If  $\eta - \eta_p \geq \beta_{max}$ , then the corresponding expression is:

$$I_{2a} = \frac{1}{2\sqrt{\pi} mn_p} \left\{ [n + (m-1)\eta_p] \sqrt{\pi} \left[ \operatorname{erf} \eta - \operatorname{erf}(\eta - \eta_p) \right] + e^{-\eta^2} - e^{-(\eta - \eta_p)^2} \right\}$$

Similarly, if the upper initial boundary layer contribution is considered, that is to say, the integral involving  $\phi_{2b}$ , then the approximate closed form solution may be written as

$$I_{2b} = \frac{\left(-\frac{\delta_a}{\delta_b} \frac{\eta - \beta_{max}}{\eta_p}\right)^{1/m}}{2\sqrt{\pi} m(\eta - \beta_{max})} \phi_b \left\{ [mn + (1-m)\beta_{max}] \sqrt{\pi} \left[ \operatorname{erf} \left( \eta + \frac{\delta_b}{\delta_a} \eta_p \right) - \operatorname{erf} \eta \right] + e^{-\left(\eta + \frac{\delta_b}{\delta_a} \eta_p\right)^2} - e^{-\eta^2} \right\}$$

for the case where  $\eta + \frac{\delta_b}{\delta_a} \eta_p > \beta_{max}$ , and

$$I_{2b} = \frac{-\phi_b}{2\sqrt{\pi} m \frac{\delta_b}{\delta_a} \eta_p} \left\{ \left[ \eta - (m-1) \frac{\delta_b}{\delta_a} \eta_p \right] \sqrt{\pi} \left[ \operatorname{erf} \left( \eta + \frac{\delta_b}{\delta_a} \eta_p \right) \right. \right. \\ \left. \left. - \operatorname{erf} \eta \right] + e^{\left( -\eta + \frac{\delta_b}{\delta_a} \eta_p \right)^2} - e^{-\eta^2} \right\}$$

for the case where  $\eta + \frac{\delta_b}{\delta_a} \eta_p \leq \beta_{\max}$ .

## APPENDIX B

## LISTING OF THE PLUME ENTRAINMENT PROGRAM, DELPL

The DELPL Program, as described in Chapter III, and its associated subroutines are inserted directly into the CVI Program when an afterbody with a real plume is analyzed. DELPL obtains its required input parameters, which are listed in Table VI, page 68, from a calling subroutine in the CVI Program through its argument list and returns the values of the displacement thickness corrections due to plume entrainment in a like manner. The numerical integrations are performed by the subroutine GSS96, which is called by DELPL at several locations. GSS96 in turn calls the function F, which evaluates the velocity function,  $\phi$ , and provides the numerical values of the integrands of the integrals  $I_1(n_{Ra})$ ,  $I_2(n_{Ra})$ , and other integrals used in the calculation of the stagnation temperature correction.

The integrals appearing in the basic relationship for  $\phi$ , Equation (8), page 60, are evaluated in function F using the approximations described in Appendix A at a large saving in CPU time.

The DELPL program is relatively fast compared to the CVI Program, with twenty-five complete  $\delta_e^*$  calculations, a typical number, requiring about ten CPU seconds on the IBM 370/165. For a typical viscous/inviscid solution of

twenty complete iterations, the increase in CPU time due to the entrainment calculations is approximately 10%.

```

SUBROUTINE DELPL(X,FB,TUA,TUB,CPA,UA,DSTRA,DSTRB,EN,N,IWR,DSTRE)
IMPLICIT REAL*8(A-H,O-Z)
DIMENSION X(100),DSTRE(100),IWR(3)
DIMENSION ETADUM(100),FDUM(100)
COMMON /PARAM/ETA,BETA,SQPIN,FFB,ETAP,DDA,DUB,TT,CA2,PWR
COMMON/XDUM/XDUM
COMMON/FSUBC/FSUBC,ETAL,ETAM
SQPIN=.5641895B35D0
FSUBC=.87462573D0
C
C *** X RECEIVED IN INCHES, THEN CONVERTED TO FEET FOR CALCULATIONS. DSTRE
C *** RETURNED IN INCHES.
C
C     DD 104 I=1,N
C     IF(X(I).LE.0.0) X(I)=1.0
C     X(I)=X(I)/12.00
104    CONTINUE
C
C *** COMPUTE CROCCO NO. SQUARED
C
C     CA2=UA**2/12.00*CPA*TUA
C
C *** COMPUTE OTHER NEEDED PARAMS.
C
C     DA=(1.00+EN)*DSTRA
C     DB=(1.00+EN)*DSTRB
C     THA=EN/(2.00+EN)*DSTRA
C     THB=EN/(2.00+EN)*DSTRB
C     DDA=DA
C     DDB=DB
C     TT=TDB/TUA
C     PWR=1.00/EN
C     FFB=FB
C     FB2=FB**2
C     RR=(1.00-CA2)/(TT-CA2*FB2)
C
C *** INITIAL OUTPUT
C
C     WRITE(6,110)
110    FORMAT('0',T8,'CA2',T23,'DA',T38,'DB',T53,'THA',T68,'THB',T83,
* 'TT',T98,'PWR',T113,'RR')
C     WRITE(6,105)CA2,DA,DB,THA,THB,TT,PWR,RR
105    FORMAT(1H ,8(1PE15.8),/)
C     IF(IWR(1).EQ.1) WRITE(6,101)
101    FORMAT('1',T57,'COMPUTE D*E',//)
C     IF(IWR(1).EQ.0) WRITE(6,102)
102    FORMAT(' T9,X(I)',T24,'SIGMA',T40,'ETAP',T57,'I1',T73,'I2',T89,
* 'IE1J',T105,'ETAM',T120,'DSTRE')
C     DO 100 I=1,N
C
C *** N IS NUMBER OF X'S
C
C     XDUM=12.00*X(I)
C
C *** COMPUTE SIGMA,ETAP, ETRA, AND ETRB
C
C     SIG =12.00+2.75800*DJSQRT(5.00*CA2/(1.00-CA2))
C     SIG=(1.00+FB)/(1.00-FB)*SIG

```

C

```

SIG0=SIG
SIG=SIG*(X(I)/(DA+DB)/36.921D0)**(1.00/6.966D0)
IF(SIG.GT.SIG0) SIG=SIG0
ETAP = SIG*DA/X(I)
ETRA=ETAP+4.00
ETRB=-DB*ETAP/DA-4.00

C *** ITERATION FOR STAG. TEMP. CORRECTION INTEGRAL LIMITS
C
ETAH=ETRA
DETAH=ETRA/2.01
ETAL=ETRB
DETAL=-ETRB/2.01
231 ETAH=ETAH-DETAH
FETAH=F(ETAH,3)
IF(FETAH.LT.9.999D-1) GO TO 230
GO TO 231
230 IF(DETAH.LT.1.0-5*ETAP) GO TO 232
ETAH=ETAH+DETAH
DETAH=DETAH/10.00
GO TO 231
232 ETAL=ETAL+DETAL
FETAL=F(ETAL,3)
IF(FETAL.GT.1.000100#FB,OR,FETAL.LT.9.999U-1#FB) GO TO 233
GO TO 232
233 IF(DETAL.LT.1.0-5*DB/DA*ETAP) GO TO 234
ETAL=ETAL-DETAL
DETAL=DETAL/10.00
GO TO 232
234 CONTINUE

C *** COMPUTE INTEGRALS FOR STAG. TEMP. CORRECTION
C
CALL GSS96(4,ETAL,ETAH,PHIERF)
CALL GSS96(3,ETAL,ETAH,PHIACT)
IF(I.EQ.1) FSCREF=(PHIERF-PHIACT)/PHIERF
FSBCI=(PHIERF-PHIACT)/PHIERF
FSUBC=FSBCI/FSCREF

C *** COMPUTE I1(ETAH) AND I2(ETAH)
C
SUMI1=0.00
SUMI2=0.00
NLMI
XNLM=NLM
DO 220 NLMI=NLM
XNL=NLM
ETRL=ETRA-(ETRA-ETRB)/XNLM*(XNL-1.00)
ETRH=ETRB-(ETRA-ETRB)/XNLM*XNL
CALL GSS96(1,ETRL,ETRH,S11)
CALL GSS96(2,ETRL,ETRH,S12)
SUMI1=SUMI1+S11
SUMI2=SUMI2+S12
220 CONTINUE
SIP = ETRH*(1.00-CA2)*FB/(TT-CA2*FB2)
S11=SUMI1*SIP
S12=SUMI2*SIP*FB
S11CHK=ETRA-ETAP/DA*(DSTRA+RR*FB*DSTRB)
S12CHK=ETRA-ETAP/DA*(DSTRA+THA+RR*FB2*(USTRB+THB))
210 FORMAT(1H ,8(1PE15.8))
C
C *** COMPUTE I1(ETAJ)
C
S11EJ=(S11-S12-ETAP*(RR*FB2*THB+THA)/DA)/(1.00-FB)
C
C *** COMPUTE ETAM

```

```

C
C      ETAM = ETRA = (SI2*FB*SI1)/(1.00-FB)
C      ETAM = ETAM - ETAP*(THB*RR*FB2 + THA + DSTRA*(1.00-FB))/(
C      * (DA*(1.00-FB)))
C
C *** COMPUTE DSTRE(I)
C
C      DSTRE(I) = DA*(ETAM-SI1EJ*(TT-CA2*FB2)/(FB*(1.00-CA2)))/FTAP-DSTHB
C
C *** DSTRE CONVERTED TO INCHES.  X CONVERTED BACK TO INCHES.
C
C      DSTRE(I)*12.00*DSTRE(I)
C      X(I)=12.00*X(I)
C      IF (LWR(I),EQ,1) WRITE(6,103) X(I),SIG,ETAP,SI1,SI2,SI1EJ,ETAM,
C      *DSTRE(I)
103  FORMAT(8(1PE16.6))
100  CONTINUE
      RETURN
      END
      SUBROUTINE G5596 (A,B,E)
      IMPLICIT REAL*8 (A-H,O-Z)
      COMMON /CARE/ NEAT
      DIMENSION X(48), W(48)
      DATA N/4/
      DATA X/.01627674484960295,.04881298513604970,.0H129749546442540,.1 AG 1
      1136958501106657,.1459737146548967,.1780968823676185,.2100313104605 AG 2
      2671,.2417431561638399,.2731988125910489,.3043649443544962,.3352085 AG 3
      3228926253,.3656968614723135,.3957976498289084,.425478984073005,.4 AG 4
      4547094221677428,.4836579739205962,.5116941771546677,.5393981083243 AG 5
      5572,.5665104185613971,.5930323647775719,.6189258401254685,.6441634 AG 6
      6037849670,.6687183100439160,.6925645366421715,.7156768123489674,.7 AG 7
      7380306437444000,.7596023411766472,.7803690438674331,.8003087441391 AG 8
      8407,.8194003107379315,.8376235112281869,.854590334346013,.8713805 AG 9
      9059092963,.8868945174024203,.9014606353158521,.9150714231208981,.9 AG 10
      B277124567223085,.9393703397527551,.9500327177844374,.9596882914487 AG 11
      8423,.9683268284632640,.9759391745851364,.9825172635630146,.9880541 AG 12
      B263296236,.9925439003237624,.9959818429872091,.9983643758631815,.9 AG 13
      B996895038832307/
      DATA W/.03255061449236316,.03251611871386881,.03244716371406424,.0 AG 14
      132234382256857591,.03220620479403022,.03203445623199264,.0318287588 AG 15
      29441099,.03158933077072714,.03131642559686134,.03101033258531383. AG 16
      3030671376123866912,.03029991542082757,.02989634413632838,.029461089 AG 17
      495816790,.02899461415055522,.02849741106508536,.02797000761684831, AG 18
      5.02741296272602922,.02682686672559174,.02621234073567240,.02557003 AG 19
      6600534935,.02490063322248359,.02420484179236466,.02348339908592620 AG 20
      71,.0227370696832935,.02196664443874432,.02117293989219129,.0203567 AG 21
      B9715433329,.01951908114014500,.01866067962741145,.0177825023160452 AG 22
      93,.01688547986424515,.01597056290256227,.01503872102699493,.014090 AG 23
      894177231485,.01312822956696156,.01215160467108829,.011162102099838 AG 24
      848,.01016077053500841,.009148671230783383,.008126876925698756,.007 AG 25
      8096470791153859,.006058545504235957,.005014202742927514,.003984554 AG 26
      8338444683,.002910731817934944,.001853960788946920,.000796792065552 AG 27
      %0122/
      E=0.000 AG 35
      HR=0.5*(B-A) AG 36
      FMID=0.5*(A+B) AG 37
      DO 1 J=1,N AG 38
      XT=FMID+HR*X(J) AG 39
      XS=FMID+HR*X(J) AG 40
      E=E+W(J)*IF(XS,K)*F(XT,K) AG 41
      1 CONTINUE AG 42
      E=HR*E AG 43
      RETURN AG 44
      END AG 45
      FUNCTION F (X,I)
      IMPLICIT REAL*8 (A-H,O-Z)

```

```

COMMON /PARAM/ ETA,BETA,SQPIN,FB,ETAP,DA,DB,TT,CA2,PWR
COMMON /XDUHM/XDUM
COMMON /FSBBC/FSUBC,ETAL,ETAM
ETAXX

C
C *** GIVEN ETA, FIND PHI
C
C
PH1=0.500*(1.00+FB)
PH2=0.500*DERF(ETA-ETAP)
PH3=-0.500*FB*DEHF(ETA+DB-ETAP/DA)

C *** CALCULATION OF INTEGRALS IN VELOCITY FUNCTION BY SERIES EXPANSION
C
TERM4=ETA-ETAP
TERM5=ETA+DB/DA-ETAP
DL4=0.00
UL4=1.00
DLS=-DB/DA
UL5=0.00
IF(ETA.GT.-4.00.AND.ETA.LT.ETAP+4.00) GO TO 3
PH4=0.00
GO TO 4
3
CONTINUE
ARG1=ETA**2
ARG2=(ETA-ETAP)**2
IF(ARG1.GT.115.00) ARG1=115.00
IF(ARG2.GT.115.00) ARG2=115.00
BETAM4=ETA/2.00+DSQRT((ETA/2.00)**2+PWR/2.00)
TC4=DERF(ETA)-DEHF(TERM4)
TD4=DEXP(-ARG1)-DEXP(-ARG2)
IF(TERM4.GE.BETAM4) GO TO 20
TA4=((ETA-BETAM4)/ETAP)**PWR/2.00*SQPIN=PWR/(ETA-BETAM4)
TB4=(ETA/PWR+(1.00-1.00/PWR)*BETAM4)/SQPIN
GO TO 21
20
CONTINUE
TA4=1.00/2.00*SQPIN=PWR/ETAP
TB4=(ETA+(1.00/PWR-1.00)*ETAP)/SQPIN
21
CONTINUE
PH4=TA4*(TB4+TC4+TD4)
4
CONTINUE
IF(ETA.LT.-4.00.AND.ETA.GT.-DB/DA-ETAP-4.00) GO TO 5
PH5=0.00
GO TO 6
5
CONTINUE
ARG1=(ETA+DB/DA-ETAP)**2
ARG2=ETA**2
IF(ARG1.GT.115.00) ARG1=115.00
IF(ARG2.GT.115.00) ARG2=115.00
BETAM5=ETA/2.00+DSQRT((ETA/2.00)**2+PWR/2.00)
TC5=DEHF(TERM5)-DERF(ETA)
TD5=DEXP(-ARG1)-DEXP(-ARG2)
IF(TERM5.LE.BETAM5) GO TO 30
TAS=(-DB/DA*(ETA-BETAM5)/ETAP)**PWR/2.00*SQPIN=PWR/(ETA-BETAM5)*FB
TB5=(ETA/PWR+(1.00-1.00/PWR)*BETAM5)/SQPIN
GO TO 31
30
CONTINUE
TAS=-FB/2.00*SQPIN=PWR/ETAP/DB*DA
TB5=(ETA+(1.00/PWR-1.00)*DB/DA-ETAP)/SQPIN
31
CONTINUE
PH5=TAS*(TB5+TC5+TD5)
6
CONTINUE
PHI=PH1+PH2+PH3+PH4+PH5

C
C *** ADJUSTMENT TO STAG. TEMP. PARAMETER. LAMDA
C
BIGLAM=TT*(1.00-PHI)/(1.00+FB)*(PHI-FB)/(1.00-FB)

```

```

IF (ETA.GE.ETAPI) GO TO 900
IF (ETA.LE.-DH/DA*ETAP) GO TO 900
C=7.39D-2
C=C*FSUBC
BIGLAM = RIGLAM+C
IF (ETA.GE.0.0D) BIGLAM = BIGLAM+C*ETA/ETAP
IF (ETA.LE.0.0D) BIGLAM=BIGLAM-C*ETA/ETAP*DA/DH
900 CONTINUE
FUNC=(1.0D-CA2)/(BIGLAM-CA2*PHI**2)*PHI
IF (ETA.LT.0.0D) GO TO 10
PHIBL=1.0D
IF (ETA.LT.ETAP) PHIBL=(ETA/ETAP)**PWR
GO TO 11
10 PHIBL=FB
IF (ETA.GT.-DH/DA*ETAP) PHIBL=FB*(-DA/DH*ETA/ETAP)**PWR
11 CONTINUE
GO TO (1,2,40,*1),1
C
C *** F FOR 11(ETARAI)
C
1 CONTINUE
F=FUNC
100 FORMAT(1M ,I4,10(1PE12.5))
      RETURN
C
C *** F FOR 12(ETARAI)
C
2 CONTINUE
F=FUNC*PHI
RETURN
C
C *** F IS VELOCITY RATIO FUNCTION FOR ACTUAL FLOW
C
40 CONTINUE
F=PHI
RETURN
C
C *** F IS VELOCITY RATIO FUNCTION FOR FULLY DEVELOPED FLOW
C
41 CONTINUE
IF (ETA.GE.0.0D) ETATMP=1.83D0*ETA/ETAH
IF (ETA.LT.0.0D) ETATMP=1.83D0*ETA/ETAL
F=0.5D0*(1.0D+FB+DERF(ETATMP)-FB*DERF(ETATMP))
RETURN
END

```

C

## APPENDIX C

## ANALYSIS OF THE CBA BOATTAIL - AN ANOMALOUS CASE

An analysis, using the CVI Program, of a boattail similarly analyzed by Chow, Bober, and Anderson (9), resulted in behavior of the viscous/inviscid iteration that was at variance with previous experience. The boattail, shown in Figure C-1, consisted of a circular arc section fairing smoothly into a conical surface of 15 degrees which then joined the cylindrical sting at this angle. Shown for comparison in this figure is the NASA Langley  $l/d_m = 1.768$  Circular Arc Boattail, and it is obvious that the body slopes of the Chow, Bober, Anderson (CBA) boattail are, for a greater distance, steeper than the NASA body, although the closure ratio ( $d_{ex}/d_m$ ) is less.

The CBA boattail was analyzed at four Mach numbers: 0.56, 0.7, 0.8, and 0.9. The data used for comparison were taken from the experimental work of Shrewsbury (76). As can be seen in Figures C-2 and C-3, the CVI Program predictions agree well with the data, excepting the prediction of a higher pressure near the boattail/sting juncture, which has been encountered previously and may be due to a small separated region of an inaccurate value of  $\delta^*$ . At Mach number 0.8, however, there appears to be an instability in the viscous/inviscid iteration, in that two solutions are produced. This situation is best shown in

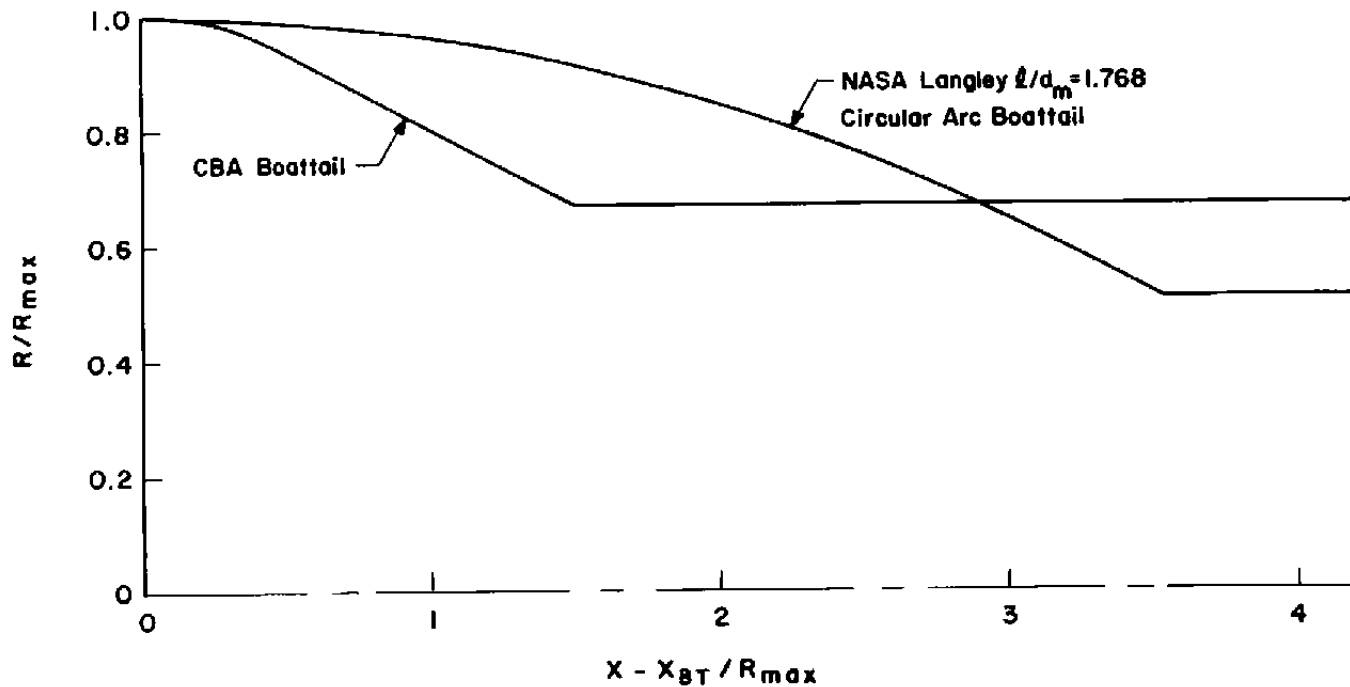


Figure C-1. Comparison of boattail and plume simulator shapes between the NASA Langley 1.768 circular arc boattail and the CBA boattail.

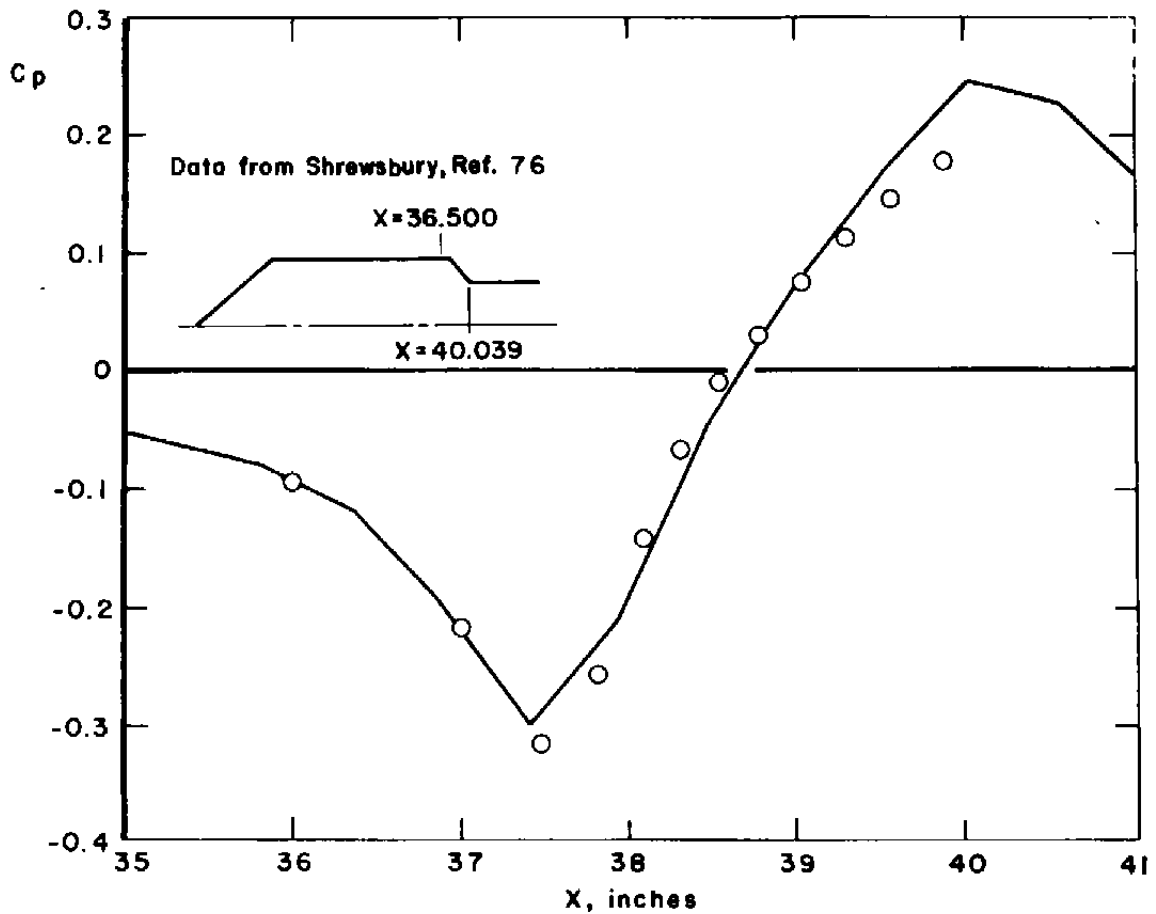


Figure C-2. Longitudinal pressure coefficient distribution for the CBA boattail,  $M_\infty = 0.56$ .

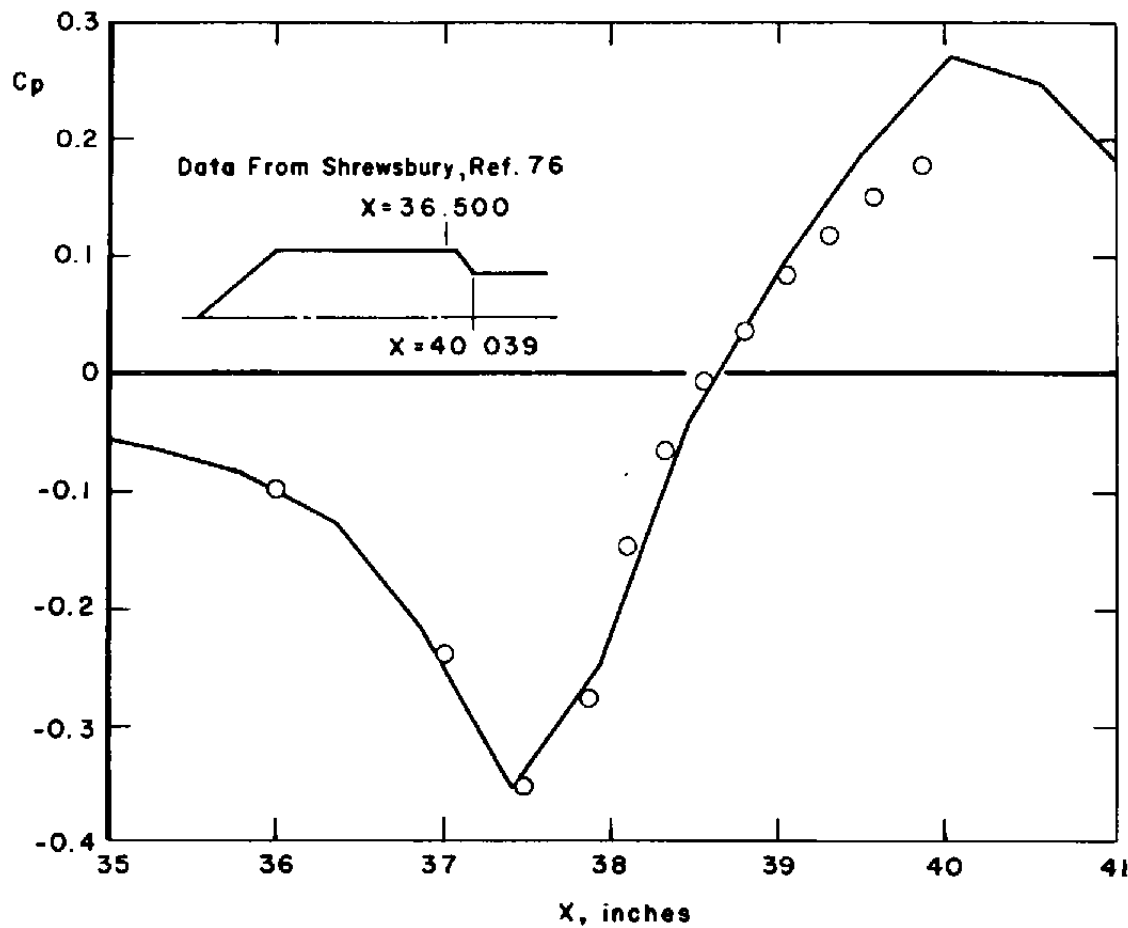


Figure C-3. Longitudinal pressure coefficient distribution for the CBA boattail,  $M_{\infty} = 0.70$ .

Figure C-4, in which the repetitive appearance of two dissimilar solutions appears as a large difference in  $\Delta C_{p_{max}}$  from one iteration to the next, followed by a recovery iteration and an apparently converging solution. Relaxing the boundary layer even more than a factor of 0.3 resulted in a longer period between the two solutions, but little else was changed.

The two solutions are shown in Figure C-5. It is apparent that the subsonic solution, the more stable of the two, is the correct solution, while the supercritical solution, which appears once at intervals depending on boundary layer relaxation, is in error, particularly in the expansion about the shoulder of the boattail.

At a Mach number of 0.9, the solution to the CVI Program prediction is shown in Figure C-6. This solution converged quickly, but it is grossly in error. It does, however, protract the characteristic of the erroneous, or "anomalous" solution of the 0.8 Mach number case, i.e. the movement of the point of minimum  $C_p$  downstream one grid point.

At the time of this writing, the reasons for such anomalous behavior are still in question. One numerical experiment, however, in which the inviscid portion of the CVI Program was restricted to central differencing is worthy of note. In the 0.8 Mach number case, rotated differencing in the South-Jameson Transonic Program was bypassed after iteration six. The solution proceeded to converge smoothly and

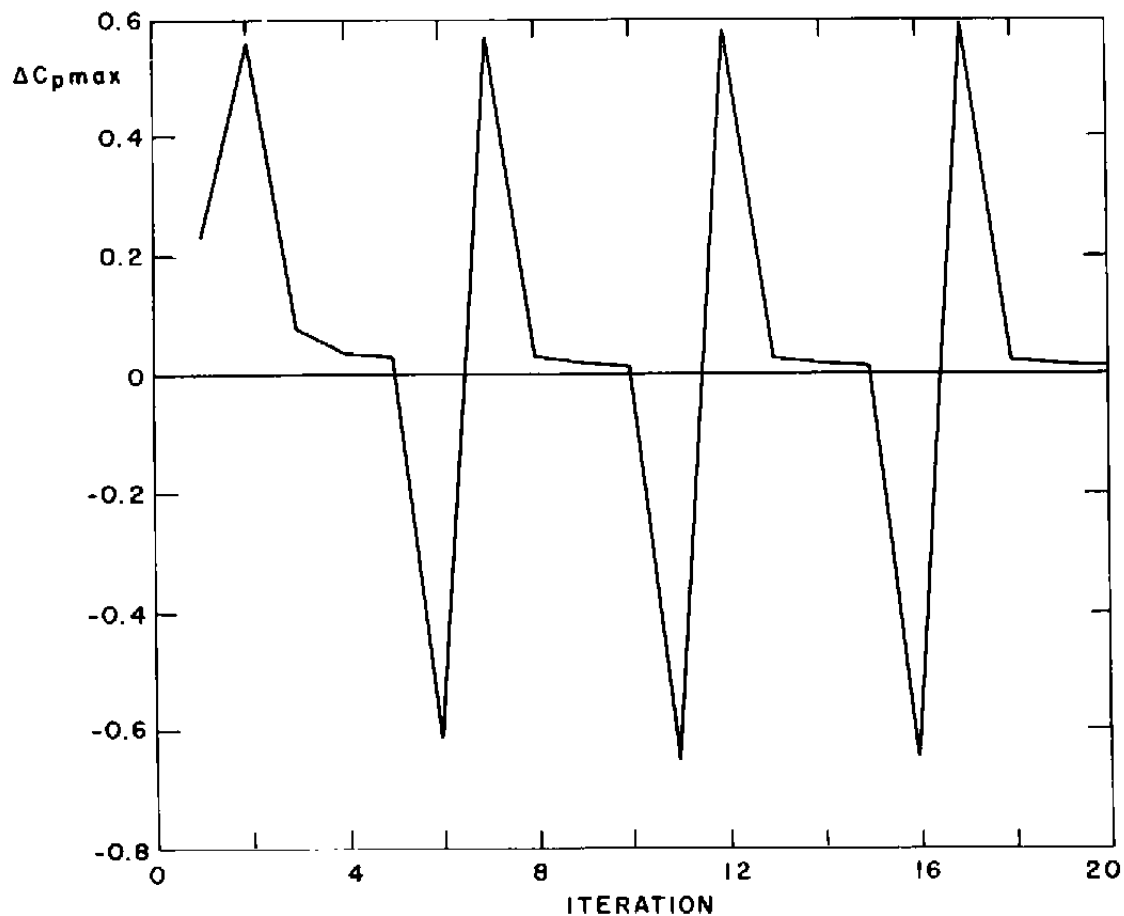


Figure C-4. Maximum pressure coefficient change at each iteration showing presence of two solutions,  $M_\infty = 0.80$ .

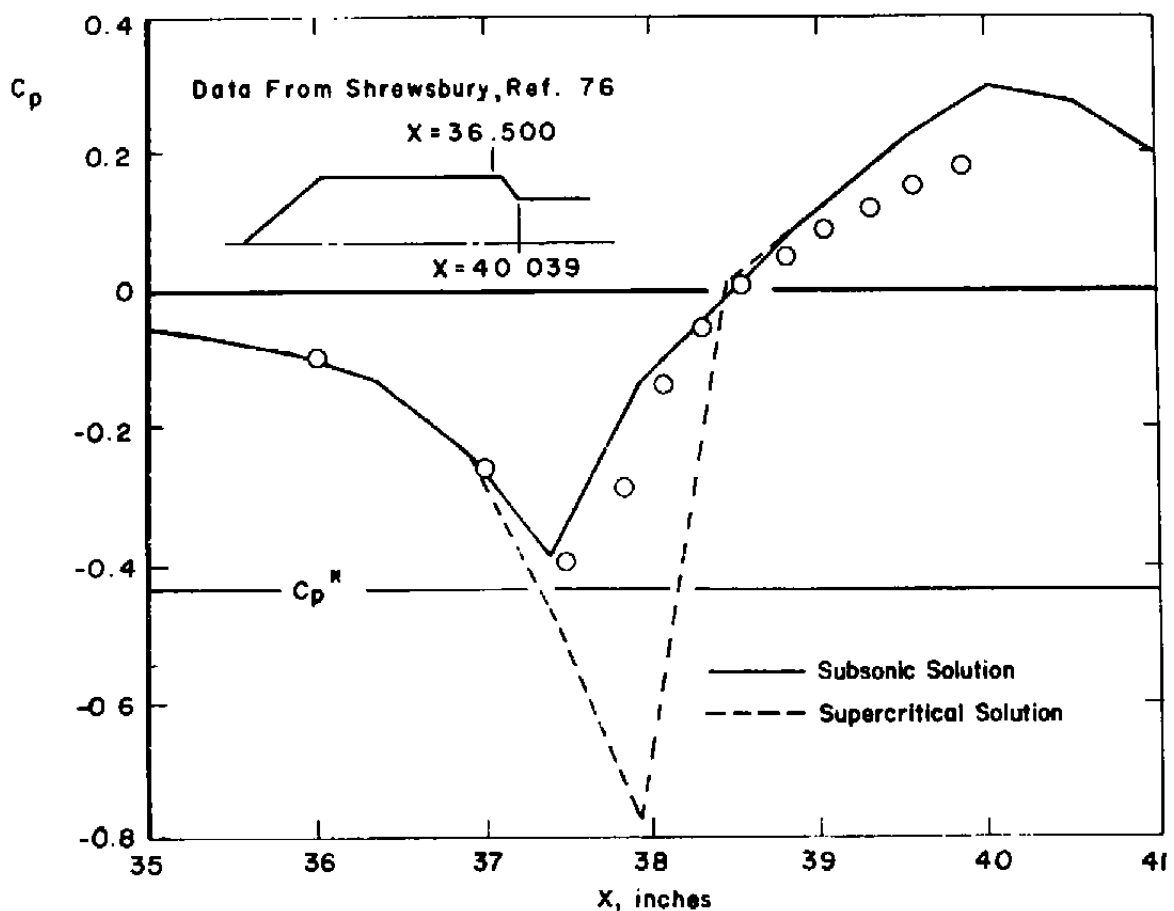


Figure C-5. Longitudinal pressure coefficient distribution for the CBA boattail showing presence of two solutions,  $M_{\infty} = 0.80$ .

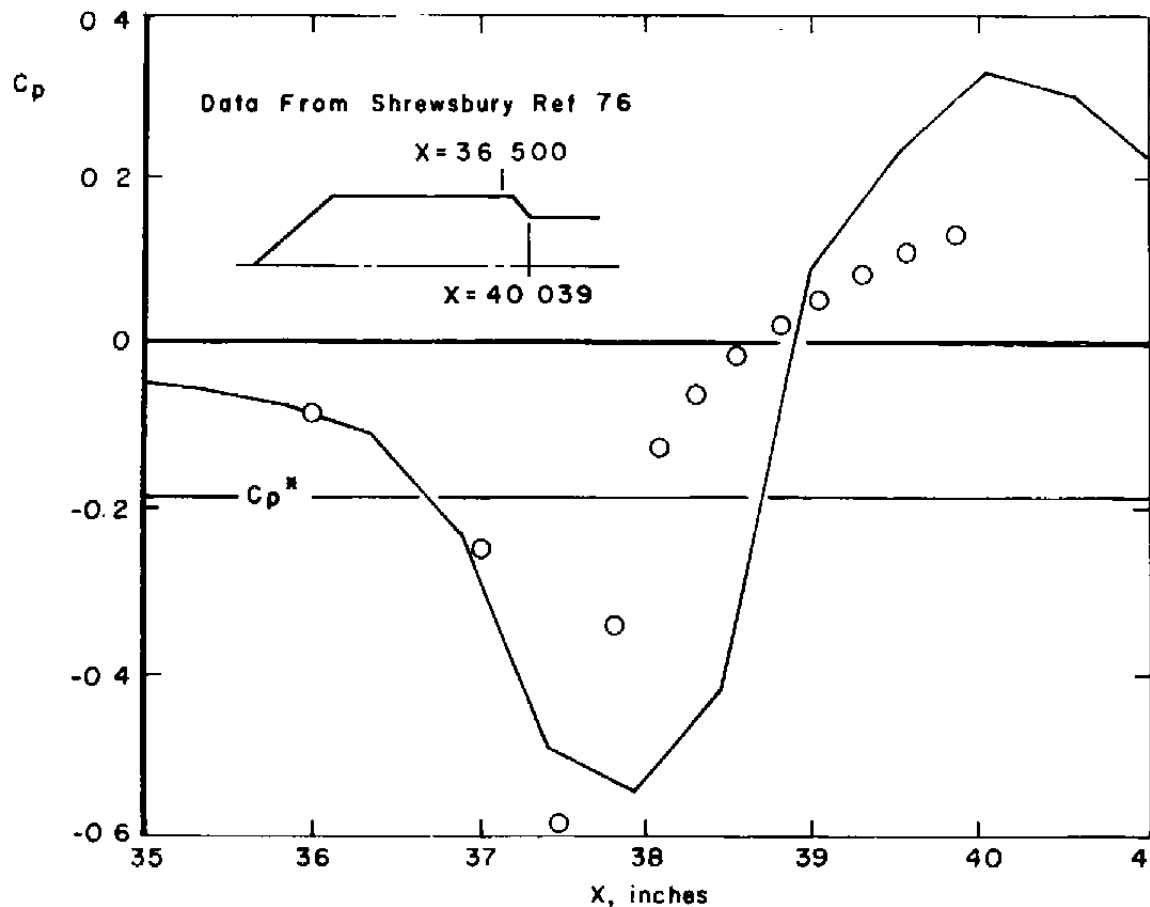


Figure C-6. Longitudinal pressure coefficient distribution for the CBA boattail showing erroneous solution,  $M_\infty = 0.90$ .

definitely, and the resulting  $C_p$  distribution is shown in Figure C-7. It agrees well with the data. Similar experimentation with the 0.9 Mach number case failed, as the central differencing was not capable of converging under supersonic conditions about the shoulder of the boattail.

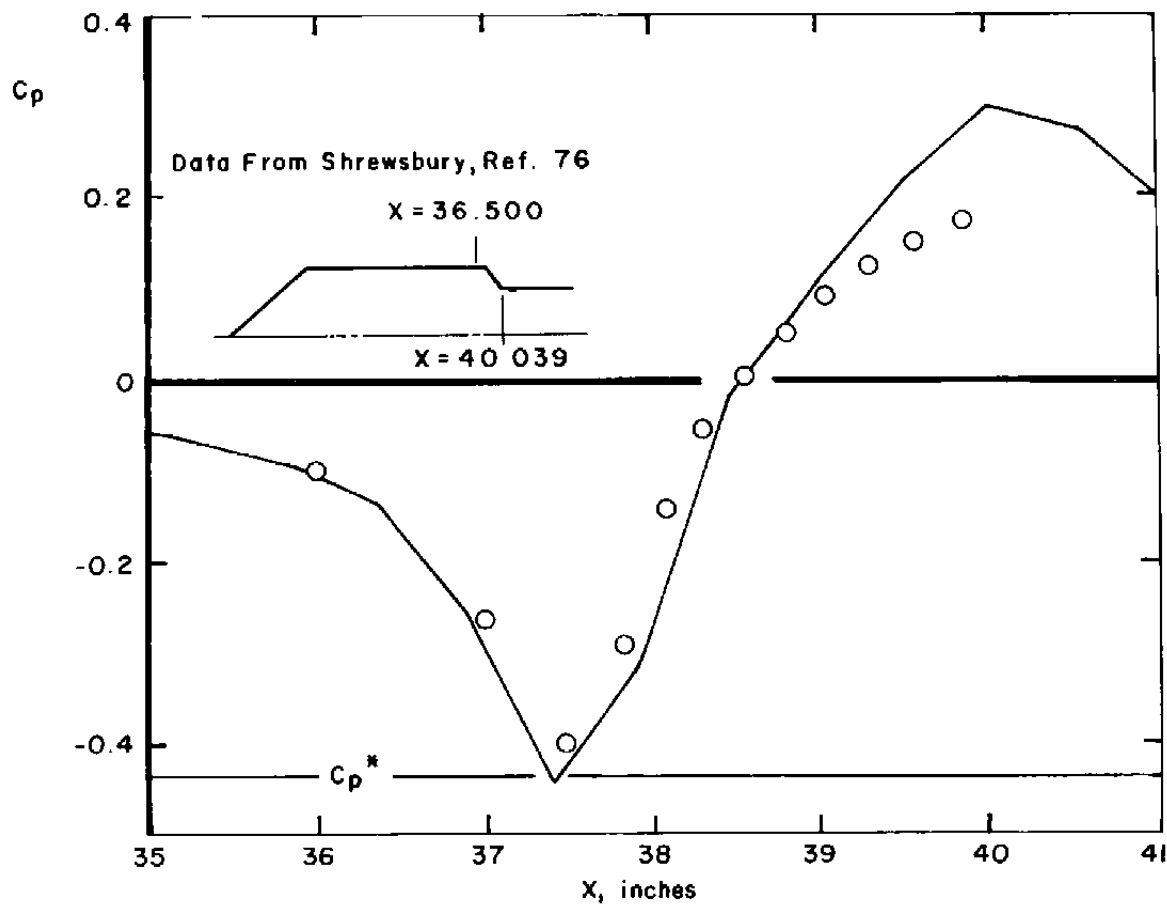


Figure C-7. Longitudinal pressure coefficient distribution for the CBA boattail using central differences only,  $M_\infty = 0.80$ .

## NOMENCLATURE

Symbols with generally recognized definitions are listed as such. Other symbols are referred to the applicable portion of the text. Additional terms, used primarily as input parameters to particular programs, may be found in the applicable table.

a	Local speed of sound
$C_a$	Crocco number of internal flow at initial conditions, $C_a = \frac{u_a}{\sqrt{2 c_p T_0}}$
$C_f$	Friction coefficient, Bartz, p. 30
$C_h$	Stanton number, Bartz, p. 31
$C_p$	Pressure coefficient
$c_{p_a}$	Specific heat at constant pressure for internal flow
d	Diameter
H	$H = 1 + Kn$ , RAXBOD, p. 19
K	Curvature of reference coordinate system, RAXBOD, p. 19
l	Length
M	Local Mach number
p	Pressure
Pr	Prandtl number
q	Total velocity, $\sqrt{u^2 + v^2}$ , RAXBOD, p. 21
r	Radius of body, Bartz, p. 30

R	Radius
R	Boundary layer relaxation factor, p. 44
Re	Reynolds number
Re/ $\lambda$	Unit Reynolds number, $ft^{-1}$
$R_\theta$	Reynolds number based on momentum thickness, Bartz, p. 31
$R_\phi$	Reynolds number based on energy thickness, Bartz, p. 31
T	Temperature
u, v	Streamwise and transverse velocity components, Chapman-Korst mixing theory, p. 58
U, V	Streamwise and transverse velocity components
U, V	Velocity components in $\xi, \eta$ system, RAXBOD, p. 19
x, y	Intrinsic coordinate system, Chapman-Korst mixing theory, p. 58
X, Y	Streamwise and transverse coordinates in the physical coordinate system
z	Axial coordinate, Bartz, p. 30
$\delta$	Boundary layer thickness
$\delta^*$	Boundary layer displacement thickness
$\epsilon$	Eddy viscosity, Chapman-Korst mixing theory, p. 58
$\eta$	Nondimensional similarity variable, Chapman-Korst mixing theory, p. 60
$\eta_p$	Position parameter, Chapman-Korst mixing theory, p. 60
$\theta$	Inclination of reference coordinate system, RAXBOD, p. 19

$\theta$	Momentum thickness, Bartz, p. 30
$\Lambda$	Stagnation temperature ratio, Chapman-Korst mixing theory, p. 63
$\xi, \eta$	Orthogonal curvilinear coordinates, RAXBOD, p. 19, or sheared cylindrical coordinates, RAXBOD, p. 20
$\rho$	Density
$\sigma$	Mixing coefficient, Chapman-Korst mixing theory, p. 58
$\phi$	Disturbance potential, RAXBOD, p. 19
$\phi$	Energy thickness, Bartz, p. 30
$\phi$	Velocity function, $u/u_a$ , Chapman-Korst mixing theory, p. 58
$\psi$	Nondimensional x-coordinate, $x/\delta_a$ , Chapman-Korst mixing theory, p. 58

## SUBSCRIPTS

$a, b$	Initial internal and external quantities, Chapman-Korst mixing theory, Figure 13, p. 56
$aw$	Adiabatic wall
$bod$	Body
$BT$	Quantity measured from beginning of boattail
$e$	Pertaining to effective plume
$ex$	Pertaining to exhaust
$j$	Pertaining to dividing streamline location, Chapman-Korst mixing theory, Figure 13, p. 56
$m$	Pertaining to intrinsic coordinate obtained in Chapman-Korst mixing theory, Figure 13, p. 56
$m, max$	Maximum

NN	Second derivative normal to velocity vector, RAXBOD, p. 21
NOZ	Pertaining to nozzle
o	Stagnation condition
p	Value at particular x-locations used by RAXBOD, p. 43
$R_a, R_b$	Reference limits of internal and external flows
rel	Pertaining to relaxed boundary layer displacement thickness
SS	Second derivative along velocity vector, RAXBOD, p. 21
w	Wall condition
$\infty$	Free-stream conditions
2a,2b	Initial boundary layer velocity profile shapes
I,II	One-stream and two-stream values of $\sigma$ , respectively, Chapman-Korst mixing theory, p. 79

## SUPERSCRIPTS

'	First derivative in longitudinal direction
"	Second derivative in longitudinal direction
$n, n-1$	Pertains to number of iteration in the South- Jameson (RAXBOD) or CVI Programs
*	Indicates critical (sonic) value

Auxiliary Integrals

$$I_1(n) = \frac{n_{Rb} (1-c_a^2) \phi_b}{\frac{T_{ob}}{T_{oa}} - c_a^2 \phi_b^2} + \int_{n_{Rb}}^n \frac{(1-c_a^2) \phi}{\Lambda - c_a^2 \phi^2} dn$$

$$I_2(\eta) = \frac{\eta_{Rb} (1-c_a^2) \phi_b^2}{\frac{T_{Ob}}{T_{Oa}} - c_a^2 \phi^2} + \int_{\eta_{Rb}}^{\eta} \frac{(1-c_a^2) \phi^2}{\Lambda - c_a^2 \phi^2} d\eta$$